COSMIC RAY STUDIES WITH A STREAMER CHAMBER

by

Ibrahim A. Hassairi

B.Sc. Libya M.Sc. London

A thesis submitted for the degree of Doctor of Philosophy in the University of London

Bedford College

London

1976

ABSTRACT

A streamer chamber system has been developed to study the multiple scattering of cosmic rays at sea level. The thesis described new electronic circuits for the control of the system, and a new method for applying high voltage pulses of short duration.

Multiple scattering studies have been conducted with one inch slabs of lead and mercury. When 138 MeV muons were identified by their decay electron, excellent agreement was obtained with the Cooper and Rainwater theory. Without this identification anomalous results were obtained.

During the course of the research, an interesting new effect has been observed - the appearance of rings on the Lichtenberg figures associated with the discharge in the chamber.

CONTENTS

CHAPTER 1

Aspects of Gas Discharges

1.1 Introduction

A great deal of theoretical and experimental work has been done on gaseous discharges, and spark formation over the past 70 years. A quantitative theory of the initial avalanche phase at low pressures was developed by Townsend (1914) and the transition of an avalanche into a streamer was observed experimentally in a cloud chamber by (Raether (1937)). The semi-empirical conditions under which this occurs were worked out by Meek, and by Raether shortly thereafter. In 1969 Lozanskii devised a theory of streamers based on the concept of the streamer as an expanding conducting plasma.

1.2 Single Avalanche

Three basic methods have been used to study the avalanche process in a gas.

(1) The cloud chamber method. This technique is useful in studying the distribution of the ions after a pulse of a given amplitude and duration has been applied.

(2) The electrical method. The drifting electrons and ions of the avalanche produce an electrical current during their transit time; this pulse displayed on an oscilloscope provides a record of the avalanche current as a function of time.

(3) The optical method. The drifting electrons of the avalanche excite the

gas molecules and cause them to emit light. A photomultiplier can be used to convert the light into an electrical pulse which can be seen on an oscilloscope, as in the electrical method. Photography, in general, is not sufficiently sensitive to investigate the growth of single avalanches.

Townsend studied the variation of the current in a gap between plane parallel electrodes, as a function of an applied electric field. To consider what happens when an electric field is applied to a free electron in a gas; for a sufficiently high field, the energy lost by elastic collision is proportional to 2 m/M, where m and M are the masses of the electron and atom, respectively. This is negligible and the electron continues to gain energy until it causes ionization. This assumes a small energy loss due to the excitation of atomic levels. The total number of drifting electrons grows as:

$$n\ (x) = \exp (\alpha\ x) \qquad 1.2.1$$

The first Townsend coefficient α is the mean number of ionizing collisions made by one electron in travelling one centimetre. Thus the mean free path for ionization is $1/\alpha$. x is the length attained by the avalanche and is given as a function of time (t) by:

$$x = vt = bEt \qquad 1.2.2$$

where v is the drift velocity of the electron,

b is the electron mobility and

E is the electric field.

Typically in the electric fields encountered in this type of work the drift velocity for electrons is about 10^7 cm/sec and for ions is about 10^5 cm/sec; therefore ions are virtually stationary during say, an interval of about 20 nsec. which is of interest to us. Because of the diffusion of the electrons perpendicular to the field the radius of the avalanche also increases as a function of time. About 85% of the electrons in an avalanche are contained in within a spherical cloud of radius.

$$r^2 = 4Dt \propto E^{1/2}t \qquad 1.2.3$$

Where D is the diffusion coefficient.

The approximate relation $D \propto E^{\frac{1}{2}}$, is verified experimentally (Raether 1964). At zero field, D is finite and is proportional to the thermal energy. It is generally assumed that the number of photons $\frac{dp(t)}{}$ created between t and t+dt is proportional to the number of drifting electrons, i.e.

$$d\,p(t) = \delta \quad n\,(t) \quad v\,dt \qquad 1.2.4$$

where δ is the number of photons produced by one electron per cm. The number of drifting electrons can be found as a function of time by substituting x from equation 1.2.2 into Townsend equation (1.2.1)

$$n\,(t) = \exp\,(\alpha\, v\, t) \qquad 1.2.5$$

Therefore the number of electrons produced in dt is:

$$dn(t) = \alpha \; n(t) \; v \; dt \qquad 1.2.6$$

Thus the number of photons and the number of electrons produced are proportional to the number of drifting electrons. This can be expressed:

$$d_p(t) = Q \, dn(t) \qquad 1.2.7$$

where

$$Q = \delta/\alpha \qquad 1.2.8$$

Experimentally Q is roughly proportional to I/E

α is proportional to E

and δ is to some approximation independent of E, (Bulos et al, 1967)

The order of magnitude of Q is unity at a pressure of one atmosphere.

At E/P $\approx$ 15 to 20 KV/cm torr; an avalanche containing 10^8 electrons will emit 10^8 photons (Bulos et al. 1967).

In this analysis no account is taken of the emission of secondary electrons from an electrode, because this is not of interest for the present studies.

1.3 Streamer Formation

The space charge developed by the avalanche itself transforms the avalanche into a streamer. The mechanism was revealed by observation in the cloud chamber (Raether 1964).

Experiments with the electrical and optical methods have confirmed the principal concept of the mechanism. A striking feature of this transformation is the rapid extension of the streamer. This occurs at a rate of at least 10^8 cm/sec. This is an order of magnitude faster than the drift velocity of the electrons and the rate of extension of the primary avalanche, and it indicates that a different mechanism or mechanisms is involved. The following discussion is intended to refer to noble gases, for example neon, argon or helium.

When the applied field is only slightly higher than is required for streamer formation the growth is toward the anode from the region of highest electron density in the avalanche. This might be due to the increased electron velocity in the perturbed field or to photo ionization. A higher field leads to growth in the cathode direction as well, which can be explained only by photo-ionization. A case of interest to us is when the applied field is 5 to 10 times the field required for static breakdown. After the primary avalanche is formed the dominant process is ionization by photons produced in the original avalanche. These are emitted isotropically and produce other electrons and photons in the gas by photo-ionization. These electrons produce localized secondary avalanches near the positive and negative tips of the original avalanche where the field is intensified by the additional space charge. The new avalanches feed the tips of the original avalanche symmetrically leaving behind space charge which extends the streamer in both directions. (The condition for the self sustaining extension of the streamer is that the electrons feeding the positive tip of the primary avalanche and neutralizing it, leave behind positive ions equal in density to those that existed in the primary avalanche.

Although the streamers can be symmetrical, they originate in the head of the original avalanche, their centers being displaced from the origin of the primary avalanche by a distance $v\,t_m$ where t_m is the time required to reach the streamer phase.

The critical point in the development of a streamer occurs when the density of the electrons is so high that the resulting space charge field in the avalanche is about the same as the applied field. Then recombinations of electrons and positive ions occur within the avalanche, emitting photons which will cause the photo-ionization. The number of electrons in dx is $dn(x)\,[= \alpha \exp(\alpha x)\,dx]$ and these are contained within a volume $\pi r^2 dx$. The electron density is then given by

$$\rho(x) = \frac{\alpha \exp(\alpha x)}{\pi r^2} \qquad 1.3.1$$

where r is the radius of the avalanche head which is assumed to be spherical.

The space field strength at a distance r is given by:

$$E = \frac{e\alpha \exp(\alpha x)}{3\pi \epsilon_0 r} \qquad 1.3.2$$

in M.K.S. units, where e is the electron charge and ϵ_0 is the permittivity constant. It has been shown (Meek & Craggs 1953) that the transition from an avalanche to a streamer occurs when the space charge field is of the order of the applied field; which happens when about 10^8 electrons develop in the avalanche head.
In this case we can write

$$\exp(\alpha x_m) \sim 10^8$$

$$\alpha x_m \sim 20$$

$$x_m \sim 20/\alpha$$

Since α is roughly proportional to the applied field E so that the critical avalanche length or "Meek Length" (and thus the displacement of the streamer centers) goes inversely as the applied field

Hence

$$x_m \propto 20/E$$

In addition (from 1.2.2) $x_m \propto Et_m$

Therefore $E^2 t_m$ = constant

In his studies with a spark gap,

Dickey (1952) indicated that the number of electrons that had to be formed to produce his observed current and thus a significant change in electrode potential should be of the order of 10^{13}. Thus the transition of an avalanche into a streamer takes place when the number of electrons in the avalanche reaches 10^8, but the breakdown of voltage occurs when it is 10^{13}.

A calculation of streamer development was proposed by Lozanskii and Firsov (1969) based on the model of the streamer as an expanding conducting plasma.

Two growth mechanisms are postulated: the expansion towards the anode is due to the existence of a very high field with the leading electrons ionizing the gas: and in the cathode direction photo-ionization liberates electrons in a high field and these multiply and develop into plasma. Their main conclusions are that the streamer propagation velocity is approximately proportional to its length and the streamer thickness is proportional to the square root of the length. Assuming that the equipotential plasma takes the form of an ellipsoid of revolution that is elongated along the field E_o, then E_a the field intensity at the ends of this region is given by, Lozanskii and Firsov to be

$$E_a = E_o \, a \left(R \ln \left(\frac{2}{e} \sqrt{a/R} \right) \right)^{-1} \qquad 1.3.3$$

where a is half the streamer length and R is the radius of curvature of its ends (Fig. 1.3.1).

If the streamer were to have the form of two spheres with radius R connected by a thin filament of length 2a ($a \gg R$) then

$$E_a = Eo \quad a/R \qquad 1.3.4$$

If the streamer is elliptical then the field intensity on its surface and the velocity of the points of this surface, are proportional to the cosine of the angle between the normal to the surface and the direction of the field Eo.

For $a \gg R$, the rate of growth of the streamer is:

$$\left|\dot{a}\right| = K E_o a\left(R \ln \left(\frac{2}{e}\sqrt{\frac{a}{R}}\right)\right)^{-1} \qquad 1.3.5$$

where K is the mobility; i.e. it is approximately proportional to its length. The dependence of its length on the time is given by:

$$a \approx \exp \left(K E_o t/R + C\right)^{\frac{1}{2}} \qquad 1.3.6$$

where C is a constant that depends on the initial conditions. The thickness of the streamer increases in proportion to the square root of its length and consequently it can reach large values. However, the eye of a photographic camera with a film of insufficient sensitivity will detect the total luminosity at the maximum with a thickness $\sim$ R, and the total thickness of the streamer(ρ_{max}) (1.3.6a) will be recorded only if the photographic film is sufficiently sensitive. Lozanskii and Firsor note that if the speed of the positive or negative end of the streamers are not equal, then the neck of the streamer becomes smeared out or disappears completely.

$$\rho_{max} \approx 0.83 \sqrt{aR} \qquad 1.3.6a$$

Allowing for the finite conductivity in the streamer, if the field intensity within the streamer is E', then the field intensity on its end will be:

$$E_a = (E_o - \bar{E}')\ a/R \ln \left(\frac{2}{e}\sqrt{a/R}\right) + E' \qquad 1.3.7$$

where it is assumed $E' \ll E_0$ and where $\bar{E}'$ is the average value of E'. The surface

charge is given by:

$$\sigma = (E - E') / 4\pi \qquad 1.3.8$$

Lozanskii and Firsov also calculated the fraction θ of the total energy released in a streamer $\theta\ E^2/8\pi$ and show that when streamer propagates, the energy released in unit volume for ionization, excitation, etc. is $E^2/8\pi$.

Assume that the fraction due to ionization is $\theta\ E^2/8\pi$. The value of θ is known if the Townsend ionization coefficient α is known. In the absence of space charge, the fraction of the energy going to ionization is α Ui/E where Ui is the ionization potential. In the presence of a streamer, the electrons move in different field, θ is determined by:

$$\theta = \frac{8\pi Ui}{E^2 KE} \int_0^E \frac{\alpha(E)\ KE\ dE}{4\pi} = \frac{2\ Ui\ \alpha(E)}{B + 2E} \qquad 1.3.9$$

B is found from $\alpha = A \exp(-B/E)$ (for air at atmospheric pressure $B \approx 200$ KV/cm. Using this $\theta \approx 0.1$ and changes strongly with changing E).

Since $\theta\ E^2/8\pi = nUie$ (where n and e are the electron concentration and charge), the field within the streamer is given by:

$$E' = 2\ Ui/\theta a$$

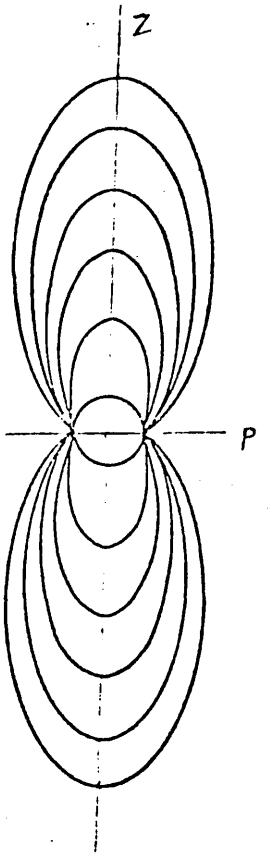

Fig. 1.3.1 Streamer geometry assumed in Lozanski model (1969)

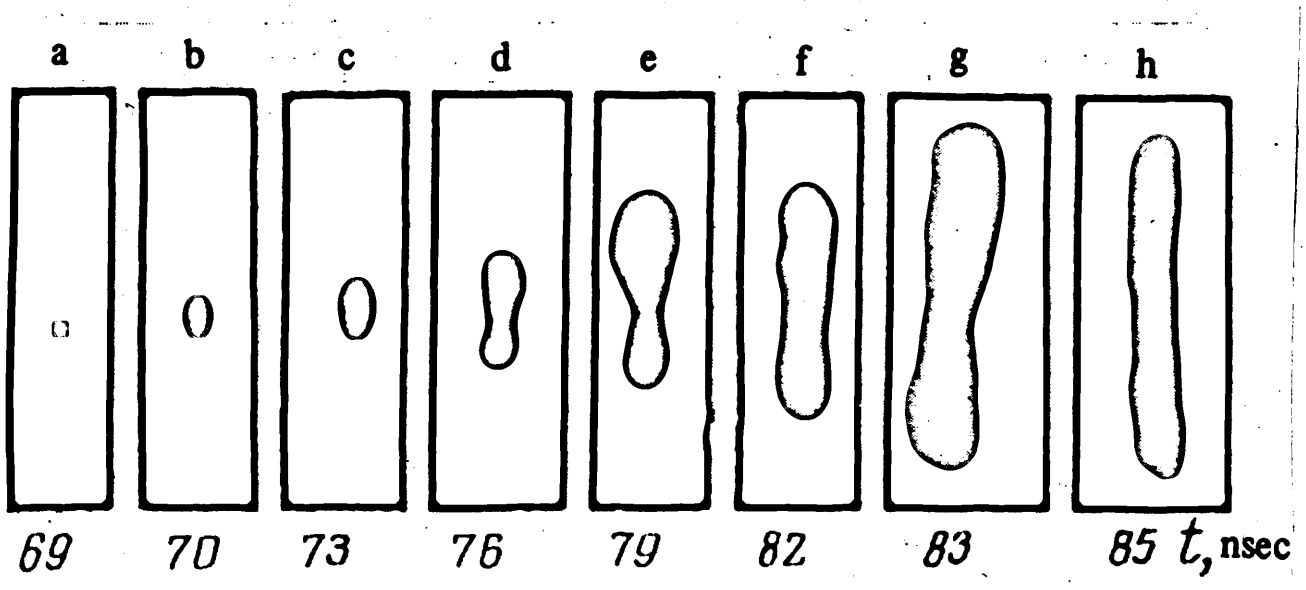

Fig. 1.4.1 Successive stages in the development of a discharge E_o = 6.6 KV/cm. Rudenko and Smetanin (1972)

For air when a = 0.1 cm, E' = 3KV/cm which is about 10% of the breakdown field intensity. Thus the larger a, the better the condition $E' \ll E_o$ is satisfied at the end of the streamer. However the current density increases in proportion to a, but at each point on the streamer λ remains constant in the first approximation, where $\lambda = e\, n\, k$ is the conductivity.

This leads to a field intensity comparable with the applied field and to development of ionization inside the streamer. At a larger streamer length when n reaches a value of the order of 1% of the gas concentration, Spitzer conductivity, which does not depend on the further increase of n, sets in. If the streamer were to remain stable, then the Spitzer conductivity in air would set in at a =10cm. If the streamer became unstable at a < 10 cm, then such a conductivity can occur earlier. The presence of finite conductivity apparently is the main cause of the temporal stability of the streamer. The growth of a thinner streamer from the head of the main streamer is accompanied by a sharp increase of the current density, whereas the conductivity cannot follow the growth of the current. This causes a drop in field intensity at the head of the thin new streamer, and hinders its further development.

1.4 Experimental Studies

Experimental studies by Davidenko et al. (1969) have been held to support the Lozanskii model. They used an image converter to study the development of an electrical discharge in pure neon and in neon with a molecular impurity. They measured the rate of development of direct and reverse streamers as a function of the electrical field strength, and the streamer length, and they found that

the linear dependence obtained by them for the velocity of the reverse streamer as a function of its length is in good agreement with the discharge mechanism proposed by Lozanskii. The very existence of streamers in pure neon supports the photo-ionization mechanism.

Rudenko and Smetanin (1972) have also astudied streamers in neon. An electron-optical method has been used to study breakdown in neon occurring in the centre of a discharge gap caused by cosmic ray tracks. They determined the time characteristics of the processes. In their studies, high voltage pulses (30 - 100 KV) with a variable rise time of 2-10 nsec, and 100 nsec, duration were applied to a 38 mm, gap chamber. Photographs of the streamers as a function of time, were obtained by means of a pulsed electron-optical image converter. The photographs Fig. 1.4.1 showed first that the growth of the avalanche head towards the anode in a field of 6.6 KV/cm. At 76 nsec. the sudden appearance of the cathode streamer can be seen. Thus in neon the electron avalanche transfers to an anode streamer before the appearance of the cathode streamer. At this instant a large current flows in the external circuit and they register a sharp drop in the field. At a later stage: a moment arrives when the decline in field strength levels off, and this moment appears to coincide with an increase in acceleration of the streamer fronts.

The observed monotonic rise in streamer velocity with increasing length is in good agreement with the mathematical model proposed by Lozanskii. Wagner (1966) also observed two stages in the growth of cathode-directed streamers in nitrogen. This was interpreted as being due to photo-ionization at the cathode.

In Rudenko and Smetanin case, processes at the cathode cannot effect the development of the streamer, since the dimensions of the discharge gap were considerably greater than the streamer length at which the acceleration sets in.

The existence of similar steps in oscilloscope traces of breakdown of medium gaps has been observed by Allen and Phillips (1964) and has been associated with transitions from the avalanche (Townsend) type of breakdown to streamer breakdown. However, in the Rudenko and Smetanin case these steps can be explained only by processes in the developing streamer without a change in the type of discharge.

Bulos et al. (1967) have investigated the dependence of streamer length and brightness on the parameters of the high voltage pulse experimentally. They photographed cosmic ray tracks in a streamer chamber on Kodak 2475 film both directly and with an image intensifier. Various pulses ranging in duration from 7 to 22 nsec, and in amplitude from 11 KV/cm to about 22 KV/cm were tried, and for each pulse the f-number was increased. They assumed that the square of the f-number at cut-off (i.e. well past the point at which streamers on the average become too faint to be practically useful) was proportional to the brightness B in the view perpendicular to the field and proportional to the total light output TL in the view along the field. Then they assumed that each of the properties L (streamer length), B and TL followed a power law of the electric field E in KV/cm and of pulse duration τ in nsec.

$$\text{property} \propto E^{X_i} \tau^{Y_i} \qquad 1.4.1$$

The best values of X and Y were given in table 1.4.1.

Table 1.4.1

Property	X	Y
streamer length L	4.7 ± 0.9	1.6 ± 0.32
streamer brightness B	2.4 ± 0.6	-0.09 ± 0.23
total light TL	5.2 ± 1	1.3 ± 0.38

1.5 Development of Streamer Chamber as Particle Detector

The streamer chamber is a recent addition to the class of charged particle detectors in which the particle track is made visible. In this chamber, which normally contains a noble gas, the path of a particle may be depicted by a line of streamers. These develop from the [illegible] of original ionization when a high voltage pulse is applied to electrodes surrounding the gas volume. Typically fields of 20 KV/cm are applied for 30 nsec.

The main advantages of this detector are its very small time resolution, its rapid cycling rate, its isotropic response to particle directions, its multiple track efficiency, its track following capability, and that it can be triggered which makes it possible to record only selected events.

The Cloud chamber triggered by Geiger counters was the standard device for particle detection in the 1930's. But it has two serious drawbacks; the device is slow to set in operation, and ionization trails persist for a large fraction of a second, with the result that the number of incoming particles must be limited,

otherwise chamber pictures may contain more tracks than one can read.

The bubble chamber developed by Glaser in early 1950's has an important virtue that it can be filled with various liquids such as liquid hydrogen, liquid propane, etc. But the bubble chamber has a serious disadvantage; it cannot be triggered. It is used exclusively with large accelerators; a timing sequence expands the chamber before the bursts of particles arrives.

The early history of the spark chamber has been reviewed by Roberts (1961). Keuffel (1949) was the first to observe that the discharge between parallel plates caused by the passage of a particle is physically located along the path of the particle. Bella and Franzinetti (1953) published the first photographs of a spark discharge.

In 1957, Cranshaw and de Beer introduced the method widely employed today of applying the high voltage to the chamber in the form of a pulse immediately after the passage of a selected particle, and made an efficient spark chamber with six one cm gaps. They also used a clearing field to remove ions older than a few microseconds. They used air which meant that if many simultaneous particles traversed the chamber only one track would be observed. Fukui and Miyamoto (1959) showed that simultaneous tracks could be recorded if noble gases were used and if the rise time of the high voltage pulse was sufficiently short.

Furthermore, a consequence of using noble gases was that in a reasonable gap (2 cm) the sparks actually followed the line of the ionized trail, rather than the electric field. This phenomenon led to the development of the wide gap chamber by Alikanian et al. (1963), in which clear spark trails of 20 cm or more could be obtained.

Chikovani et al. (1963) realised an essentially new method of operation - the streamer chamber. Similar operational conditions were realised later by Dolgoshein et al. (1964). Unlike spark chambers, the streamer chamber cuts off the development of streamers at an early stage due to the shortness of the high voltage pulse. The path of the particle is made visible. Large tracks lengths can easily be obtained in streamer chambers. Its ability to reproduce tracks in space with a high resolution combined with its ability to register equally well both single particles and large groups of particles as well as particles produced within the chamber makes it a very important device as a particle detector. The modes of operation of this chamber are described in chapter 4.

The most recent addition to this family of instruments is the avalanche chamber reported by Gygi and Schneider (1966) using an almost triangular pulse of 300 KV amplitude and 5 nsec, base length across a chamber of 10 cm, gap width. They were able to limit the discharge at the avalanche stage, to a single avalanche of about 1 mm, i.e. the growth into a streamer was prevented. Since the light output was not enough for photography an image intensifier has to be used.

CHAPTER 2

2.1 Theories of Multiple Scattering

When a charged particle, as the result of passing through a thickness, of matter is scattered through an angle, the scattering distribution can be divided roughly into two regions:

(a) The region of multiple scattering in which distant collisions yield small deflections.

(b) The region of large angle scattering where the effect of single close collisions predominates.

Williams 1939 suggested that this small angle scattering could be accounted for by multiple Rutherford scattering.

When the impact parameter is greater than the nuclear radius, the scattering occurs in the Coulomb field of the scattering atom; the scattering would be the accumulated effect of a number of small deflexions produced by successive nuclei in the scatterer. In his theory Williams assigned two limits for the extreme collision distances. The most simplifying features are:

(1) The average deflexion is mainly contributed to by scattering through small angles.

(2) The Gaussian distribution representing the multiple scattering is nearly complete before the region of single scattering is reached.

(3) Williams considered the case in which the measured scattering is the projection of the deflexion on a plane perpendicular to the line of sight, and containing the original direction.

In a field-free space a particle moving with velocity v parallel to a direction x, may be represented by the infinite plane wave - A exp (ix/λ) where $2\pi\lambda$ is the De-Broglie wave length. In the presence of a scattering field in which the potential of the particle is V(r), the solution will be of the form.

$$\psi = A \exp(ix/\lambda) + \psi_1 \qquad 2.1.1$$

ψ_1 represents the effect of the field.

For low velocities ψ_1 is determined by the Schrodinger non-relativistic wave equation.

$$\nabla^2 \psi_1 + (2M/\hbar^2) E\psi_1 = (2M/\hbar^2) V (A \exp(ix/\lambda) + \psi_1) \qquad 2.1.2$$

where $E = \frac{1}{2} Mv^2$.

If the scattering field is sufficiently weak the term $V\psi_1$ may be neglected (Born approximation), the solution for ψ_1 at large distances R from the scattering field is given by

$$\psi_1 (R) = \frac{A}{R} \frac{M}{2\pi\hbar^2} \int V(r) \exp\left(i(x + |R - r|)/\lambda\right) d\tau_r \qquad 2.1.3$$

This means that the scattered wave at R may be obtained by supposing that every element of volume $d\tau_r$ of the field scatters waves of amplitude $(M/2\pi\hbar^2)$ $V\, d\tau_r/R$, the phase of the secondary wave being the same as that of the primary wave at the point of scattering r. For a field that is spherically symmetrical the probability $I(\theta)$ of scattering through an angle θ per unit solid angle per incident particle per unit area, according to 2.1.3 is:

$$I(\theta) = (\psi(R, \theta)^2 R^2/A^2 = (2M/\mu\hbar^2)^2 f^2 \qquad 2.1.4$$

$$f = V(r) \; r \sin\mu_r \, dr \qquad \mu = 2 \sin \tfrac{1}{2}\theta/\lambda$$

For the scattering of a particle of charge e by a nucleus of charge Ze, the probability is:

$$I(\theta) = Z^2 e^4 / (4 M^2 v^4 \sin^4 \tfrac{1}{2}\theta) \qquad 2.1.5$$

which is the Rutherford scattering.

If the field deviates from coulombian, the modified scattering may be obtained by evaluating 2.1.4 for the modified field. These are well known results in the non-relativistic theory of scattering.

For the requirements of relativistic theory, where small angle scattering is concerned, equation 2.1.4 may be used, if the relativistic expression for the mass is inserted.

In Dirac's relativistic theory of electrons there is a term representing the effect of spin which is negligibly small at distances from the nucleus large compared with $\lambda\!\!\!^{-}$. This simplifies the theory of small angle scattering. Thus for small angles

$$I(\theta) = (Z^2 e^4 / 4m^2 v^4 \sin^4 \tfrac{1}{2}\theta) \qquad 2.1.6$$

$$m = M/(1 - \beta^2)^{\frac{1}{2}} \quad \text{and} \quad v = \beta c$$

Using the approximations $2 \sin \frac{1}{2}\theta \approx \theta$ and $\cos \frac{1}{2}\theta \approx \theta$ in equation 2.1.6.

$$P(\theta)\, d\theta = 2k\, d\theta/\theta^3 \qquad 2.1.7$$

$$k = 4\pi N t Z^2 e^4 / m^2 v^4 \beta^4 c^4 \qquad 2.1.8$$

where t is the thickness of the scatterer, and N is the number of atoms per c.c.

The distribution of the projected deflexion ϕ is

$$P(\phi)\, d\phi = K\, d\phi/\phi^3 \qquad 2.1.9$$

Where ϕ is the projection of θ on the plane perpendicular to the line of sight, this plane contains the initial direction. The probability of a particle being scattered through an angle between ϕ and $\phi + d\phi$, can be expressed as a sum of two probabilities.

$$P(\phi)\, d\phi = G(\phi)\, d\phi + S(\phi)\, d\phi \qquad 2.1.10$$

$G(\phi)$ represents the Gaussian distribution, and $S(\phi)$ represents the Rutherford distribution of single scattering. Introducing an angle ϕ_1, such that in traversing the plate the particle experiences on the average one collision which deflects it more than ϕ_1, where

$$\phi_1^2 = \tfrac{1}{2}K. \qquad 2.1.11$$

For angles less than ϕ_1, the Gaussian distribution is predominant, and for angles greater than ϕ_1, the Rutherford distribution is.

The angle ϕ_{max} is the greatest single-angle scattering which can contribute to the observed deflextion and physically it is determined by the finite size of the nucleus. Williams takes the angle ϕ_1, as the first approximation to ϕ_{max}.

The mean absolute deviation

$$\langle\phi\rangle = \delta\,[\log(\phi^2_{max}/\phi^2_{min})]^{\frac{1}{2}} \qquad 2.1.12$$

where $$\delta = \sqrt{k} = 2e^2 (Nt)^{\frac{1}{2}} Z/Pv \qquad 2.1.13$$

and $$\phi_{max} = (\pi/2)^{\frac{1}{2}}\, \delta \qquad 2.1.14$$

and $$\phi_{min} \sim \chi/a , \qquad a = Z^{\frac{1}{3}} a_o . \qquad 2.1.15$$

a_o is the radius of the first Bohr orbit of the hydrogen atom; ϕ min, is the effective minimum angle, its magnitude is determined by the screening of the field by the orbital electrons. In deriving the basic single scattering formulae using the Fermi-Thomas statistical model of the atom, to allow for the screening effect, Williams considered separately the cases $\alpha = Z/137\beta \ll 1$ where the Born approximation is valid, and $\alpha \ll 1$ (classical).

For $\alpha \ll 1$

$$\begin{aligned} \phi_{min} &= 1.75\,(\lambda/a) \\ &= 1.75\, mc\, Z^{\frac{1}{3}}/137\, P \end{aligned} \qquad 2.1.16$$

Thus

$$(\log (\phi^2_{max}/\phi^2_{min}))^{\frac{1}{2}} = (\log 2\pi\, Z^{4/3}\, Nt\hbar^2/3.1\, mc^2\beta^2)^{\frac{1}{2}}$$

$$= (\log M)^{\frac{1}{2}} \qquad 2.1.17$$

For $\alpha \ll 1$

$$Mcl = 0.2\pi Nt\, Z^{-2/3} (\hbar^2/mc^2)^2 \qquad 2.1.18$$

M is the average number of collisions.

These assumptions give the mean deviation

$$\bar{\theta} = \delta\, (\log M)^{\frac{1}{2}} \qquad 2.1.19$$

Allowing for deflections greater than $\emptyset$ max, the arithmetic mean deflection is:

$$\bar{\theta}_1 = (3.69 + 0.28 \log (Z^{4/3} \rho t/A\beta^2)) \delta \qquad 2.1.20$$

Where ρ is the density of the scattering material, and A is the atomic weight. Williams considered the effect of the nuclear size, and the mean deflection is expressed by

$$\bar{\theta} \text{ mean} = (19.5 - 3.1 \log Z) \delta \qquad 2.1.21$$

The root mean square scattering angle is given by

$$\bar{\theta} \text{ r.m.s.} = (1.45 \delta + 0.80 \bar{\theta}) \qquad 2.1.22$$

Other multiple scattering theories, which are mathematically closely related have been published. They are the work Moliere (1948) Snyder and Scott (1949), Goudsmith and Saunderson (1940) Lewis (1950), Nigam et al., 1955, Nigam 1963 and Cooper and Rainwater (1955). All these theories gave results within few percent of William's theory.

Moliere (1948), and Snyder and Scott (1949), use the approximation of small angle scattering and hence an expansion of Bessel functions; for the distribution of projected angle a Fourier integral was used. Goudsmith and Saunderson developed a theory valid for any angle by means of an expansion in Legendre

polynomials; Lewis starts from the Legendre expansion and then goes over to the limit of small angles, thus establishing the connection between the first three methods. Nigam et al., (1959, 1963) used Dalitz (1951) relativistic expressions for single scattering cross sections derived in the second Born approximation.

In the Moliere's multiple scattering theory the nucleus is treated as a point charge; he shows that the scattering depends only on a single parameter describing the screening of the atom. The angular distribution depends on the parameter, which is given by

$$\exp(b) = \frac{6680t}{\beta^2}\left(Z^{\frac{1}{3}}(Z+1)\, z/A\,(1+3.34\,\alpha^2)\right) \qquad 2.1.23$$

b depends essentially on the thickness of the scattering plate in gm/cm^2 and is nearly independent of Z.

t is the thickness in gm/cm^2, A is the atomic weight, z is the charge of the scattered particle and α^2 is the deviation from the Born approximation.

Equation 2.1.23 shows that the effective number of collisions per gm/cm^2 is (nearly independent of Z), i.e. almost the same for all elements.

Bethe (1952) shows that the theory of Goudsmith and Saunderson has a close quantitative relation to that of Moliere, and a good approximation to their distribution function can be obtained by multiplying Moliere's function by $(\theta/\sin\theta)$. This relation holds until the scattering angle becomes so large

that only very few terms in the series of Goudsmith and Saunderson need to be taken into account.

Snyder and Scott calculated the distribution of projected angles; Goudsmith and Saunderson that of the total scattering angle; and Moliere both.

Olbert (1952) modified Moliere's theory of multiple scattering by considering the finite nuclear size. He assumed that the probability of single scattering goes abruptly to zero for angles greater than $\varphi_o = \varphi_m a/r_n$, where a is the radius of the statistical Thomas-Fermi atom, r_n is the radius of the nucleus, and φ_m is the screening angle given by Moliere.

Cooper and Rainwater (1955) described two methods for calculating the multiple scattering distribution for projected angle scattering. The single scattering law for projected angle is taken to be the Rutherford scattering law for projected angles, modified at small angles by electron shielding, and at large angles by a nuclear form factor $F(\varphi/\varphi_o)$ which gives the effect of the finite nuclear size.

Cooper and Rainwater described a way which consists of folding together several simpler distributions in a manner somewhat analogous to the actual effect of successive layers of the scatterer. The method is based on the observation that if $f(\varphi)\, d\varphi$, the probability of a single scattering through φ to $\varphi + d\varphi$ to one side in projected angle, is given, then the multiple scattering distribution $M(\varphi)$ is completely defined. Furthermore, if the actual scattering slab were replaced

by a series of consecutive slabs A, B, C, ... having a single scattering laws $f_A(\varphi) + f_\beta(\varphi)$ ..... where

$$f(\varphi) = f_A(\varphi) + f_\beta(\varphi) \cdots$$

Then the same multiple scattering distribution results on traversing all the slabs in series. If $M_A(\varphi)$, $M_\beta(\varphi)$, ... are the separate multiple scattering distributions for A, B, ... then $M(\varphi)$ results on folding MA, MB, ... together. For the case of two components

$$M(\varphi) = \int_{-\infty}^{\infty} M_A(\varphi_1)\, M_\beta(\varphi - \varphi_1)\, d\varphi_1 \qquad 2.1.24$$

For small φ $\quad \sin\varphi = \tan\varphi = \varphi$

The distribution law for small angles is just the Rutherford scattering law modified because of electron shielding. Following Moliere, they represent this as

$$f'(\varphi) = \tfrac{1}{2} Q (\varphi^2 + \varphi_m 2)^{3/2} \qquad 2.1.25$$

where φ is the projected angle and φ_m is the screening angle, given by

$$\varphi_m = \frac{1.14\, mec^2\, Z^{\frac{1}{2}}}{137\ cP} \left[1.13 + 3.76\left(\frac{Z}{137\beta}\right)^2 \right] \approx \lambda/a \qquad 2.1.26$$

and $\quad Q = 4\pi (Nt/A) \quad (Z e^2/Pv)^2 \qquad 2.1.27$

Here (Nt/A) gives the scatterer thickness in atom/cm^2, p is the momentum of the incoming particle, $\lambda = h/p$, v is the velocity, a is the Fermi-Thomas radius of the atom where $a = 167 \times 10^4 Z^{-\frac{1}{3}} (e^2/m_e c^2)$ and m_e is the electron mass, the charge of the particle is taken to be singly charged.

$$Q = \frac{x}{4X} \left(\frac{Es}{vp} \right)^2 \frac{1}{\ln (191 Z^{-\frac{1}{3}})} \qquad 2.1.28$$

where x is the thickness in gm/cm^2, Es is the characteristic energy for scattering which is equal to $21 Z'^2$ MeV, where Z' is the charge of the scattered particle.

$$1/X = \frac{4e^2}{\hbar c} \frac{NZ(Z+1)}{A} r_e^2 \ln (191 Z^{-\frac{1}{3}}) \qquad 2.1.29$$

where N is Avogadro number and r_e is the classical electron radius.

The modification in the above distribution at large angles is given by multiplying $f'(\varphi)$ by $F_N(\varphi/\varphi_o)$ to give

$$f(\varphi) = \tfrac{1}{2} Q (\varphi^2 + \varphi_m 2)^{-2/3} F_N(\varphi/\varphi_o) \qquad 2.1.30$$

The term $F_N(\varphi/\varphi_o)$ is the nuclear form factor, which contains a part representing elastic coherent scattering plus a part representing inelastic scattering.

In the first method they treat the multiple scattering from extended nuclei as a correction to the Moliere theory by setting $F_N = [1 + (F_N - 1)]$, where $(F_N - 1)$ gives the correction term. This is the method used by Olbert for his step up function. Such a treatment yields satisfactory results for small angles, but is inconvenient for large angles where the second method is preferred.

Equation 2.1.30 is written

$$f'(\varphi) = \tfrac{1}{2} Q (\varphi^2 + \varphi_m 2)^{-3/2} [1 + (F_N - 1)] \qquad 2.1.31$$

Then

$$g(\zeta) - g(O) = \frac{Q}{2} \int_{-\infty}^{\infty} \frac{(e^{i\zeta\varphi} - 1)}{(\varphi'^2 + \varphi_m 2)^{3/2}} \frac{F_N(\varphi/\varphi_o)}{} \, d\varphi$$

$$+ \frac{Q}{2} \int_{-\infty}^{\infty} \frac{(e^{i\zeta\infty} - 1)(F_N - 1)}{(\varphi^2 + \varphi_m 2)^{3/2}} \, d\varphi \qquad 2.1.32$$

Introducing Moliere parameters x, η, G as defined

$$x = (2GQ)^{-\frac{1}{2}} \varphi \qquad 2.1.33$$

$$\eta = (2GQ)^{\frac{1}{2}} \zeta \qquad 2.1.34$$

where G is the solution of

$$G = -\tfrac{1}{2} \ln\left(\frac{\gamma^2 \varphi_1^2}{2 G \varphi_e}\right) \qquad 2.1.35$$

γ is Euler constant

G is given numerically by

$$G = 5.66 + 1.24 \log\left(\frac{Z^{4/3} A^{-1} \times \text{gm/cm}^2}{1.13 \beta^2 + 3.76 (Z/137)^2}\right) \qquad 2.1.36$$

putting these values in equation 2.1.32 and using the fact that G is reasonably large (for moderate foil thickness G varies between 7 and 15), and after performing the integration over η

$$M_2(x)\,dx = \frac{\exp(-x^2)\,dx}{\sqrt{\pi}} + \frac{dx\,[f(x,\infty) - k(x)]}{4G} \qquad 2.1.37$$

where
$$k = \frac{1}{\sqrt{\pi}} \int_0^\infty dx' \frac{[1 - F_N(x'/x_o)}{(x'^2 + x_m^2)^{3/2}} \Big[\exp[-(x + x')^2] + \exp[-(x - x')^2] - 2\exp(-x^2)\Big] \qquad 2.1.38$$

and
$$f(x,\infty) = \frac{1}{\pi} \int_{-\infty}^{\infty} d\eta \exp(i\eta x - \eta^2/4)\,(\eta^2/4 \ln \eta^2/4) \qquad 2.1.39$$

In the second method they consider the Fourier transform of the single scattering law.

$$g(\zeta) - g(o) = \frac{Q}{2} \int_{-\infty}^{\infty} \frac{(e^{i\zeta\varphi'} - 1)\, F_N(\varphi'/\varphi_o)\, d\varphi'}{(\varphi'^2 + \varphi_m^2)^{3/2}} \qquad 2.1.40$$

Introducing the Moliere parameters, x, η and G

$$g\left(\frac{\eta}{(2GQ)^{\frac{1}{2}}}\right) - g(o) \equiv S(\eta)$$

$$= \tfrac{1}{2} G \int_{o}^{\infty} \frac{(F_N(x'/x_o)(\cos \eta x' - 1)}{(x'^2 + x_m^2)^{3/2}}\, dx' \qquad 2.1.41$$

$$M_2(x)\, dx = \frac{dx}{2\pi} \int_{-\infty}^{\infty} e^{i\eta x}\, e^{S(\eta)}\, d\eta \qquad 2.1.42$$

Equation 2.1.41 is the Moliere-Fourier transform if $F_N(x/x_o) = 1$. In the case of point nucleus this integral is evaluated through the observation that there exists an angle $x' = k$ at which the integral can be split.

Splitting the integral in 2.1.41 and performing the integration and then substituting the value of $S(\eta)$ in 2.1.42

$$M_2(x) = \frac{\exp(-x^2)}{\sqrt{\pi}} \left[1 + \frac{1}{4G}\, 2(2x^2 - 1) \ln(k/1.26) \right]$$

$$+ \frac{1}{4G} \frac{1}{\sqrt{\pi}} N(k, x) \qquad 2.1.43$$

where $$N(k, x) = \int_{k}^{\infty} \frac{F_N(\lambda/xo)\, T(x, \lambda)}{\lambda^3}\, d\lambda \qquad 2.1.44$$

$$T(x, \lambda) = \exp[-(x + \lambda^2)] + \exp[-(x - \lambda)^2] - 2\exp(-x^2) \qquad 2.1.45$$

After some labour, they obtained the final formula:

$$M_2(x) = \frac{\exp(-x^2)}{\sqrt{\pi}} \left[1 + \frac{q(L, x)}{4G} \right]$$

$$+ \frac{1}{4G} \frac{1}{\sqrt{\pi}} \int_L^\infty \lambda^3 F_N(\lambda/\lambda_o)\, T(x, \lambda)\, d\lambda \qquad 2.1.46$$

where $$q(L, x) = 2(2x^2 - 1)\left[\ln \left(\frac{L}{1.26} \right) + \int_o^{2Lx} \frac{\cosh t - 1}{t}\, dt \right]$$

$$+ 6x^2 - \frac{1}{L^2}(\cosh 2Lx - 1) - \frac{2x}{L} \sin 2xL \qquad 2.1.47$$

and $$\int_o^{2Lx} \frac{\cosh t - 1}{t}\, dt = \frac{(2Lx)^2}{2.2!} + \frac{(2Lx)^4}{2.4!} \qquad 2.1.48$$

L is chosen to be equal to $\frac{1}{4}$ which is number corresponding to an angle.

The first term in 2.1.46 is William's formula, the second term indicates a correction due mainly to the screening effect, and the last term represents the nuclear-size effect and has to be evaluated numerically by taking account of

$$T(\eta, \zeta) = \exp -(\eta + \zeta)^2 \exp -(\eta - \zeta)^2 - 2 \exp(-\eta^2) \qquad 2.1.49$$

This term is important at large angles and represents the effect of single scattering.

2.2 Survey of early experimental work

Fowler and Wolfendale (1958) reviewed the scattering experiments prior to 1958. A few experiments were carried out in the momentum region $P\beta < 200$ MeV/c

from which no firm conclusion could be drawn. Although the statistics of the experiment in the region $200 < P\beta < 600$ MeV/c were rather poor, the scattering appeared to be in agreement with the theory of Coulomb multiple scattering.

In the momentum region $P\beta > 600$ MeV/c more particles were scattered through large angles than would be expected on the basis of a pure Coulomb effect. This phenomenon is known as anomalous scattering.

Since then only a few (possibly six) experiments for which $P\beta$ is less than 250 MeV/c have been reported; including one bubble chamber experiment with a lead scatterer, one counter hodoscope experiment with a lead scatterer and four multiple cloud chamber experiments with copper and iron, beryllium, lead and copper respectively. These experiments were in agreement with the theory. The other experiment was a streamer chamber with a 2.5 cm lead scatterer which was not in agreement with the theory (see Table 2.2.1).

For momentum $P\beta > 250$ MeV/c only a few experiments have been reported; in all these experiments the results were in good agreement with the theories. Table 2.2.1 lists the previous experiments and their results. It may be seen that the observed amount of multiple scattering in some of the experiments does not agree with the theoretical values. The disagreement is generally in the case of lower energy particles scattered in thick specimens of heavy materials.

For muons scattered through 1 cm thickness of lead, at lower energies, the measured value of θ rms has been smaller than theoretically predicted, as has been found by Sinha (1945), Crewe (1951) and Mishra (1969). However, Meyer (1961) and Sen Gupta et al., (1962) observing the multiple scattering of muons in the same energy region, found out that the experimental value was in good agreement with the theoretical one.

In most the experiments in which the results were in good agreement with those predicted, the scattered particle has been identified as a muon. From table 2.2.1 there are only a few experiments in the same momentum range as the one studied in this work; and since their results conflict no decisive conclusions can be drawn on the agreement of the experimental results with the theories of multiple scattering.

Table 2.2.1 List of earlier work on multiple scattering of Muons

Author	Scatterer	Energy	Method	Agreement
1. Wilson, J.G. (1940)	0.3 + 1 cm lead 2 cm copper and 2 cm Gold	$E < 2$ GeV	expansion chamber	yes
2. Code, F.L. (1941)	3.8 cm of Tungsten	mean $\bar{E} = 2.14 \times 10^4$ ev. degree	counter controlled Cloud chamber	yes
3. Shutt, R.P. (1941)	1 + 5 cm of lead	All over cut off of 15 cm lead	Cloud chamber	no
4. Sinha, M.S. (1945)	2 cm of lead	$55 < E < 130$ MeV	Cloud chamber	no
5. Crewe, A.V. (1951)	2.54 cm of lead	$E = 184 \pm 12$ MeV	Cloud chamber	no
6. Whittemole Wandshutt, R.P. (1952)	5 cm of lead	$0.3 < P < 3.1$ BeV/c	Cloud chamber	yes
7. George, E.P. et al.(1953)	2 cm lead	all $E > 100$ MeV at a depth of 60 m.w.e.	Cloud chamber	no
8. Leontic, B and Wolfendale A,W. (1953)	6 plates 2 cm of lead	all spectrum after passing in 100 cm of lead filter	Multiplate Cloud chamber	no
9. Lloyd, J.L. and Wolfendale, A.W. (1955)	54.7 gm/cm^2 iron 50.9 gm/cm^2 lead	$0.5 < P < 20$ GeV/c	Cloud chamber	yes

10. Nash, W.F. and Pointon, A.J. (1958)	2 plate 2 cm lead + 5.8 cm of copper	$P > 0.5$ GeV/o $P > 0.7$ GeV/c	Cloud chamber	yes
11. Kirillov-Vhrymov, V.G. et al. (1958)	4 m copper 4 mm Iron	$85 < P < 144$ MeV/c $81.2 < P < 135$ MeV/c	Cloud chamber	yes
12. Alikanian, A.I. et al. (1954)	7 mm lead	$100 < P < 180$ MeV/c	Mass spectrometer with cloud chamber	yes
13. Chidley, B. et al. (1959)	0.22 inch of lead	$E = 23$ MeV	probane bubble chamber	yes
14. Meyer, M.A. et al. (1961)	2 cm lead and 4 cm of lead	$160 < P < 1020$ MeV/c divided in 4 ranges	A counter hodo-scope	yes
15. Sen Gupta, S.N. and Sinha, M.S. (1962)	0.25 inch copper	$40 < P < 170$ MeV/c	Multiplate cloud chamber	yes
16. Meyer, M.A. et al. (1962)	7.1 cm of Iron 4.57 cm of Tin	$298 < P < 773$ MeV/c divided in 2 ranges $248 < P < 539$ MeV/c $533 < P < 773$ MeV/c	Counter hodoscope	yes
17. Bizard, G. et al. (1964)	5 plates of 5 mm lead	$200 < P < 1500$ MeV/c momentum measured	Cloud chamber	yes
18. Bizard, G. et al. (1966)	11.33 gm/cm^2 of lead	$P = 920$ MeV/c $+35$ MeV/c -27 MeV/c	Accaustic spark chamber	yes
19. Mishra (1968)	2.5 cm of lead	≈ 100 MeV	Streamer chamber	no

20. Present work (1975)	2.5 cm of lead	≈100 MeV	Streamer chamber	no
		≈135 MeV		no
	2.5 cm of Hg	≈159 MeV	streamer chamber identified μ	yes
	2.5 cm of Pb	≈148 MeV	streamer chamber identified muons (decay electron in carbon + delay coince technique)	yes

CHAPTER 3

The Streamer Chamber

3.1 General Features

The experimental arrangement consists of the perspex chamber containing the active gas (the sensitive volume); the electronics including detectors, logic and trigger amplifiers; the high voltage generator; and the recording system (the automatic camera). Two logic systems will be described; the first used valves and the second made use of transistors and integrated circuits. Two trigger amplifiers will be described as well. The logic system using integrated circuits was developed because a need arose for a delayed coincidence facility so a decision was made to redesign the original logic system. When an automatic camera was used the need for a pulse to advance it led to the development of the transistorized trigger amplifier.

When the logic selects an event that has been detected by the counters the resulting output operates the trigger amplifier. The very fast rising output pulse of the trigger amplifier, which is a few kilovolts in amplitude, triggers the high voltage source and a high voltage pulse is then applied on the chamber. The electronic system should be so fast that the overall delay between the detection of the event and the application of the high voltage pulse on the chamber must be less than one microsecond.

3.2 Description of the Chamber

3.2.1 Mechanical Details

The sensitive volume of the chamber is 20 x 20 x 20 cm^3; it is made up of

half inch thick perspex cemented with I.C.I. tensol cement No. 7; the boxes each have a small hole on a side wall in which a perspex tube is held by clamps screwed to the side wall of the chamber. The clamp and the screws were made out of perspex. Between the wall of the chamber and the tube a rubber 'O' ring was used to make the connection vacuum tight. The inner surface opposite the sides through which the photographs were taken was painted black with Rustin black paint to minimize the back-reflected light.

The earthed electrodes were 2 ft. square, $\frac{1}{4}$ inch thick Duraluminium plates with their edges rounded off. The high voltage electrodes were 1/16 inch thick, 2 ft. square aluminium plates which had both surfaces polished, the scatterer was placed between the two high voltage electrodes. The perspex boxes and the electrodes (the whole system) were clamped together using four 2 x 3 x 37 inches wooden joists with 0.5 inch diameter hole at 3 inches from each end, through which four 30 inch long 0.5 inch diameter nylon rods threaded at both ends passed, and the whole arrangement was clamped using tufnol nuts.

3.2.2 Evacuating and filling the system

The method adopted in this work was to evacuate the chambers to about 0.03 mm of Hg before filling. Since the chambers were gas tight, it was found that one filling with gas could last several days. The system used in the present work for evacuating and filling the chambers is shown in Fig. 3.2.2.1. The tap (T1) which opens up when the gas pressure inside the chambers becomes

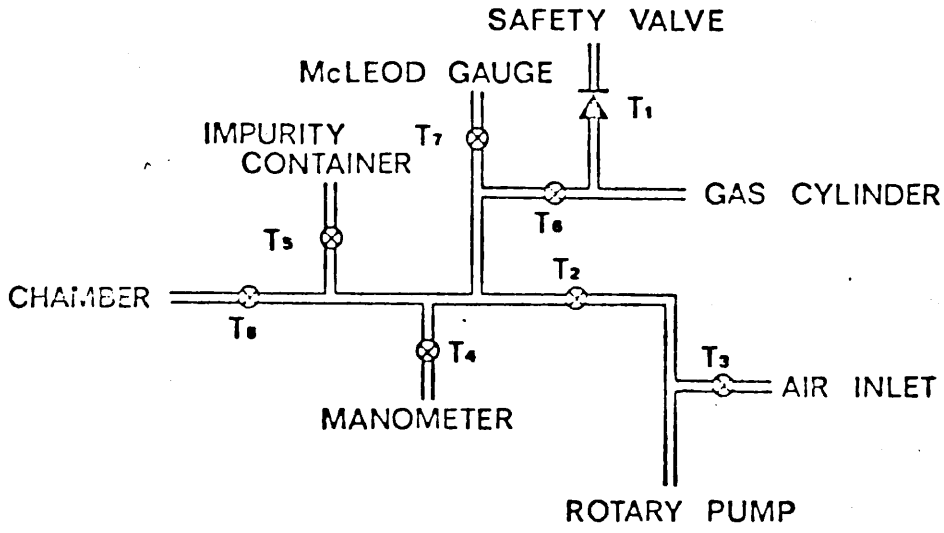

Fig. 3.2.2.1 The arrangement for evacuating and filling the system

higher than the atmospheric pressure (about 2 atmospheres) was used as a precaution to prevent explosion. A facility to introduce gas admixture to the filling gas is available through tap (T5).

With a rotary pump it was found possible to reduce the pressure inside the chambers to 20 micron of Hg. A McLeod gauge was used to measure this pressure. The chamber was filled to a pressure of 2 cm of Hg above atmospheric pressure, this was measured by the manometer. The gas used was 30% Helium and 70% Neon.

3.3 Scintillation Counters

In the experimental studies described later, cosmic ray particles have been employed. They were detected with a scintillation counter arrangement: two counters each consisted of 9 inch square, $\frac{1}{2}$ inch thick plastic scintillator NE 102A coupled by a triangular light guide to a thirteen stage photo-multiplier tube EMI 9594B. Each assembly was covered by a white sheet of polystyreen foam to reflect the photons created in the plastic scintillator and then covered by a black polythene and sealed by a P.V.C. tape to make it light tight. The light guide was a half an inch thick perspex plate, the length of the edge in contact with the scintillator was nine inches and that in contact with the photomultiplier was 1.5 inch.

The counter used for anticoincidence measurement was a larger $((50 \times 40 \times 2)\text{cm}^3)$ NE102A plastic coupled by a long light guide to a thirteen stage photo-multiplier tube E.M.I. 9594A. The light guide used was 2.5cm. thick perspex

plate, the length of the edge in contact with the crystal was 40 cm. and the other end was 4 cm.

The light guide and the plastic scintillator were covered with aluminium foil to reflect the light emitted inside the scintillator. The aluminium foil was earthed to stop electrostatic sparks and the whole assembly was made light tight by black P.V.C. The light guides in the three units were cemented to the scintillators and the photomultipliers by the use of optical cement NE580 which has a refractive index close to that of NE102A plastic scintillator.

3.4 Early Valve Circuits

When an event has been observed by the scintillation counters, the output signal initiates a sequence of operations which will result in the application of 240 KV pulse to the central plates of the chamber. This is achieved with the units described in detail in the following sections.

3.4.1 Coincidence Circuit

In the circuit used Fig. 3.4.1.1 a 6BN6 valve pentode was used; positive 6 volts pulses from the photomultipliers were applied to the control and suppressor grids which were negatively biassed. The bias voltage could be adjusted by changing R5 till there were no singles going through. For two pulses arriving simultaneously at the valve grids, a negative output pulse of about 4 volts and a rise time of 25 ns was obtained. This circuit was tested and found to operate satisfactory.

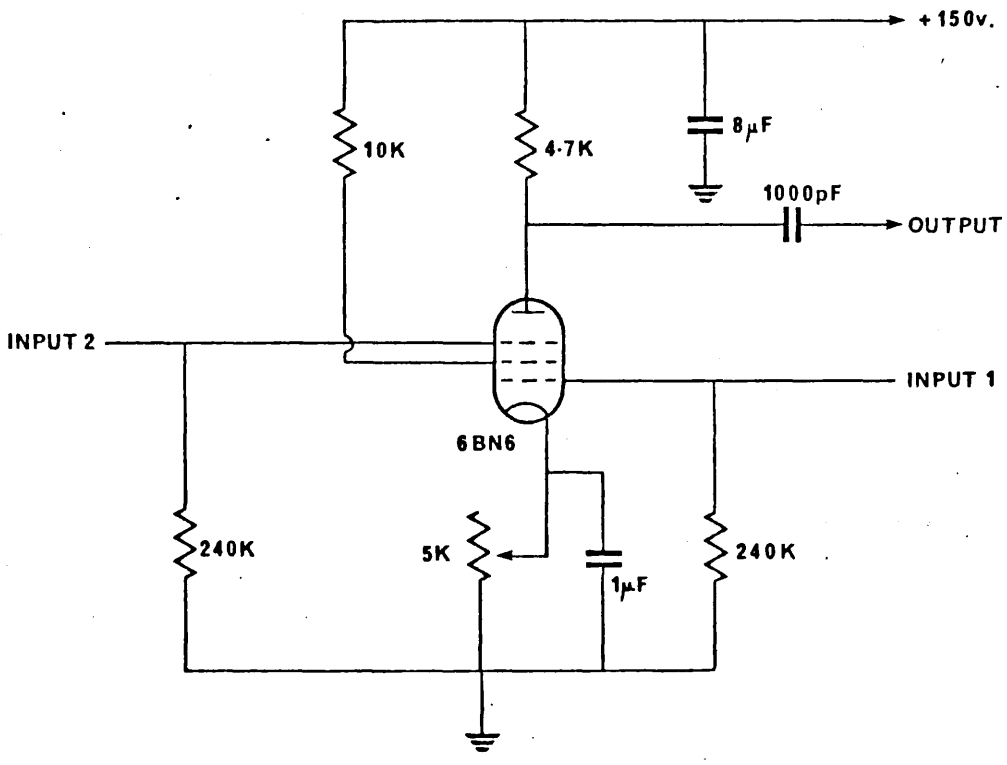

Fig. 3.4.1.1 Early coincidence circuit

3.4.2 Anticoincidence Unit

An anticoincidence arrangement was used to select a particular event; for this purpose the circuit in Fig. 3.4.2.1 was used. A negative 5 volts bias and a positive 0.5 volt bias were applied to the control and the suppressor grids. Normally the valve remained cut off; the valve became conducting when a positive pulse was applied to the control grid and no pulse was applied to the suppressor grid, and a negative output pulse of 10 volts resulted. If the two pulses were applied simultaneously no output pulses will be obtained. The negative pulses from the anticoincidence counter were lengthened and amplified. Care was taken to ensure that they arrived before the pulses from the coincidence circuit and stayed long after. For this a monostable multivibrator was used.

3.4.3 Trigger Amplifier

To obtain a negative 6 KV pulse from a negative 3 volts input pulse, the trigger amplifier described by (Rice-Evans and Mishra, 1969) was used. It consists of four stages. The first stage is a pentode (E 180 F) amplifier, whose output is a positive 20 volts which is applied to the grid of the secondary emission pentode (EFP60) of the second stage; the third stage is a cathode follower using the EL 360 to improve the rise time of the output pulse of the fourth stage which is a beam power tetrode cv 4082, which normally remains cut off. When a positive 140 volt pulse from the EL 360 is applied to the control grid, the valve becomes conducting giving rise to a negative fast rising 6 KV pulse.

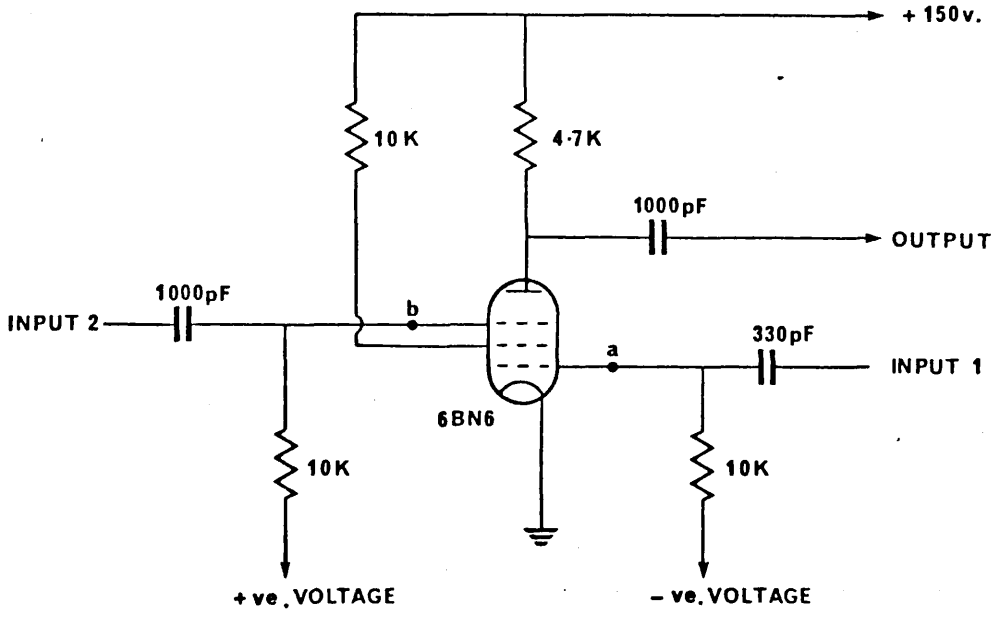

Fig. 3.4.2.1 Early Anticoincidence Circuit

3.4.4 Intermediate Spark Gap

Since the 6 KV pulse from the trigger amplifier was not sufficient to trigger Marx generator an intermediate spark gap was used. This switch consists of a storage capacitor and a spark gap. Two rapid discharge condensers 1000 pF each and 15 KV working voltage of a very low inductance were connected in series between the high voltage and earth through a 1 K resistance. The spark gap is made ot two stainless steel hemisphere electrodes each of about 2.5 cm. in diameter. The earthed electrode is a hollow with a 3 mm. hole; this hollow space was filled with tufnol having a central hole through which passed a 1 mm. diameter tungsten electrode which was connected to the trigger amplifier output. A barium titanate annulus with an inner diameter of about 1 mm. and an outer diameter of about 3 mm. was placed in the space between the earthed electrode and the tungsten wire. The barium titanate was used to intensify the field, advantage was taken of the effect that the reduction of electrical field in an insulator due to its dielectric constant and the consequent overvolting of an adjacent air gap (Lavoie et al., 1964). The high voltage applied across this gap was in the region of 25 KV. Thus when this spark gap is triggered, a 25 KV pulse is transferred to the first stage of the Marx generator.

3.5 Marx Generator

The Marx generator is a high voltage pulse generator which can be triggered. It consists of condensers which are charged in parallel and discharged in series. Such a generator consists of an array of n condensers C_o and n switches between them, the condensers are charged in parallel through a number of high

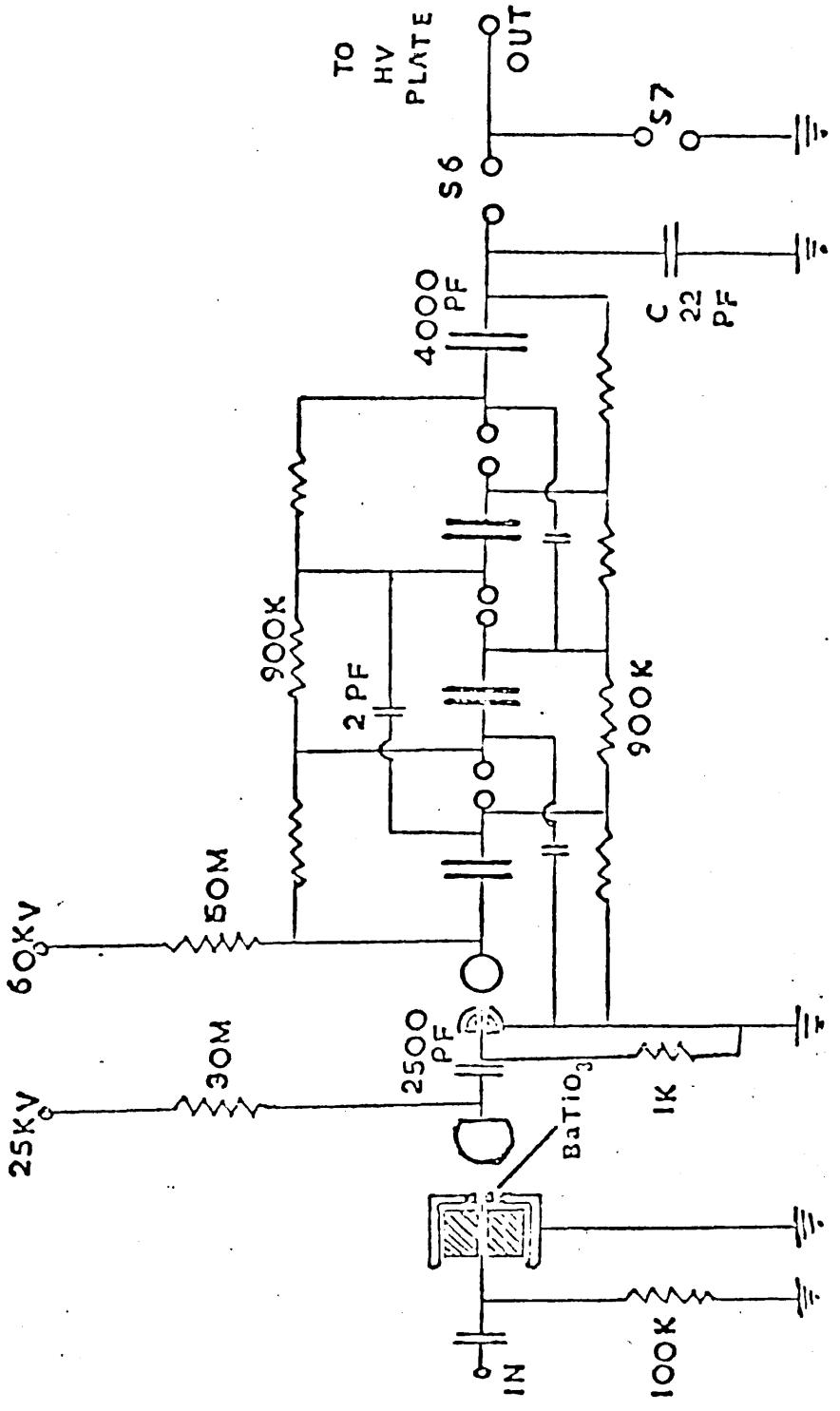

Fig. 3.5.1.1 Intermediate spark gap and the Marx generator

resistances up to a voltage V_o; the total voltage between ground and the output of the generator is zero. On closing all switches, the voltage over them adds, and a resultant output voltage V is obtained across the output terminal which is equal to nV_o. V will decay within a time interval determined by R.C. Fast switching is best realised by using spark gaps. Switching times and inductances are minimised by the use of small gap widths. The dielectric strength of a gap is determined by the electrode material, the kind of gas and its pressure.

When the first switch is closed (Fig. 3.5.1) by a trigger pulse, a step pulse of amplitude V_o is applied to the remaining gaps. To reduce the time lag between the first breakdowns one has to over volt the gaps by larger pulses. The use of a small value coupling condensers to couple the adjacent stages allows one to over volt the second gap by 100% (i.e. by V_o) independently of the number of stages.

The generator used in this work was described by Rice-Evans and Mishra, (1969). It is capable of producing 240 kV and it consists of four stages using large paper condensers 4000 PF each. The total inductance of the four capacitors is 0.8 micro Henrys; the working voltage of the charging resistors was 25 kV and they were 20 Watt resistors.

3.6 Logic control with integrated circuits

The logic control unit is described in detail in the following sections. This unit was built with integrated circuits and semiconductor devices. One of

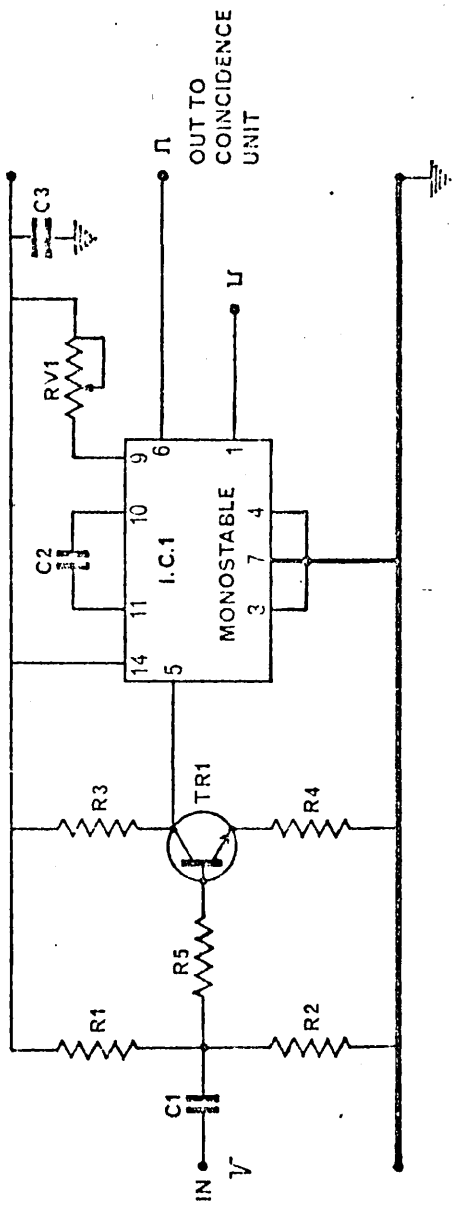

Fig. 3.6.1.1 Limiter pulse shaper

the major difficulties of using the semiconductor devices comes from the production of a heavy radiation background by the high voltage pulse generator. Even though the electronic control unit is in the same room as the generator, this difficulty was overcome by using sufficient screening around the logic unit as well as carefully selecting the components. The whole logic control unit fitted in a Harwell 2000 standard double width module.

3.6.1 Limiter/pulse shaper

A circuit diagram for this limiter/shaper is shown in Fig. 3.6.1.1. The limiter part was to protect the integrated circuit used as a pulse shaper. This unit is sensitive to 50 mV negative input pulses; the output pulse is a standard T.T.L. (Fig. 3.6.1.2). A choice of positive or negative output pulse is available. A negative anode pulse from a photomultiplier applied to the base of n.p.n. transistor which is normally conducting will turn the transistor off giving rise to a fast positive pulse whose amplitude is limited to 5 volts. The output from the limiter was shaped by a monostable SN 74121 N which gave a standard output; the width of the output pulse could be changed by varying the value of the resistance RV1.

3.6.2 Coincidence/Anticoincidence Logic

A block diagram of this unit is shown in Fig. 3.6.2.1; pulses from the limiter/pulse shapers fed to the three inputs of the first gate (NAND IC_1); the third input could be used as an inhibitor or as another input for triple coincidence work. For the present work one input was coupled to a d.c. level. When two pulses arrive simultaneously at inputs 1 and 2 an output is obtained from

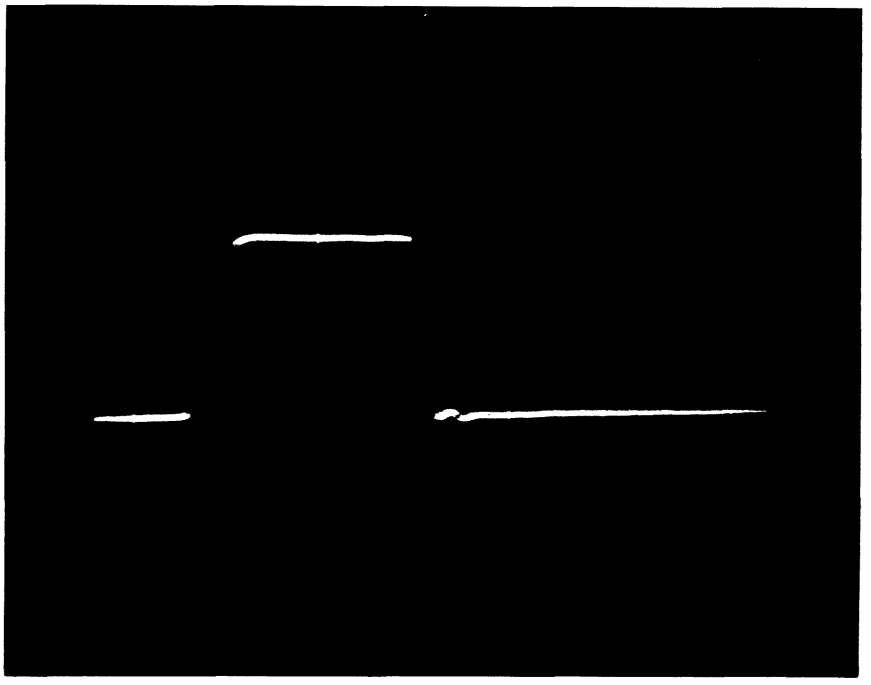

Fig. 3.6.1.2 The output pulse of the limiter pulse shaper

the first gate; this output is inverted and a delay could be used if necessary and applied to the input of the second gate (NAND 2 IC_9). If no pulse is observed simultaneously at the anticoincidence counter (IN 3) nothing is applied at the other inputs of the second gate, and a coincidence output pulse is obtained (OUT 1). If however, a pulse is observed simultaneously by the anticoincidence counter it will be inverted after the limiter/shaper and fed to the second gate to inhibit its output. So output pulses from the second gate were obtained only if two simultaneous pulses were applied to inputs 1 and 2 and no pulse at input 3. Fig. 3.6.2.2 shows a detailed diagram of the unit used.

Care was taken to ensure that anticoincidence pulses applied to input 3 arrive at the second gate before the output of the first gate and are long enough to outlast the coincidence pulse. This was achieved by taking two outputs from the fourth pulse shaper, one was inverted and applied directly to the second gate, which will insure that it will arrive first. A monostable IC_5 was used to lengthen the other pulse before it was fed to the second gate and this length could be adjusted.

This unit could be used to detect the delayed coincidence between pulses applied to input 3 and the output of the second gate (IC_9). The anti-coincidence counter was used to detect the delayed event. An output from NAND IC_1 was applied to one of the input of NAND (IC_8). The output from NAND IC_9 goes to a monostable (IC_{10}) which determines the time after which the gate (IC_8) is opened, this time could be adjusted between 1 and

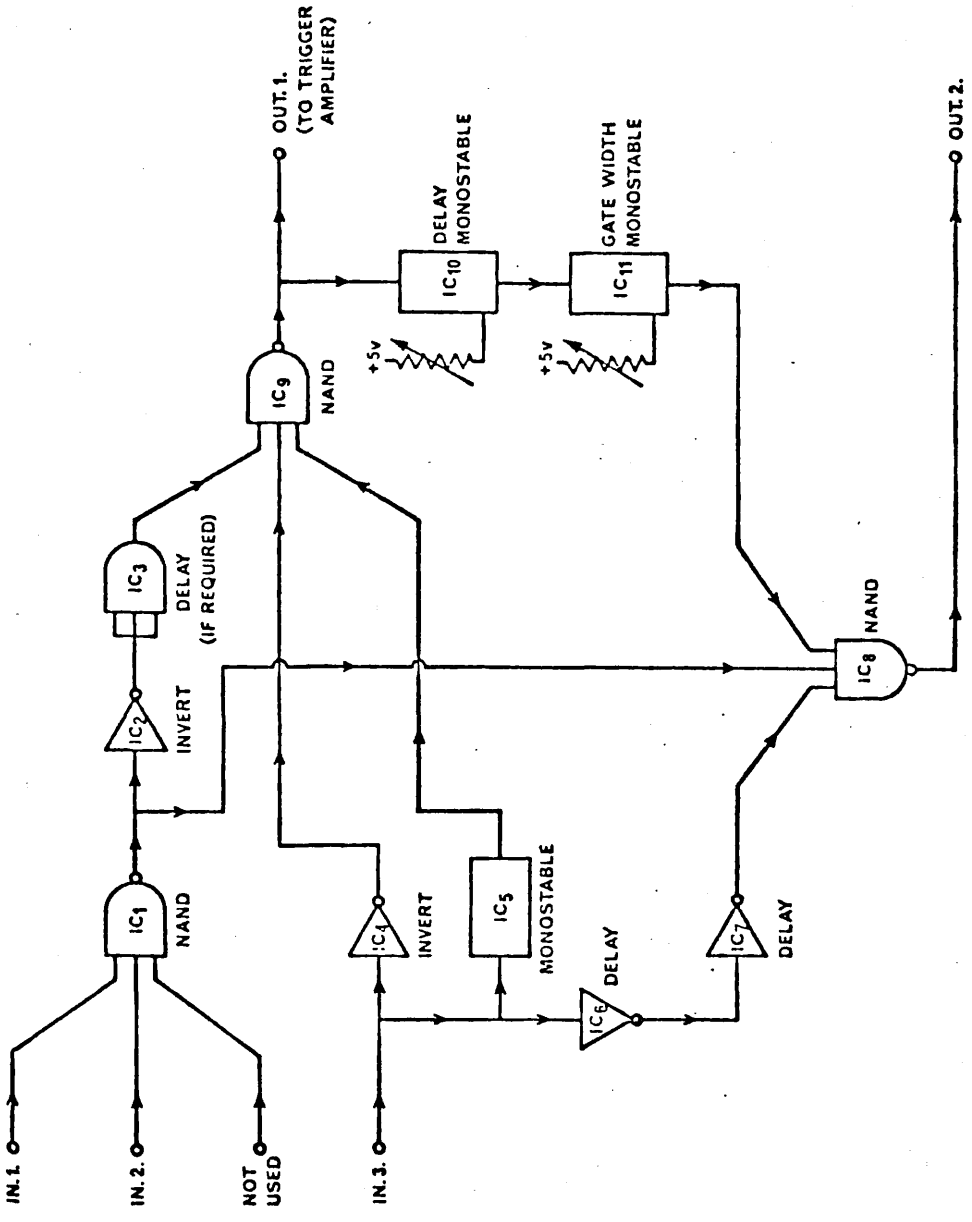

Fig. 3.6.2.1 A block diagram of the control electronics

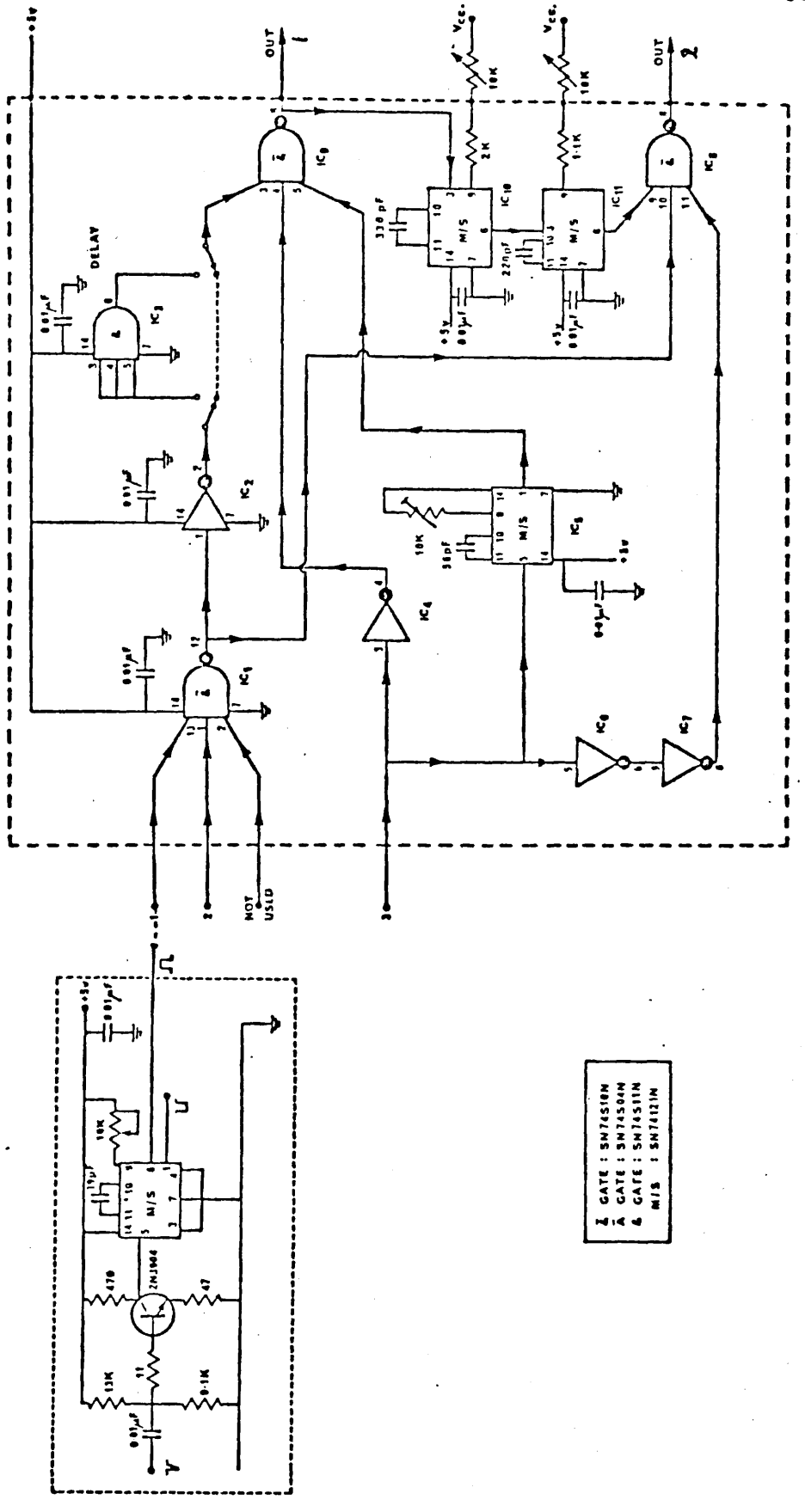

Fig. 3.6.2.2 Detailed circuits for the pulse shaping and logic

3.2 microseconds. The monostable IC_{11} determines the time for which IC_8 remains open; this time could be adjusted between 0.5 and 2 microseconds. The output from the anticoincidence counter applied to input 3 was inverted (IC_6) and delayed (IC_7) and then applied to the input of NAND IC_8. Thus for two simultaneous inputs at 1 and 2 and no input at 2, the NAND IC_9 gives an output; and if after a certain delay another pulse arrives at input 3, an output pulse from NAND IC_8 is obtained at OUT 2. However if pulses arrive at inputs 1 and 2 which are simultaneous with this delayed pulse at input 3, no output will be obtained because the output IC_1 will directly inhibit IC_8. All NAND gates were Schottky SN74510N which have a transit time of about 3 nanoseconds, the monostables were SN74121N and the inverters were SN74511N.

3.6.3 High speed trigger amplifier unit

The circuit used Fig. 3.6.3.1 consists of four stages. The first is a buffer to protect the logic unit from the high voltage part. A fast p.n.p. transistor 2N3906 was used; in normal condition the transistor is conducting, a negative logic output pulse applied to the base of the transistor gives a negative output which has the same amplitude as the input pulse. A pulse transformer (L2) was used to invert the output of the buffer, the ratio of the transformer is 1:1. The positive pulse from the transformer will switch on the high speed avalanche transistor Tr 2 (RT 3333A) of the second stage giving a fast rising negative pulse of 50 volt amplitude. Another pulse transformer of 1:5 ratio was used to invert this pulse. The third stage was used as a pulse shaper because the inverter output was too short to turn on the valve V2 (EL 360)

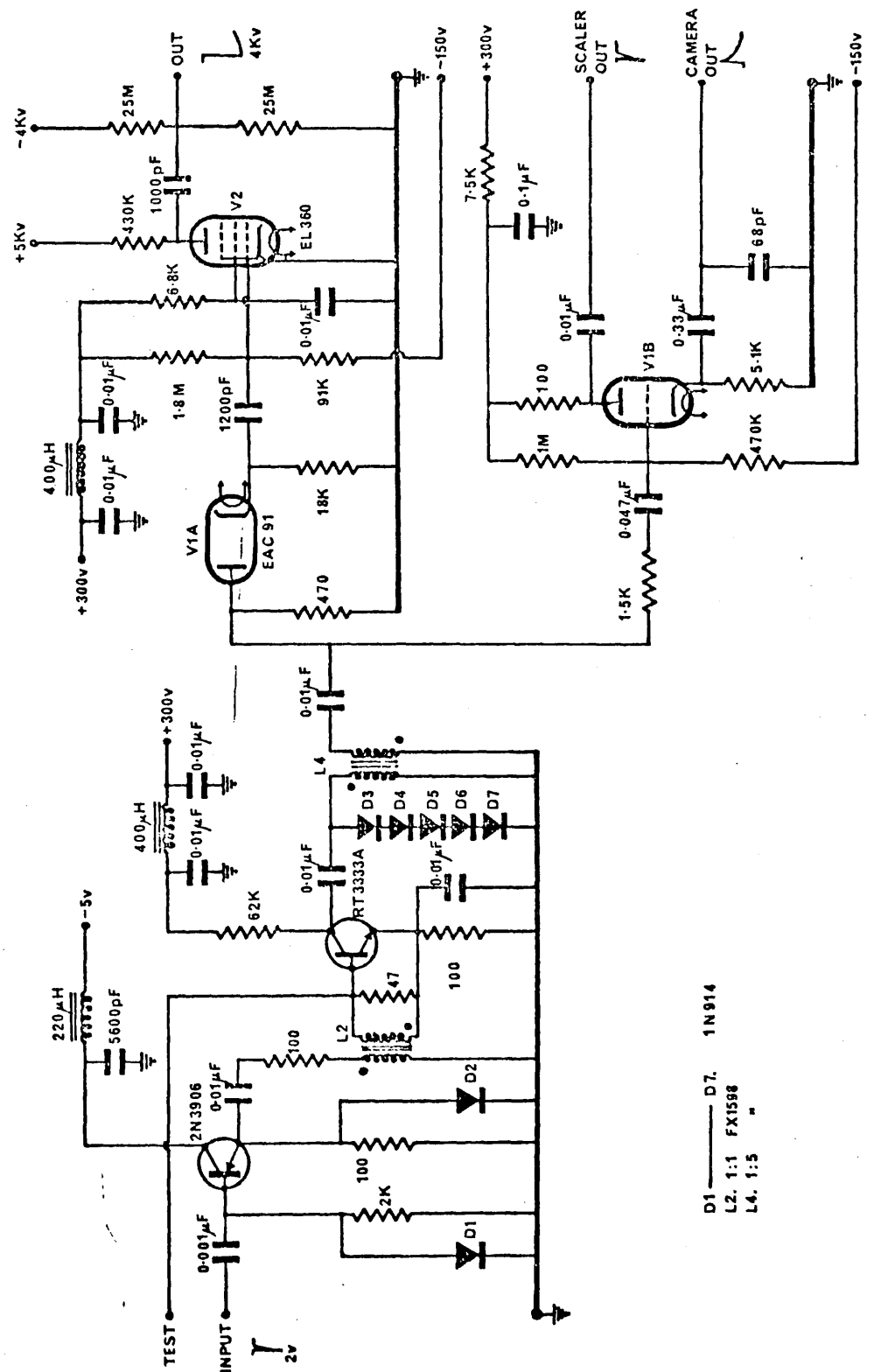

Fig. 3.6.2.2 The fast trigger amplifier

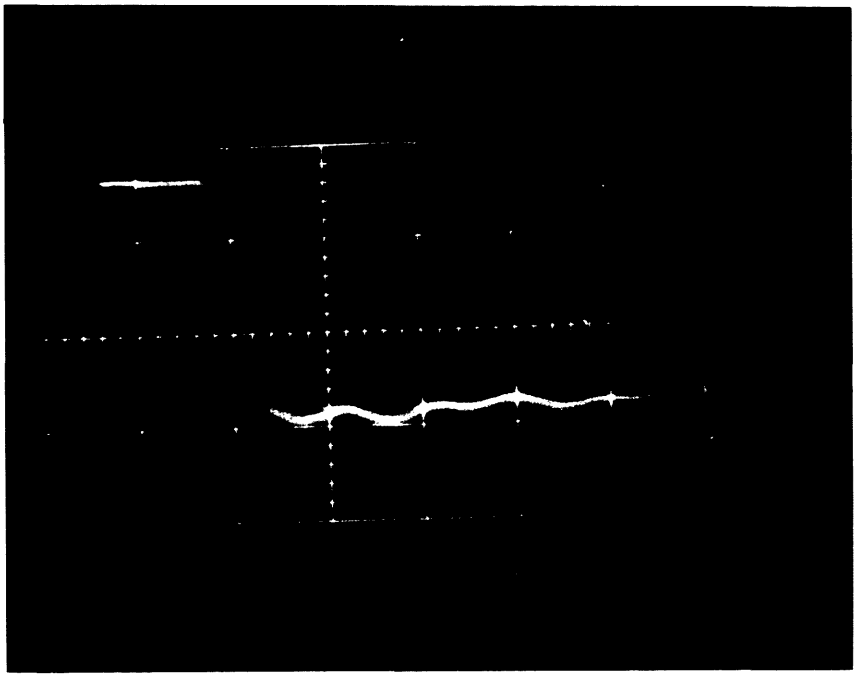

Fig. 3.6.3.2. The output pulse of the trigger amplifier

of the fourth stage. A diode-triode EAC 91 was used, the diode part as a pulse shaper to lengthen the pulse and the triode part as an amplifier/buffer to drive the automatic camera and provide a suitable pulse for the scaler.

The fourth stage consists of an EL 360 valve. This valve is normally cut off, but a positive 180 volt from the output of the diode pulse shaper applied to the control grid will switch it on giving a fast negative pulse of about 4 kV and a rise time of 10 nsec. (Fig. 3.6.3.2). This pulse was used to trigger the intermediate spark gap. Since the pulse needed to trigger the intermediate spark gap was 5 kV, a 2 kV negative D.C. bias was applied continuously on the spark gap. This was found to improve the delay in switching the spark gap. The total delay over the trigger amplifier was found to be about 25 n.sec. and the overall delay of the whole logic unit, from limiter to the trigger amplifier was measured to be less than 75 nanoseconds.

3.7 Recording of tracks

An automatic 35 mm. camera has been used to record the tracks. It has a 50 mm. focal length and a stop number from 1.8 to 22. The clear perspex of the chamber walls transmits about 90% of the visible light. Before photography begun the chambers were surrounded by a black cloth to cut down the background light from the spark gaps, the indicator lamps of the instruments were removed or covered by P.V.C. black tape. The camera was focused at the middle of the chamber from a distance of about 4 feet, so the depth of field would cover the whole chamber. The camera has no shutter so photography had to be done in complete darkness. When an event had been selected

and the Marx had fired, a pulse from the trigger amplifier would advance the film to the next frame and the camera would be ready to record the next event. The film used was Ilford HP 4 which has a speed of 650 ASA when developed in Ilford Microphen for $5\frac{1}{2}$ minutes at $20^{\circ}C$. giving a contrast gradient of 0.55. The speed of the film could be further increased by increasing the developing time, for a developing time 15 minutes at $20^{\circ}C$. the speed of the film becomes 1250 ASA with a contrast gradient of 0.9.

In the continuous streamer mode a speed of 650 ASA was found to be sufficient but for separate streamers (projection and side view) a photography speed of 1250 ASA was necessary. For high resolution, the speed of the emulsion should be rather low so by increasing the speed one affects the resolution. However, HP 4 film has an excellent speed/grain ratio. The resolution can also be affected by halation (i.e. reflection effects of the back surface of the film) but in our case the intensity was low enough for these effects to be minimal. The HP 4 film, when purchased in 200 foot rolls, is called Mark 5.

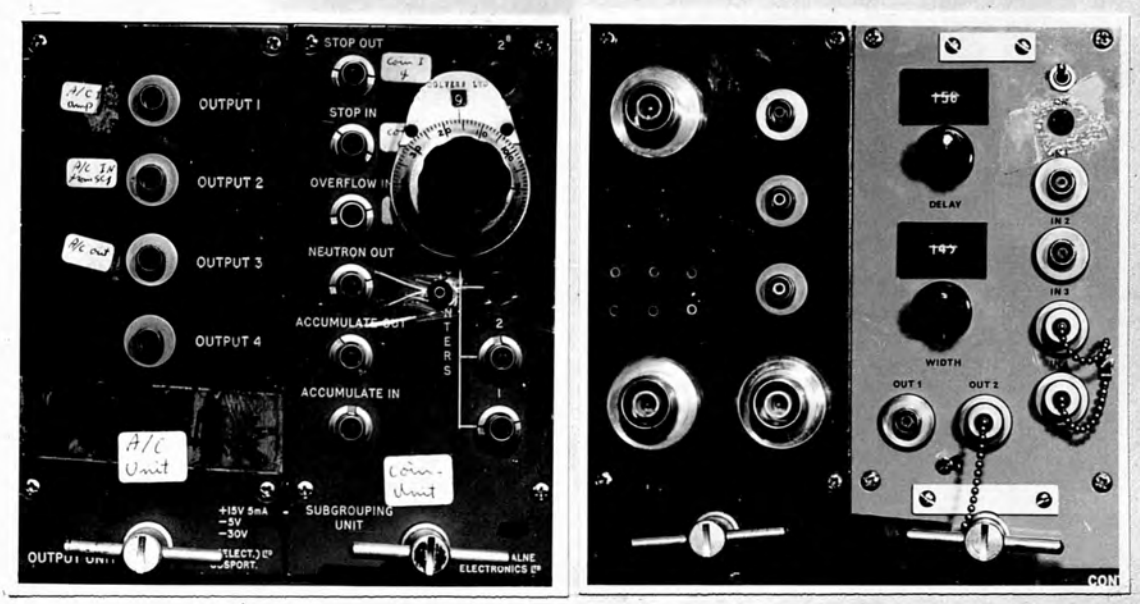

a b

Fig. 3.7.1. Photographs of the units constructed in the course of this work
(a) valve control unit (b) solid state logic and high speed amplifier

Fig. 3.7.2 Photograph of the streamer chamber

Fig. 3.7.3 Photograph of the control electronics

CHAPTER 4

Performance of the System

4.1 Introduction to Pulse Shaping

The streamer chamber differs from the conventional spark chamber by the fact that the electrodes are isolated from the sensitive gas volume. The electrodes do not completely discharge through the gas but rather the field on the chamber is cancelled before the streamers develop into a spark. An early approach was to apply the output from the high voltage Marx generator directly to the plates of the chamber and then to use shunting resistors, so the pulse will decay exponentially with a chosen time constant. In practice this method has been abandoned, partly because the exponential pulse shape is not ideal for streamer development.

Since the internal impedance of most high voltage generators tends to be larger than is satisfactory when fast rise times and short pulse durations are required, an intermediate pulse shaping net-work is necessary to free the generators from restrictions of this kind. This permits straightforward extrapolation of small generator to generators with additional stages, although special care must be taken to prevent breakdown in the charging elements since the voltage appears across them for a much longer time than it appears across the chamber electrodes.

Such a pulse shaping method is the use of a series-parallel spark gas arrangement developed by Chikovani et al. (1965) which has proved a considerable improvement. The Marx output charges a low inductance capacitor which when a certain high voltage is reached fires the series spark gap giving rise to a fast rising pulse, the

duration of which is controlled by the parallel spark gap. This pulse appears on the chamber.

Another method, which is considered best for pulsing large chambers (2 m) (Bulos et al. 1967) is the Blumlein line. It is essentially a transmission line arrangement consisting of a charged element that when fired delivers a square pulse to the chamber which forms part of the transmission line.

4.2 Series and shunt spark gaps

The rise time of the output pulse from the Marx generator was improved with the spark gap arrangements shown in Fig. 4.2.1. The Marx output first charges the shaping low inductance capacitor C; when the breakdown voltage is approached, the series spark gap S, fires with the result that the pulse actually transferred to the chamber has an improved rise time. This improvement is obtained at the cost of an increase in delay by a few nanoseconds which is immaterial in our case.

The shaping capacitor C was made out of large arrangement of perspex plates with aluminium electrodes (121 x 45 cm^2); its capacitance was 56 pF. The series spark gap was made of two hard steel spherical balls, 2.5 cm. in diameter, the gap width could be adjusted. The shunt or parallel spark gap is made up of two stainless steel hemispheres 2.5 cm in diameter, they are enclosed in a perspex box. The earthed electrode has been attached to a threaded brass rod, by means of which the gap width can be adjusted. The moment of breakdown of the series spark gap is controlled by adjusting the gap width.

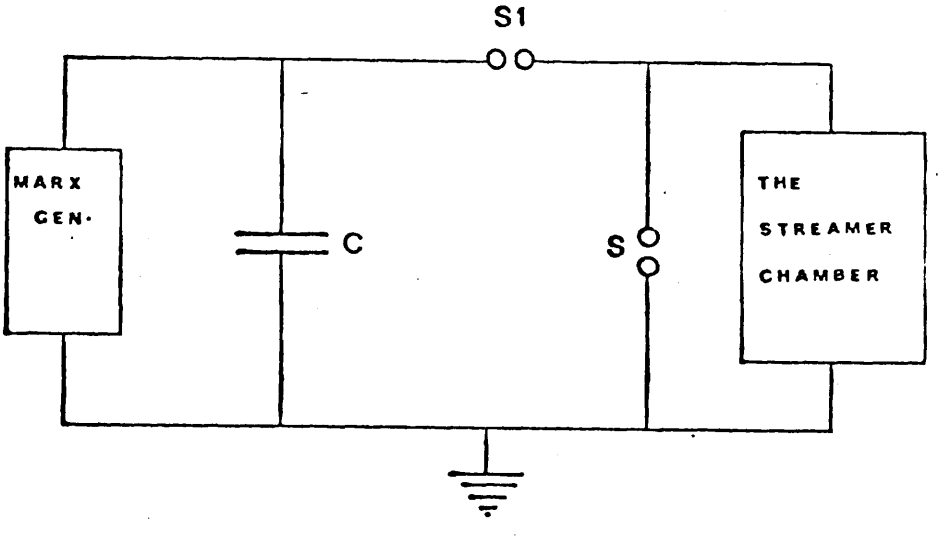

Fig. 4.2.1 The spark gap pulse-shaping arrangement

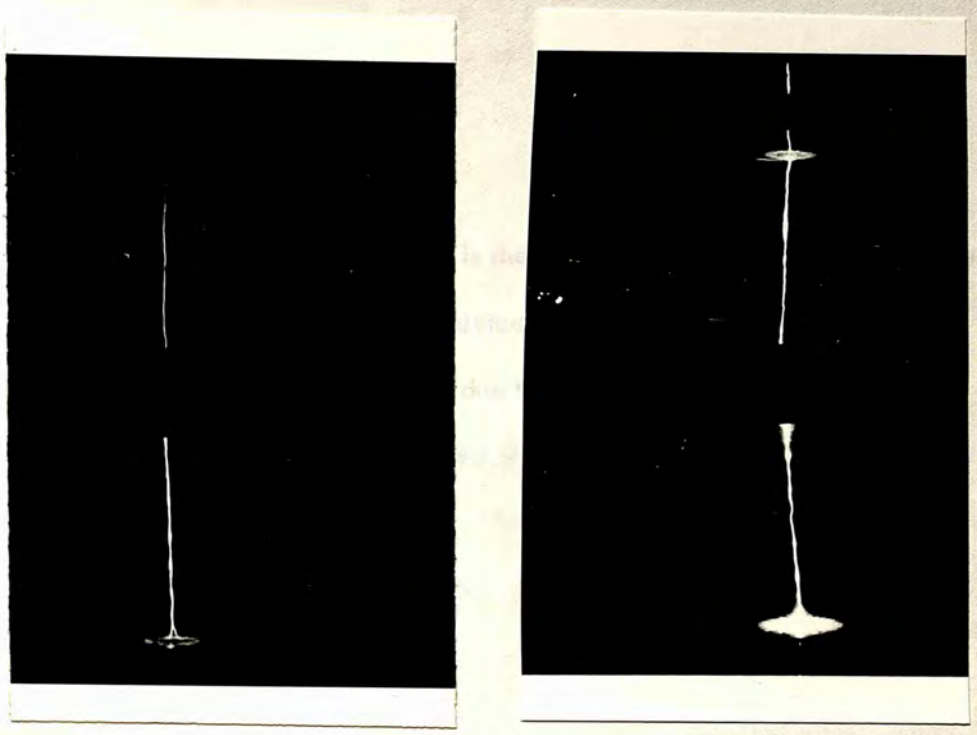

Fig. 4.2.2 Photographs of cosmic ray tracks obtained with the spark gap pulse shaping arrangement showing the fluctuation in brightness

The length of the high voltage pulse and hence the duration of the field on the chamber was adjusted by changing the width of the parallel spark gap. Both the spark gaps were operated in air at atmospheric pressure during this work. With this arrangement a pulse with 5 - 6 n. sec. rise time could be achieved (Mishra 1969).

A disadvantage of this arrangement is that the final pulses are likely to have different widths as a result of the fluctuating uncertainty in breakdown time of the over-voltaged shunt gap and due to slight changes in atmospheric conditions. Photographs of the tracks obtained by this arrangement can vary in brightness due to this fluctuation. Samples of these photographs which are taken with the same spark gaps setting are shown in Fig. 4.2.2.

Attempts to eliminate the variation in the time taken for the shunt gap to fire have included priming the gap with a constant supply of electrons from an adjacent corona needle or ultra violet source (Gygi and Schneider, 1964). And actual triggering of the shunt gap is also feasible. Spark gap operation in pressurised nitrogen can circumvent variations in atmospheric conditions.

4.3 Lecher Wires

From the beginning a series/parallel spark gap arrangement had been used to shape the high voltage. To eliminate fluctuations in streamer brightness, it was decided to try alternative means for pulse shaping. In the first trial the chamber electrodes were joined to a long aluminium foils to form part of a transmission line, short circuited at the far end. The intention was that the

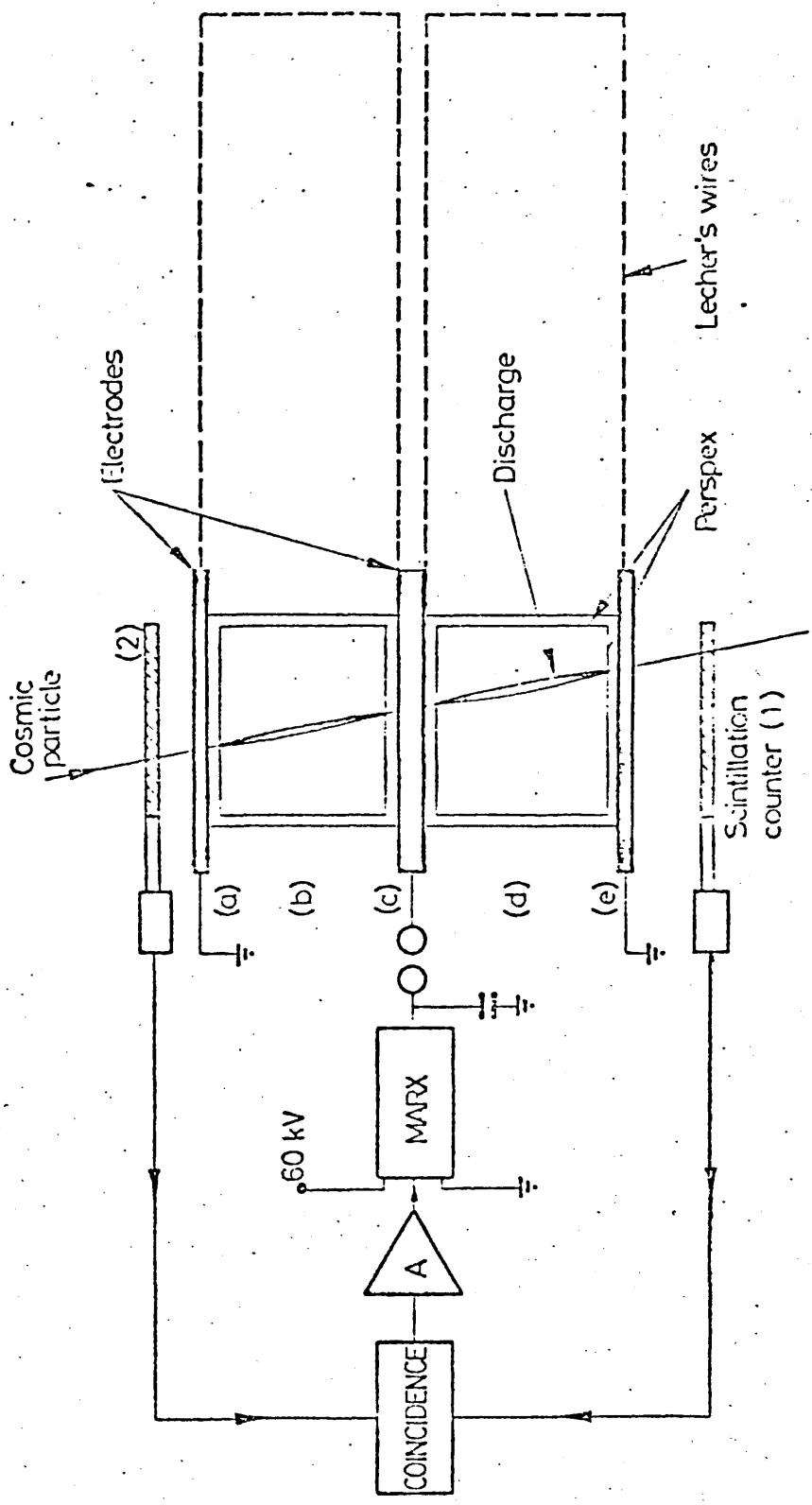

Fig. 4.3.1 High voltage pulse shaping arrangement using Lecher wires

inverted pulse reflected from the end would cancel the field in the chamber after a time controlled by the length of the transmission line; this attempt did not work because the capacity of the pulsing system (Marx generator) was inadequate to charge the line.

When the parallel plates were replaced with parallel wires shorted at the far end, visible streamers were observed inside the chamber and photographs of tracks obtained. Figure 4.3.1 shows the wire arrangement. The wires used were 2 mm. diameter stranded copper wire· the track brightness could be varied by changing the length of the wire line. For these wires the appropriate length of line was found to be about 2.7 m. for the best tracks. Figure 4.3.2 shows some results obtained by this pulse shaping arrangement, (a) shows a typical 20 cm. track taken in the projection streamer mode and (b) 2 x 20 cm tracks in the continuous streamer (side view) mode. In the projection mode the appearance of an individual track is hardly distinguished from the case with the parallel spark gap shaping. In the continuous mode the appearance of the track is quite different. Instead of the fine, slightly rippled track the track is diffuse, more regular and broader in the middle. This was thought to be caused by oscillation in the electric field caused by the reflected pulse as a result of the system not being matched. Using this arrangement it was possible to obtain tracks of constant brightness. The constancy of track appearance obtained with lecher wires has led us to adopt it during this work.

For a transmission line, assume that an arbitrary impedance Z is connected across the far end of the line, then

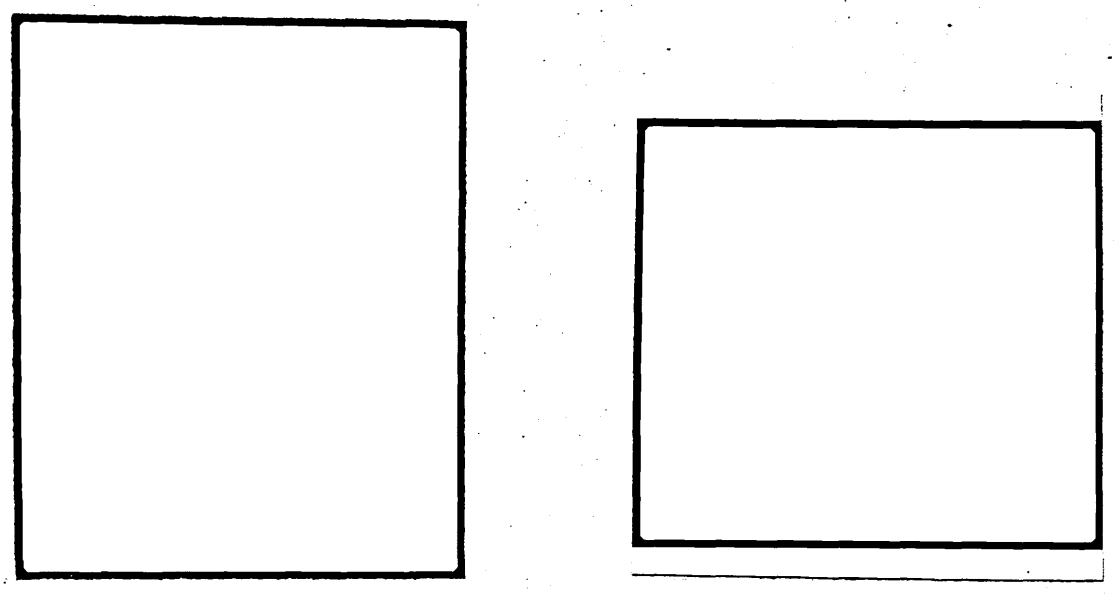

a b

Fig. 4.3.2 Photographs of cosmic ray tracks obtained with Lecher wire arrangement

$$\rho = \frac{Z - Z_o}{Z + Z_o}$$

where Z_o is the input impedance. (In our case the far end of the line was shorted i.e. $Z = O$, and then $\rho = -1$.) Therefore the reflected wave is of the same amplitude as the input but opposite in sign. The characteristic impedance of a parallel wire transmission line is given by:

$$Z_e = 276 \log d/a \text{ ohms} \qquad (4.3.2)$$

where $a << d$ (Lewis and Wells 1956). Where a is the wire radius and d is the distance between the wires. The conductors are supposed to be lossless and if embedded in a medium of relative permeability K_m and relative permittivity K_e the expression for Z_e (which is given in ohms) must be multiplied by K_m/Ke. For a rectilinear line the inductance and the capacitance are given by:

$$L = \frac{K_m}{300} Z_e \quad \mu H/m \qquad (4.3.3)$$

$$C = \frac{K_e}{3Z_e} \times 10^4 \quad PF/m \qquad (4.3.4)$$

The transmission line used is referred to as a rectilinear uniform line because it consists of two parallel conductors of constant cross section along the line.

The velocity of propagation is independent of frequency, in particular, there does not exist any low frequency cut off as in a wave guide. The speed of propagation is equal to that of a plane wave in an infinite volume of the dielectric (air) which fills the space between the conductors. If T is the time delay per unit length then:

$$T = \sqrt{\epsilon\mu} = \frac{10}{3}\sqrt{Ke\ Km} \quad \text{n.sec./m} \qquad (4.3.5)$$

from equations 4.3.3 and 4.3.4

$$T = \sqrt{LC} \quad \text{sec/m} \qquad (4.3.6)$$

In the case concerned it was found that the speed of propagation T = 3.3 n sec/m. and the impedance $Z_{wire} = Z_e = 635$ ohms.

Since the chamber electrodes form a part of the transmission line so its characteristics impedance is given by:

$$Z = 377\ \frac{x}{b} \quad \text{ohms} \qquad (4.3.7)$$

$x << b$, which is the expression for the impedance of a transmission line made out of parallel strips, x is the distance between the two conductors and b is the width of the conductor. The impedance of the chamber electrodes was found to be:

$$Z_{ch} = 128 \text{ ohms}$$

and the speed of propagation is the same as in the case of the parallel wires.

It is clear that the chamber and the Lecher wires are not properly matched, nevertheless the quality of the tracks was considered very satisfactory.

At one stage in our experimentation shunting resistors were used instead of the parallel spark gap to control the duration of the high voltage pulse on the chamber, but they were found unsatisfactory. For a resistance of 165 ohms the whole chamber was illuminated; reducing the resistance to 110 ohms the chamber was found to work with rather low efficiency and the tracks still very bright. Any reduction in this resistance reduced the efficiency still further, but any increase made the tracks too bright and the entire volume of the chamber glow. The reason seems to be that the high voltage pulse starts decaying exponentially as soon as it is applied. The exponential pulse shape is not ideal for streamer formation, and the uncertainty in the moment of streamer formation is too large when compared with the full time of the pulse.

The multiple track efficiency was also found to be poor. These troubles were completely absent in the case of a shunt gap or lecher wires, because in these cases the amplitude of the high voltage pulse remains roughly constant on the chamber until it is cancelled by the gap break down or the reflected pulse in case of wires.

4.4 High voltage pulse monitoring

Resistive and capacitive probes were used in attempts to monitor the high voltage pulse. With the series/parallel spark gap arrangement a resistance chain was used. The output pulse was fed to Tektronix 581A oscilloscope after attenuation, first by a resistance dividing (1:10) chain and then by a 1:1000 HV probe (P6015). Noise and both mains borne and radiated interference prevented the pulse being seen; instead a ringing noise was observed every time the Marx fired. A separate screened mains line was obtained for the oscilloscope from another building to eliminate the mains borne interference. A filter was also used. Although this led to some improvement, it was found that radiated interference still prevents the clear observation of the high voltage pulse.

When Lecher wires were used as a pulse shaping network i.e. the chamber was a part of a transmission line a capacitive divider (Fig. 4.4.1) was used. Such a probe could be mounted just inside the ground plate of the transmission line in this case the earthed chamber electrode. This probe is made of thin aluminium foil mounted between two perspex rings, the output lead is taken through a hole in the earthed electrode. The capacitive division is equal to distance between the earth electrode and the aluminium foil divided by the distance between the chamber electrodes which is:

$$2 \text{ mm}/20 \text{ cm} = 1/100$$

i.e. the pulse is attenuated by 1:100 by this probe, which was followed by an

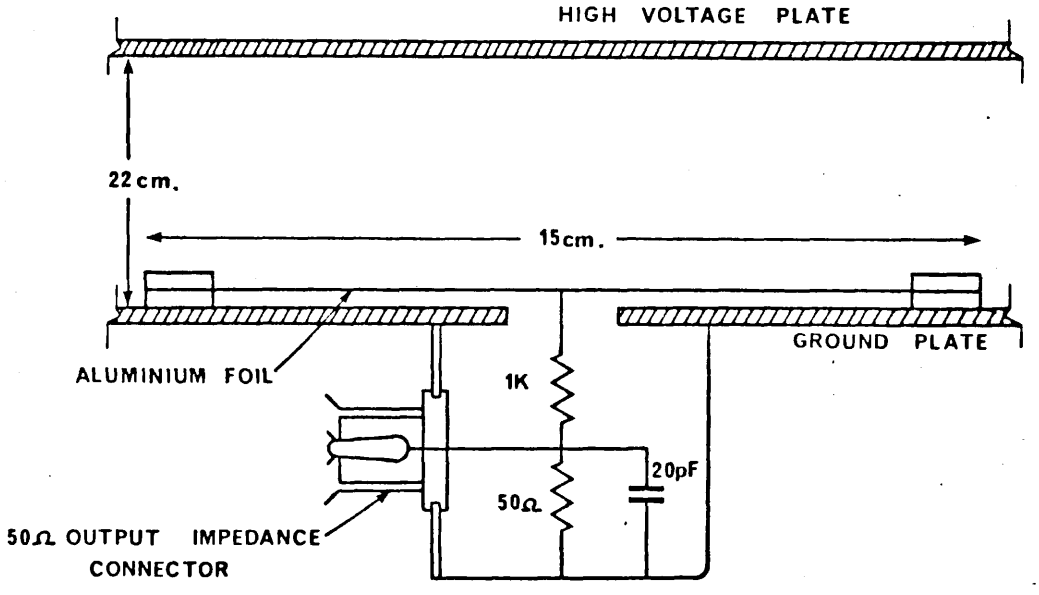

Fig. 4.4.1 A capacitive probe

additional resistive divider of 25 ohms/1000 ohms = 1/40. Thus the total attenuation is 1/4000. A 1000 ohm resistor is connected in series with the output so that the pulse is not severely differentiated by the probe capacitor across the 50 ohms cable terminated by a 50 ohm resistors at both ends.

Capacitive probes tends to ring. An important source of the ringing of a capacitive probe mounted on a transmission line is the difference in wave velocity in the dielectric of the probe and that of the transmission line. There are two ways of solving this problem; either by using the same dielectric in both the probe and the transmission line (Bulos et al. 1967) or by making the thickness of the metalic conductor of the probe less than the skin depth as suggested by (Gygi and Schneider 1964). In this work the first method was adopted and the same dielectric (air) was used in both the probe and the transmission line. Using this pulse attenuation arrangement with Tektronix 581A oscilloscope, radiated interference and other sources of interference prevented the pulse from being observed. (Bulos et al. 1967) noted that with attenuation as high as this, care must be taken so that pick up in the cable does not mask the attenuated pulse; additional radio frequency shielding of the signal is necessary to obtain a clean pulse. As a result of these attempts, it was concluded that to obtain a clean visible pulse, the entire experimental arrangement (Marx generator, the shaping condenser and the chamber) has to be completely shielded, otherwise any attempt to observe the high voltage pulse will be prevented by radiated interference.

4.5 Accuracy of Track Measurements

The spatial accuracy of tracks observed in this streamer chamber was reported to be 0.34 mm. (Rice-Evans and Mishra 1969). The spatial accuracy of a track is the root mean square deviation of the measured points about the reconstructed trajectory. The method used consists of measuring the co-ordinates of a number of points on the track, constructing a line by least square fit and then determining the standard deviation of the measured points in a direction normal to the constructed trajectory.

The precision in angular measurements which was necessary for the present experiments was estimated as the average of the standard deviation of a number of measurements of the angle between the tracks in both gaps computed by the method of least squares.

Ten arbitrary events having tracks in both gaps were chosen. The co-ordinates of ten points on each track were measured and each event was scanned ten times. So for each event ten values of the same angle θ were obtained.

For a particular event the standard deviation of these ten values of θ is given by:

$$\sigma\theta = \left[\sum_i (\theta_i - \bar{\theta})/_{n-1} \right]^{\frac{1}{2}} \qquad (4.5.1)$$

where $n = 10$ is the number of repeated measurements, and $\bar{\theta}$ is the mean value of the measured angle.

The scanning was made with the digitized D-Mac table belonging to Dr. P.T. Trent at Birkbeck College, University of London. The co-ordinates of each point are punched on eight hole paper tape by the teleprinter attached to the table. The measurements of the angles were computed by CDC 6600 University of London computer.

The mean of the mean standard deviation of our angular measurements was found to be 1.5 m.rad.

4.6 The Effect of Gas Pressure On Track Qualities

In the case of continuous streamer mode it was found that the efficiency of the chamber as a track detector was reduced appreciably with the reduction of gas pressure. However at 200 m.m. Hg. the efficiency was very low and the whole chamber was found to glow, reducing the pulse duration by adjusting the length of lecher wires, the background glow was decreased but there was no improvement in the efficiency. The glow is probably connected with the reduction of the break-down voltage with pressure and due to the increased photon radiation at lower pressures. A vast decrease in the number of primary electrons, and in the gas multiplication, because there are fewer gas atoms at lower pressure, might be the reason for the decrease in efficiency. It was noticed also that at low pressures the tracks become wider and diffused, which could be due to electron diffusion at low pressure, since diffusion is inversely proportional to the square root of the pressure. Operation at high pressures offer the prospects of high spatial resolution, because the tracks become narrower and less diffused, but at higher pressures the working voltage has to be increased.

In a set of experimental results (Fig. 4.6.1) to show the effect of gas pressure on track qualities, the high voltage pulse applied to the chambers was kept constant. The Marx generator was allowed to trigger once a minute, so time was allowed for it to charge to the same level; the rise time of the high voltage pulse was kept constant by keeping the width of the series spark gap constant; the length of the lecher's wires and hence the high voltage pulse duration was the same and the lens aperture was fixed. The only variable throughout the experiment was the pressure. From the results it was clear that by decreasing the pressure the brightness of the tracks increased and the tracks became too broad.

The results shown in Fig. 4.6.1 were taken under the condition given in Table 4.6.1.

	Pressure in cm. Hg.
a	70.5
b	76
c	80.5
d	85
e	88.5
f	96
g	100

During this experiment the atmospheric pressure was 76.5 cm. of Hg.

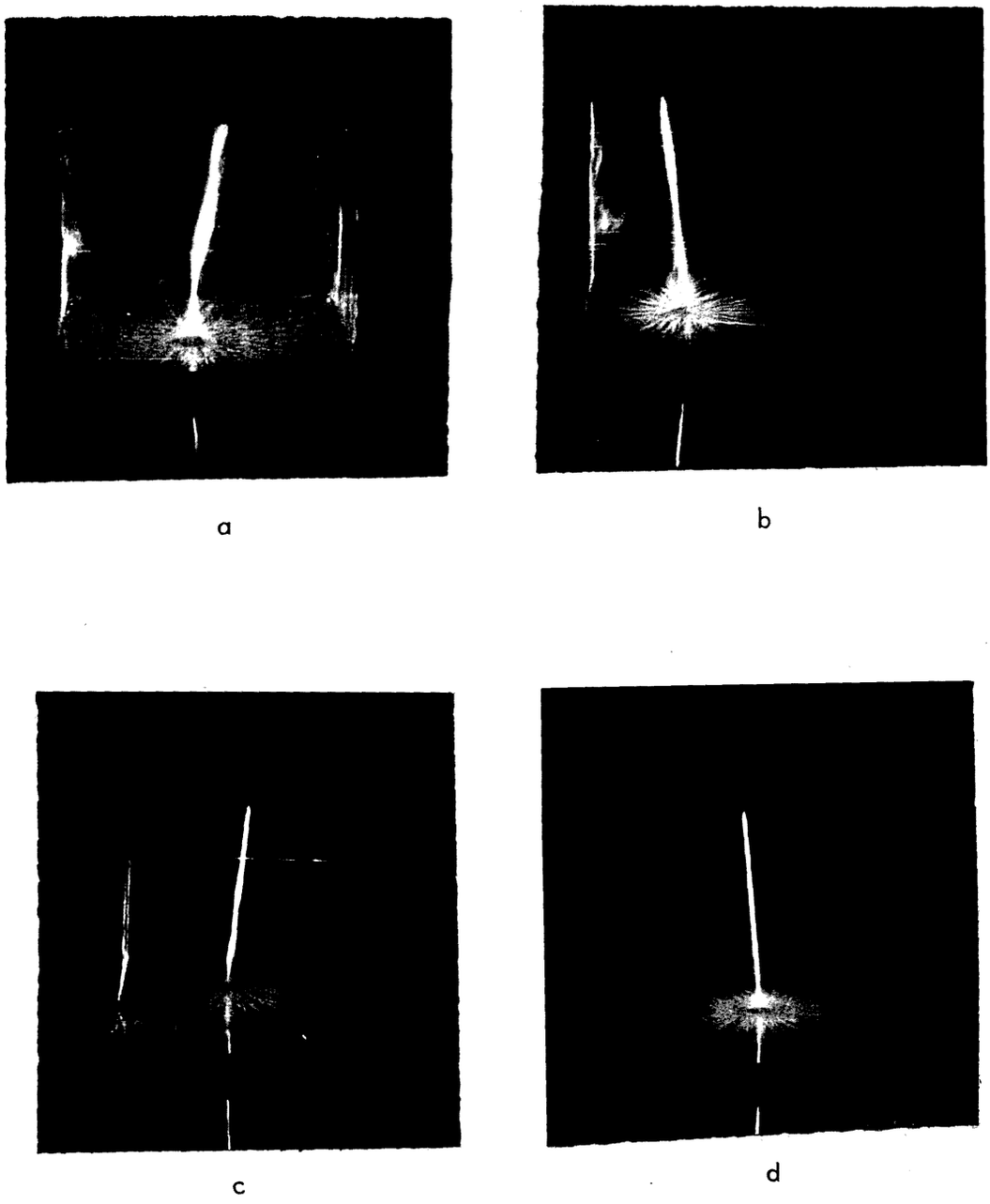

Fig. 4.6.1 Photographs of cosmic ray tracks showing the effect of gas pressure on track quality.

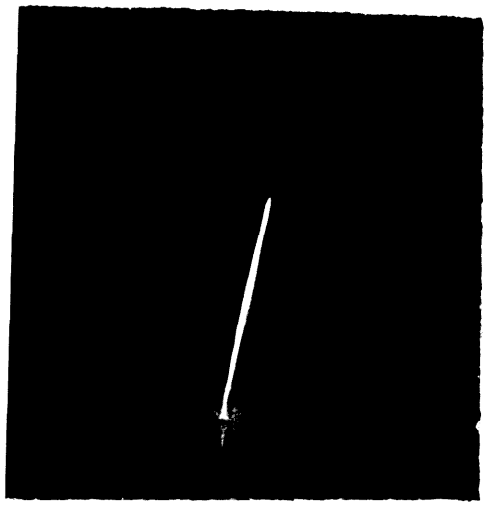

e

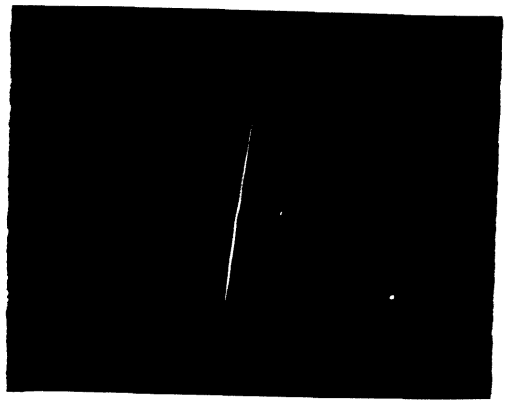

f

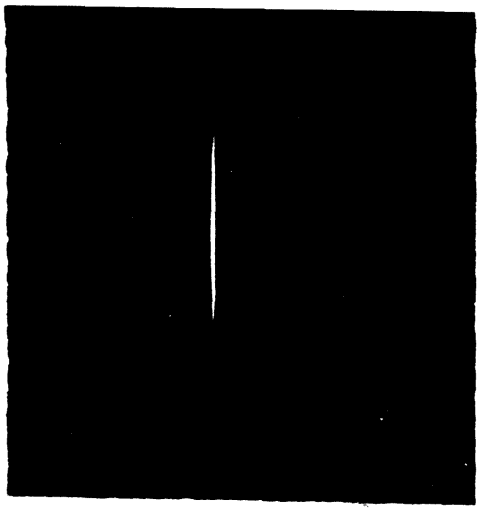

g

Fig. 4.6.1 (Continued) Photographs of cosmic ray tracks showing the effect of gas pressure on track quality

CHAPTER 5

Studies On Gas Discharges

5.1 Introduction

In 1777 G.C. Lichtenberg discovered that when an electrical discharge occurs in the proximity of a solid dielectric, star-like patterns of peculiar design may be manifested on its surface. The shape and the polarity of surface discharge could be developed by dust figures.

Since this discovery, Lichtenberg figures have attracted the interest of physicists because, their characteristics reveal some new aspects of gaseous discharges. The speed of propagation of the figures gives information on the breakdown mechanism. Their size and shape can be used for recording the magnitude and polarity of the transient voltage applied. The finely detailed drawings that Lichtenberg made of the figures offer an unusually clear record of the early stages of discharge phenomena.

An extensive study of Lichtenberg figures has been made by Merrill and Von Hippel (1939) who have observed the formation of figures on photographic plates in various gases at different pressures. The results confirm that the figures are produced by light emission from the discharge and that the nature of the figures is characteristic of the surrounding gas in contrast to the breath-figures which are generated by the resistance of the flashed surface to condensation.

It has been asserted that moving electrons are responsible for the structure of the figures. In other words that the figures are the result of electrons being

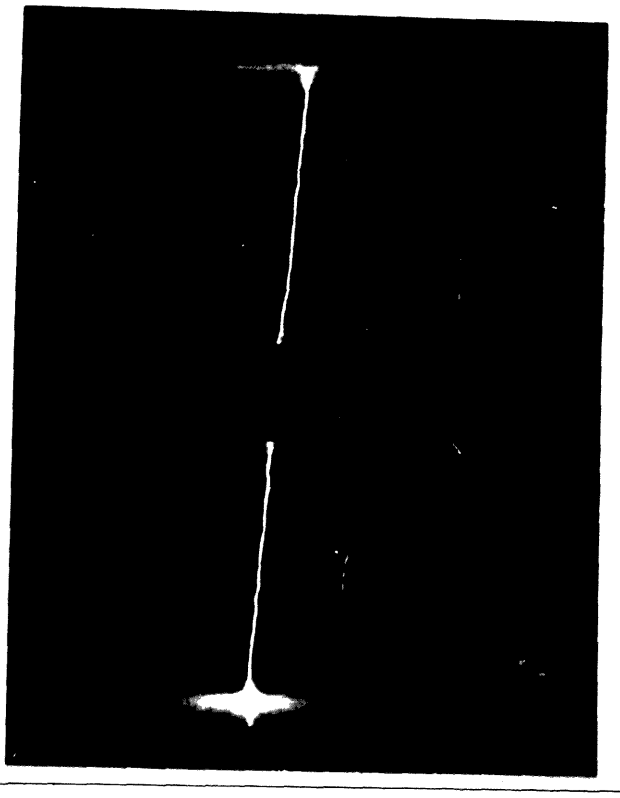

Fig. 5.2.1 Photograph of cosmic ray tracks showing the radially spoked Lichtenberg figures obtained when the shunting spark gaps arrangement was used in shaping the high voltage pulse

deposited on, or removed from, the dielectric surface, and that they indicate the paths the electrons traverse in the gas adjacent to the surface. Nasser and Loeb (1963) studied the streamer branching from Lichtenberg figures.

5.2 Observation of Lichtenberg Figures and Discoveries of Rings

Radially spoked Lichtenberg figures have frequently been photographed (Fig. 5.2.1) in the streamer chamber described by Rice-Evans and Mishra 1969. However during some attempts to improve the constancy of the high voltage pulse shaping network curious ring patterns on the surface of the dielectric were photographed.

When Lecher's wires were used to limit the pulse duration (Fig. 4.3.2) these rings pattern were observed on the chamber floor above the earthed electrode, as well as on the ceiling of the box below the high voltage electrode.

Fig. 5.2.2 shows a sample of photographs taken during the investigation of this phenomenon, the photographs show what are thought to be Lichtenberg figures associated with tracks of cosmic particles in the streamer chamber. The photograph show:

(A) A track, typical of those obtained with Lecher's wires. The Lichtenberg figures exhibits a series of light and dark rings, while the radial spoke structure is maintained in luminescent parts.

(B) An incoming cosmic particle has interacted with the central electrode and produced secondary particles. The luminous Lichtenberg rings, corresponding

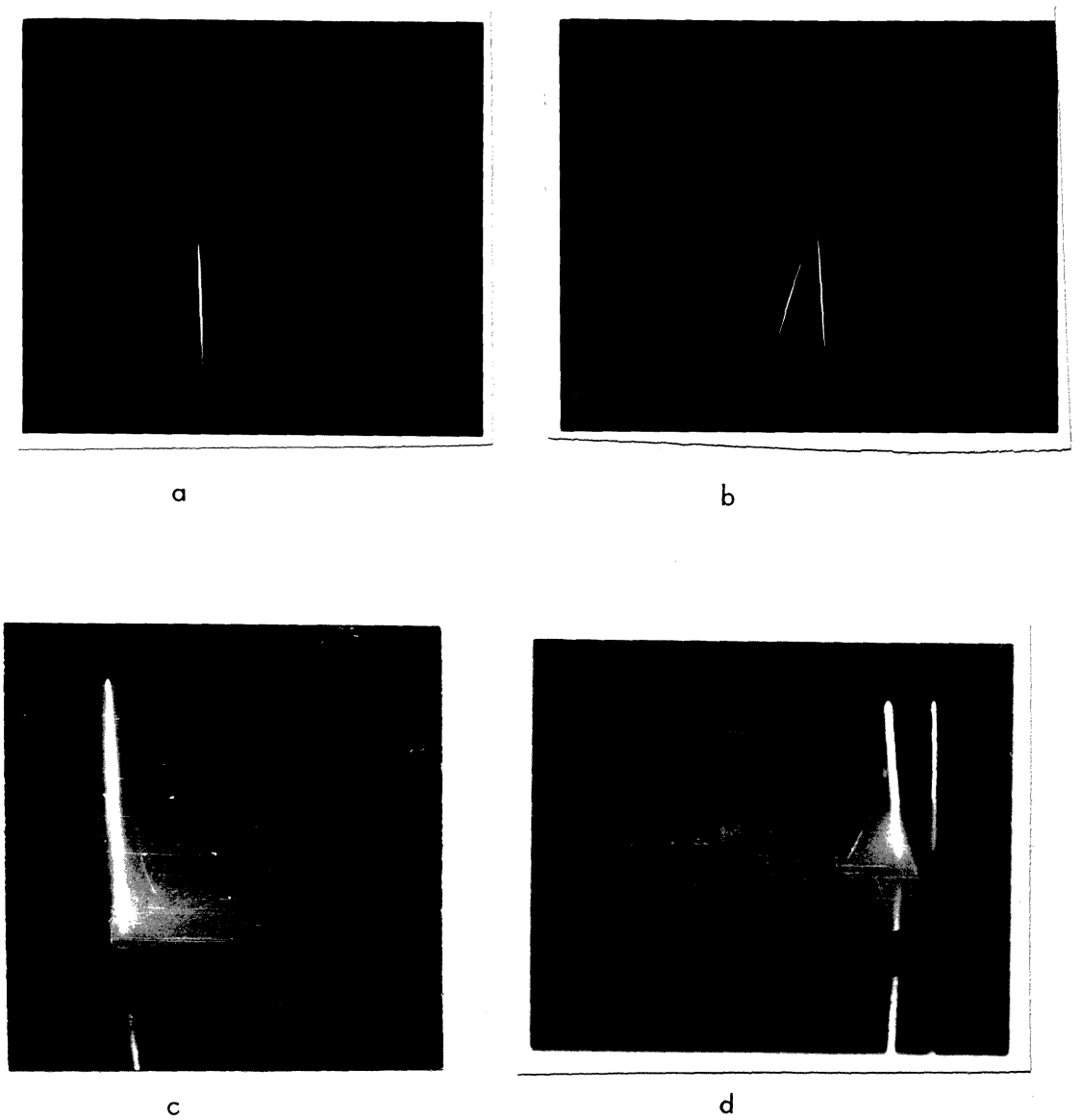

a b c d

Fig. 5.2.2 Examples of photographs taken during the investigation of the rings

to different tracks are seen to interfere with each other; they do not overlap but rather dark spaces occur.

(C) A closer view of a star-like pattern at the lower electrode.

(D) The dark ring of a Lichtenberg figure is seen to be associated with the wispy discharge in the chamber gas, from the photograph one can see that a visible cloud appears above the dark ring, as if it had been removed from the surface.

5.3 Studies on the Rings

A few attempts to observe the shape of the high voltage pulse and correlate it to the shape of the rings were not successful because the radiated and mains borne interference made it impossible to observe the pulse on the oscilloscope. To see if the light emitted from the bright rings is polarized or not, two sets of photographs of the rings were taken with a polaroid plate mounted in front of the lens, one set with the polaroid plate in one position and the other set with one of the plate rotated 90^{o}. From the results there was no apparent difference between the two cases. So it was concluded that the light emitted in the bright rings was not polarized. In another experiment to study the relation between the time for which the electric field is applied on the chamber, and the ring diameters, the amplitude of the high voltage pulse was kept constant, but the duration of the high voltage pulse was varied by changing the length of Lecher's wires.

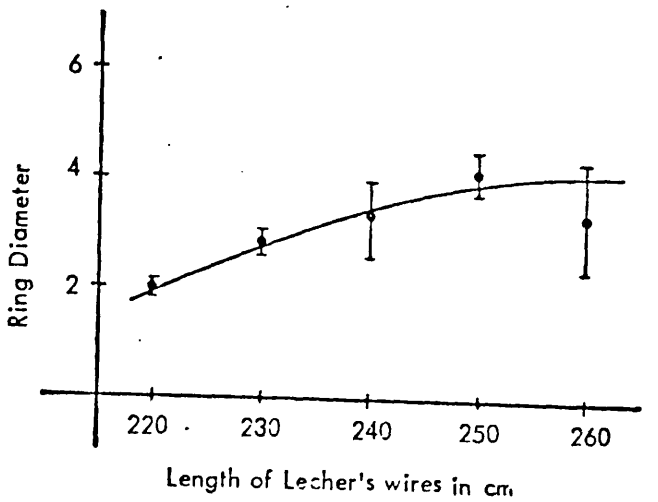

Fig. 5.3.1 The relation between the ring diameter and the length of Lecher's wires

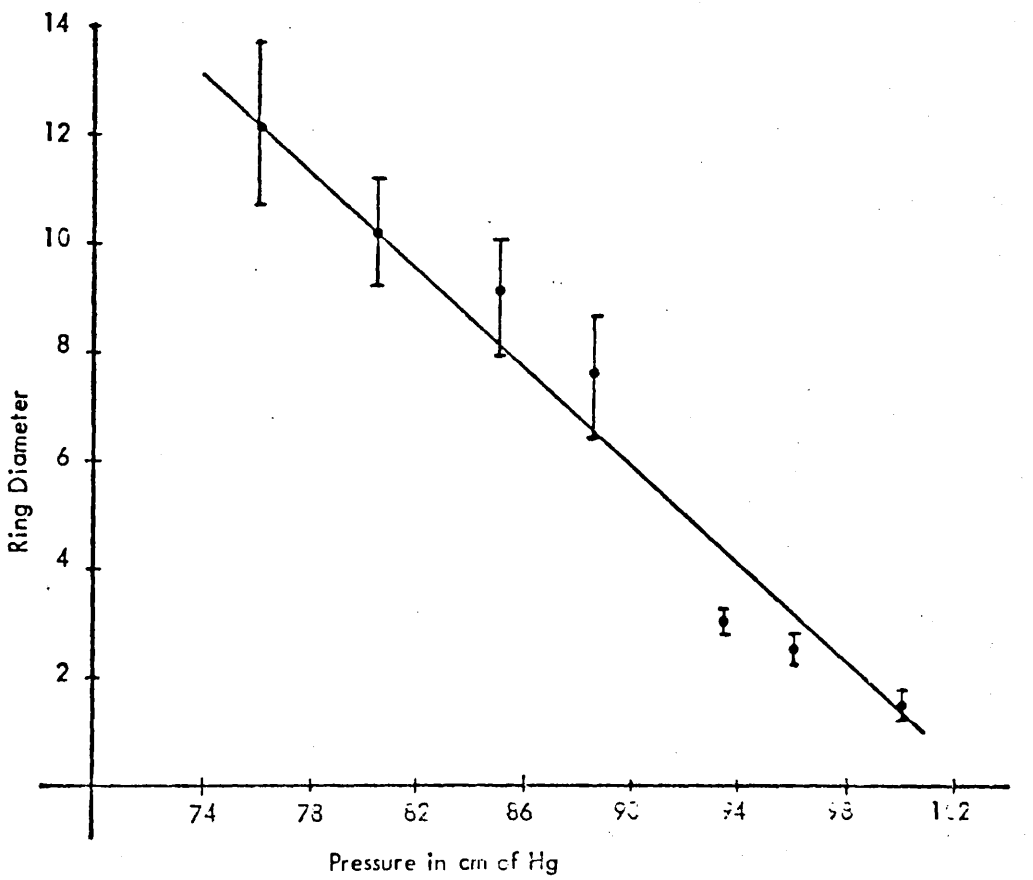

Fig. 5.3.2 The relation between the ring diameter and the gas pressure

The camera was placed at about 125 cm from the chamber looking at the bottom plate with an angle of about 30^{o}; the lens aperture was kept at 1.9.

The ring diameters were measured using the enlarger. For each length of Lecher's wires (i.e. high voltage pulse length) an average diameter was obtained and plotted against the length. The results are shown in Fig. 5.3.1, where it is clear that the diameter of the rings increases with increasing the length of Lecher's wires, when the length of Lecher's wires increased from 250 cm to 260 cm. the diameter of of the rings appear to decrease. This is most probably related to the shape of the high voltage pulse and to explain it one has to observe the shape of the high voltage pulse on the oscilloscope.

The effect of gas pressure on the diameter of the ring was observed, in this observation the amplitude of the high voltage pulse and the length of Lecher's wires were kept constant, the camera was kept in the same place looking at the bottom of the chamber.

At different gas pressures a number of photographs were taken, and the mean ring diameter was measured using the enlarger. The mean ring diameter was plotted against the pressure as shown in Fig. 5.3.2.

5.4 Discussion

The rings which are visible to the eye, show the red colour characteristic of the track discharge in the neon/helium and it is clear that gaseous ions are responsible for the luminosity. Neither the tracks, nor the rings, are seen when the chambers were filled with air.

In an attempt to explain the rings structures Rice-Evans and Hassairi (1972) suggested that the Lecher's wires arrangement causes the pulsed field which is usually about 10 kV/cm to oscillate with a period of about 5 n. sec. (depending on the length of Lecher's wires). In this event, avalanches, initiated by a total specific ionization of about 30 electrons/cm, would be expected to grow, too and fro, along the line of the track. The discharge would then constitute an oscillating plasma and would give rise to a fluctuating magnetic field with cylendrical symmetry.

The figures must indicate the form of the discharge that results from electrons moving radially over the surface of the perspex. A relevant fact is that a spark discharge on a dielectric surface is known to have a greater luminosity than a free discharge in the same gas (Daniel 1965).

The dark rings may be explained by the electrons moving from the dielectric surface, perhaps fluctuating polarisation charges or alternating magnetic fields produce successive damping and reignition of the radial charge.

CHAPTER 6

Multiple Scattering Experiment

6.1 Experimental arrangement

The following experiments were designed to study the multiple scattering of cosmic ray muons in thick scatterers. The scatterers used were lead and mercury of 1 inch thickness.

A double gap streamer chamber in the continuous streamer mode was used, with the scatterer ($9 \times 9 \times 1$ inch^3) placed between the two gaps. Fig. (6.1.1) shows the experimental arrangement, two scintillation counters (3) and (2) were placed just below and above the lead absorber - its thickness determines the momentum interval of the observed muons. The counter below the lead absorber is the anticoincidence counter (3), the other coincidence counter (1) was placed above the chamber resting on the wooden frame used for clamping the chambers. Above this counter, 15 cm of lead was placed, to absorb the soft component of cosmic ray particles and to eliminate the electrons from the analysis; electrons will produce showers if they travel through thick lead plates. The counters (2) and (1) were in coincidence, the output from the coincidence unit and the counter (3) were in anticoincidence. To satisfy the experimental conditions only the hard component of cosmic ray particles was able to pass through the thick lead absorber, the scatterer placed between the chambers and stop in the lead absorber placed between counters (3) and (2). Such an event would produce an output signal from the anticoincidence unit (logic unit in some cases). This signal after amplification triggers the Marx generator which results in

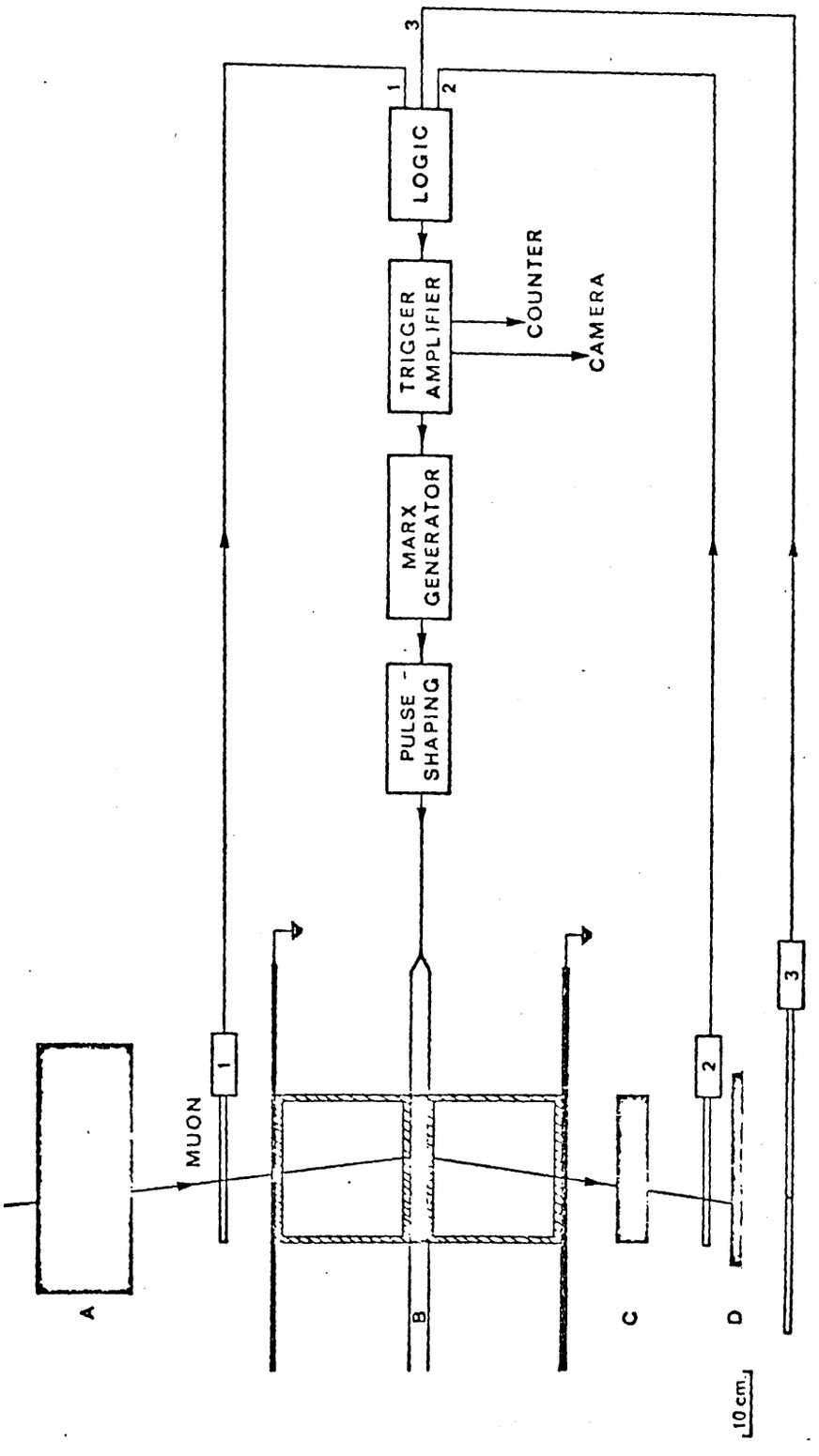

Fig. 6.1.1 The experimental arrangement for multiple scattering

the transfer of the high voltage pulse to the chambers and hence allows the visualization of an event which could be photographed and analysed.

The electronics controlling the operation of the system were described in detail in chapter 3. The experiments were carried out at sea level, the rate of genuine anticoincidence output was about 5% of the coincidence output; this being in good agreement with the established fluxes.

6.2 Efficiency of the Anticoincidence counter

An important factor in the validity of the present work is the efficiency of the detection system, especially that of the anticoincidence counter. If the efficiency of the anticoincidence counter is not high, muons of higher momenta than the expected value will be accepted. Such muons could only scatter through small angles which would badly affect the observed distribution.

Great care was taken in designing and operating the anticoincidence counter. Its size was chosen so any particle detected by the two coincidence counters must travel through it. The size of the scintillator was chosen to be 40 x 50 cm^2. A long light guide was used to improve the scintillator uniformity because it reduces the solid angle effect in the region of the photomultiplier Grieder (1967). The scintillator and the light guide were wrapped in aluminium foil to collect more light. The thickness of a scintillator is an important parameter, it effects the overall signal to noise ratio of the counter to a large extent beside the fact that thick scintillators produce more light due to longer particle tracks and hence improve the efficiency. The scintillator used for

the anticoincidence was thicker than those used as coincidence counters.

To check that the efficiency of the anticoincidence counter was uniform over the whole area, the other two counters were placed one above and one below it in five different places (the four comers and the middle) and a counting rate was taken, it was concluded that the anticoincidence counter was satisfactorily uniform over the whole area.

To check the performance of the counter and select a working voltage for it, the counters were placed in their position as shown in Fig. (6.1.1) and the counting rate out of the anticoincidence (logic) unit was observed, keeping the voltage on the coincidence counters constant and changing the voltage on the anticoincidence counter in 100 volt steps. Typical results are displayed in Fig. 6.2.1; from the graph a working voltage of 2.6 kV for the anticoincidence counter was chosen. This was repeated for the different electronic configurations.

6.3 Geometrical corrections

A geometrical factor to account for the small variation in the recording efficiency as a function of incident and scattered angles has been obtained.

The correction has been found by a graphical method. In a scaled diagram of the whole arrangement (counters, chambers, scatterer and the lead absorber) as shown in Fig. (6.3.1), five equally spaced points were taken both on the upper counter and on the scatterer. The lines joining these

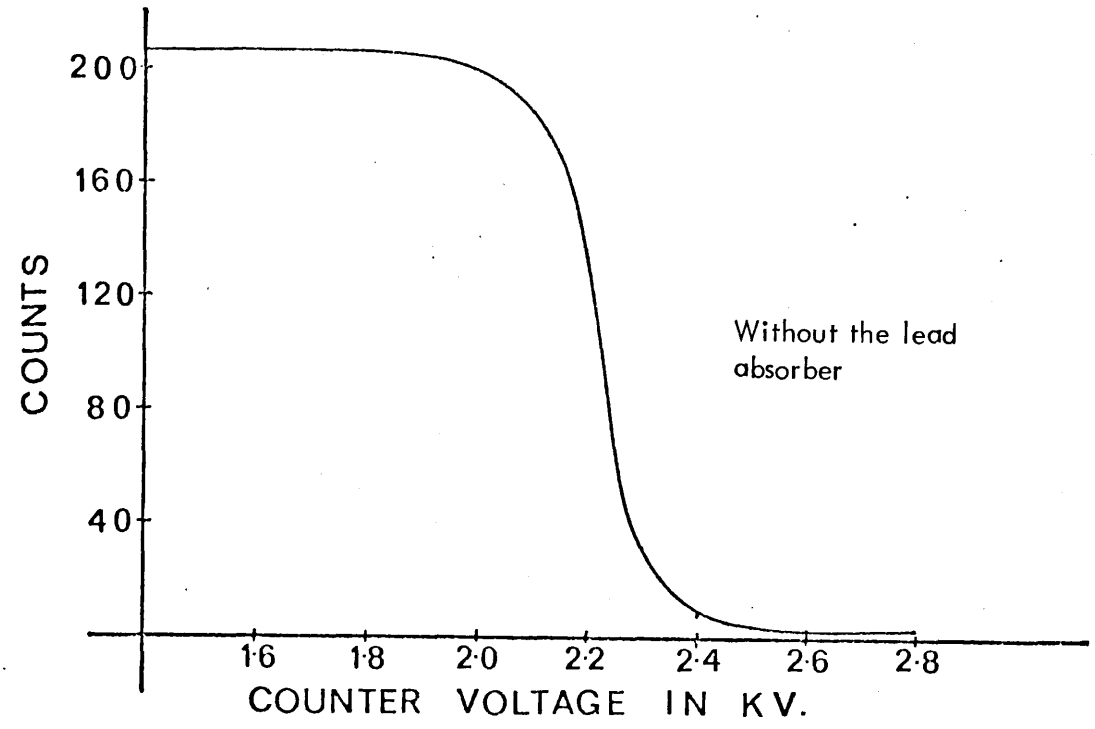

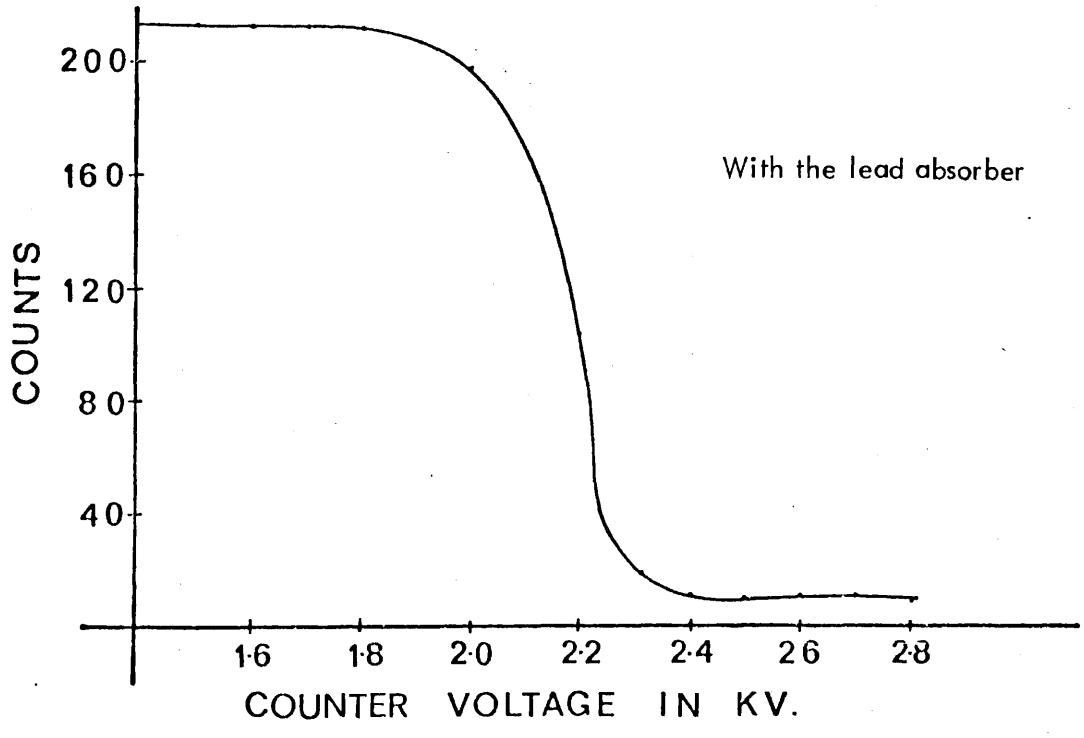

Fig. 6.2.1 The observed counting rate plotted against the anticoincidence counter voltage

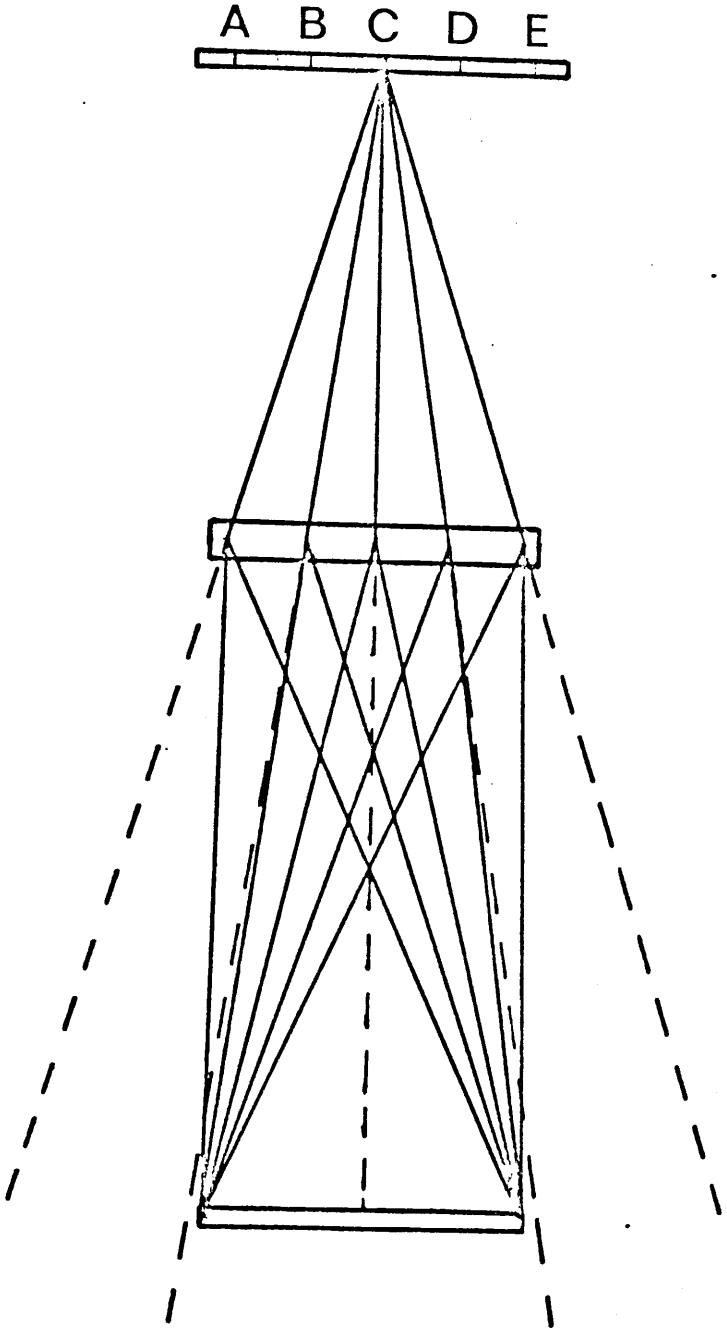

Fig. 6.3.1 A graphical representation of the geometric limitations of the chamber for recording scattering

points gave 25 typical trajectories of particles incident at different angles as allowed by the geometry of the system. The area of the two counters and the scatterer are almost the same.

Trajectories in the second gap represent the direction of the scattered particles with the minimum and the maximum angle of scattering that could be recorded. The possibility that a particle scatter through a certain angle was determined for each trajectory. The results for all trajectories were combined to give an overall efficiency. Thus a correction factor was obtained for each angular group. Figure (6.3.2) shows the efficiency of the system to record tracks scattered at different angles. From the graph it can be seen that there is a maximum decrease in efficiency of only 4% for angles as large as 15°. Application of these corrections increases the mean projected angle by only 2%.

The other factor which might effect the scattering distribution is that the projection of the scattering angles on a plain parallel to the chamber walls, i.e. the plane of photography, were measured, whereas the theories considered the plane containing the initial direction of the scattered particle. A graphical assessment Fig. 6.3.3 has shown that the difference between the results in these two cases is very small, i.e. about 3% for a particle incident at an angle of 20° and scattered through an angle of 10° (Mishra, 1969). Since the maximum angle of incidence accepted in the present work was only 15°, the actual correction would be smaller.

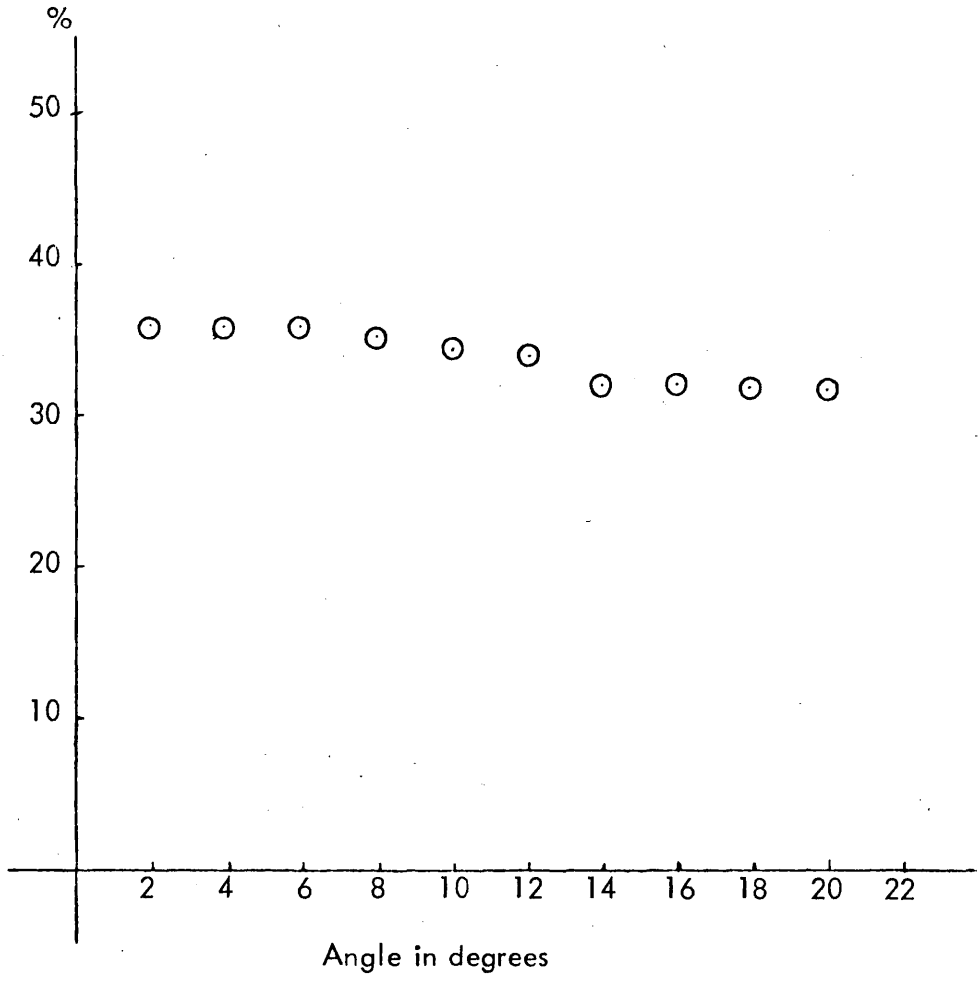

Fig. 6.3.2 Recording efficiency for different scattering angles

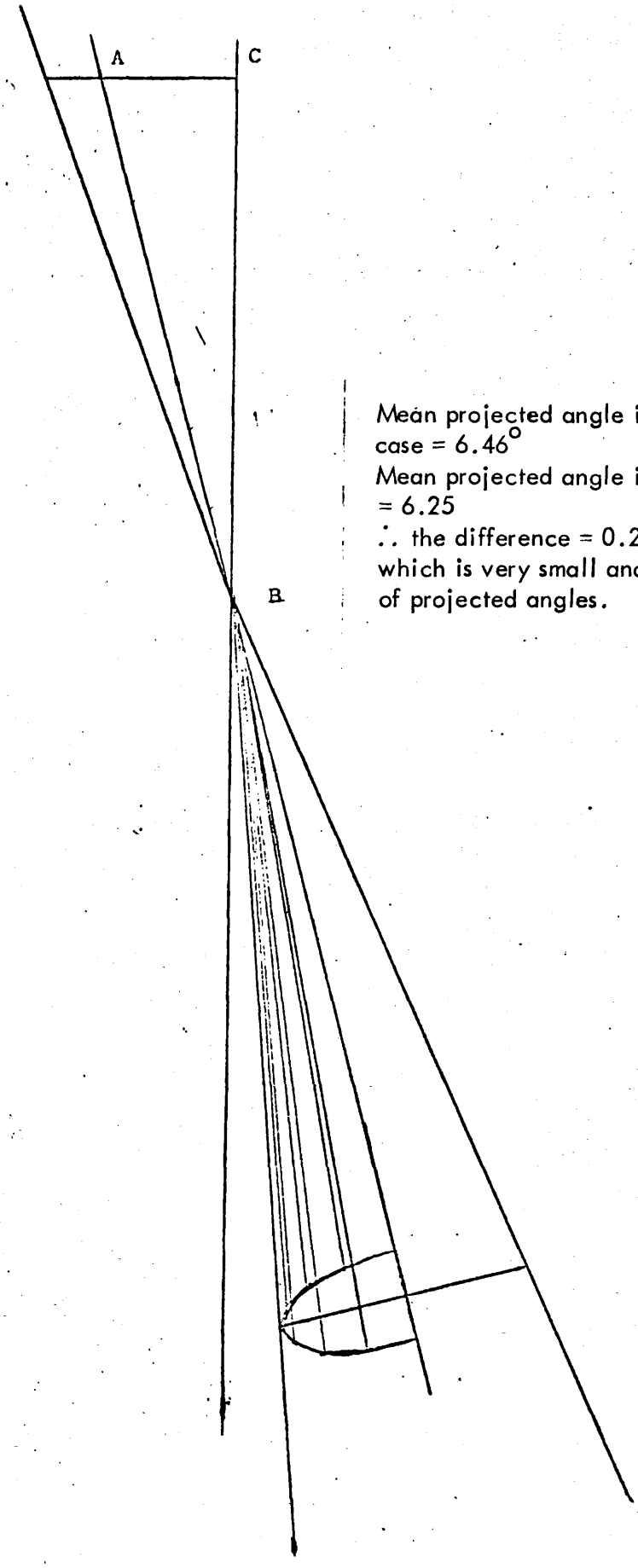

Mean projected angle in the present case = 6.46°
Mean projected angle in case of theory = 6.25
$\therefore$ the difference = $0.21^{\circ}/6.25^{\circ}$ = 3.3% which is very small and justifies the use of projected angles.

Fig. 6.3.3 Assessment of the error involved in the projected distribution when compared with the theoretical condition

6.4 Multiple scattering in lead

A 35 mm. camera was used to photograph the selected events. Any photograph that contains more than one event, (or more than one track in the second gap) was omitted from the analysis.

A D - Mac table was used to transfer the information from the negatives selected for analysis to a digital form on tape which can be handled much more easily. Ten arbitrary points were chosen on the tracks in each gap and the co-ordinates of these points were obtained. Straight lines were constructed by the least square method for the tracks above and below the scatterer, and the scattering angle was measured from the difference of the slopes. The selected events were grouped in the angular range $0^{\circ} - 1^{\circ}$, $1^{\circ} - 2^{\circ}$, $2^{\circ} - 3^{\circ}$, ... $19^{\circ} - 20^{\circ}$ and so on. The number of events in each angular group were displayed in the form of a histogram from which the experimental mean angle of scattering and the root mean square were calculated, these values being useful in comparison with the theoretical predictions. The majority of the analysed events have scattered with angles that lie in the range 0° to 18°, although a few cases of larger angles were observed.

Figure 6.4.1 shows some typical examples of the selected events. The accuracy with which the scattering angle can be measured is 1.5 milliradian, so the probable error in the angular measurement is 0.09 degree.

For the measurements described in this chapter electrons have been excluded.

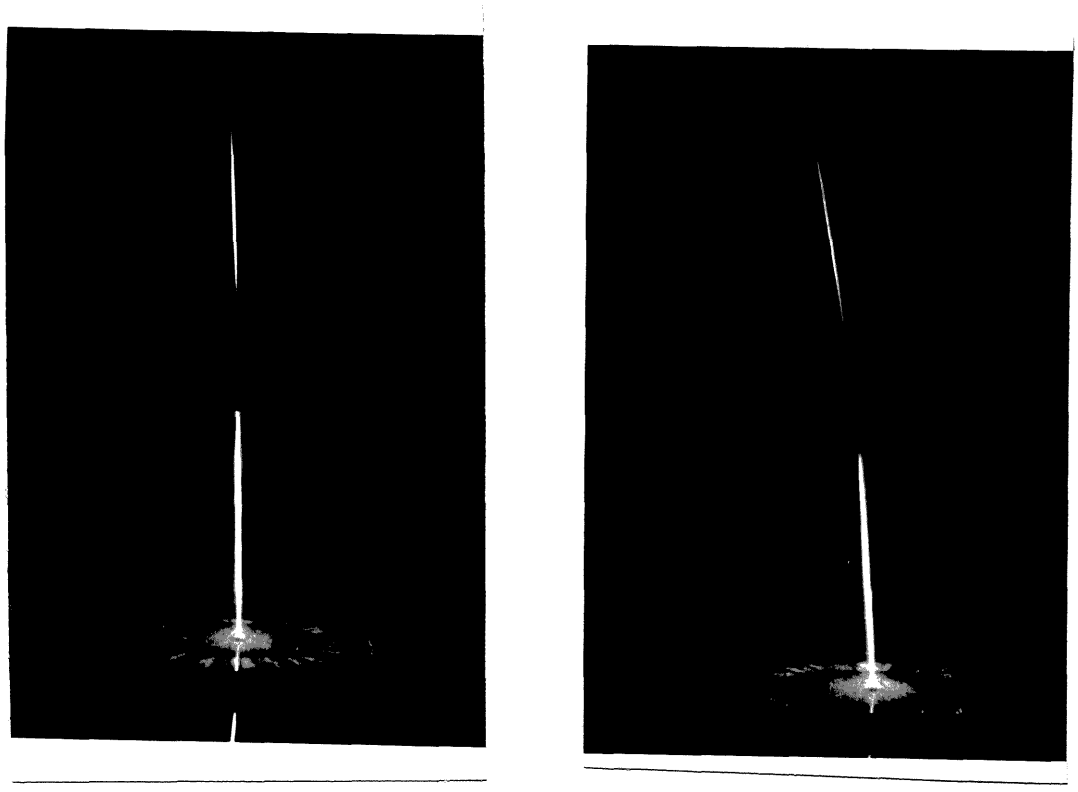

Fig. 6.4.1 Photographs of events analysed

Electrons would have to travel about 34.5 radiation lengths (7 inches of lead) without producing a shower. This is most unlikely, since fast electrons produce showers in one or very few radiation lengths. Protons cannot be excluded. But they have been estimated to be less than 4% (Alkofer et al., 1970). Thus their contribution to the distribution is very small and could be accounted for if necessary. It was therefore concluded that most the observed particles were muons.

6.4.1 Experiment A; Using anticoincidence counter

Two sets of results for different muons mean energies were observed. For this experiment the anticoincidence counter (3) was assumed to be 100% efficient, and no correction was used. For the first set of results a 5 cm block of lead was used as an absorber, and it was placed between the anticoincidence counter (3) and the coincidence counter (2). Thus only particles that were detected simultaneously by counters (1) and (2) and stop in the lead absorber will give an output signal which triggers the Marx generator. The experimental arrangement is shown in Figure 6.4.1.1. The angle of scattering for the events selected for analysis was measured using the D-Mac table, and the results were grouped according to their angular range and displayed in a histogram Fig. 6.4.1.2. The muons studied in this experiment have a maximum energy of 127 MeV which corresponds to a range of 7.5 cm of lead, and minimum energy of 63 MeV which corresponds to 2.5 cm of lead. These values gives a mean kinetic energy of 95 MeV. From the experimental distribution the mean angle of scattering was 5.28^{o} and the root mean square value was 7.21^{o}. Figure 6.4.1.2 shows also the

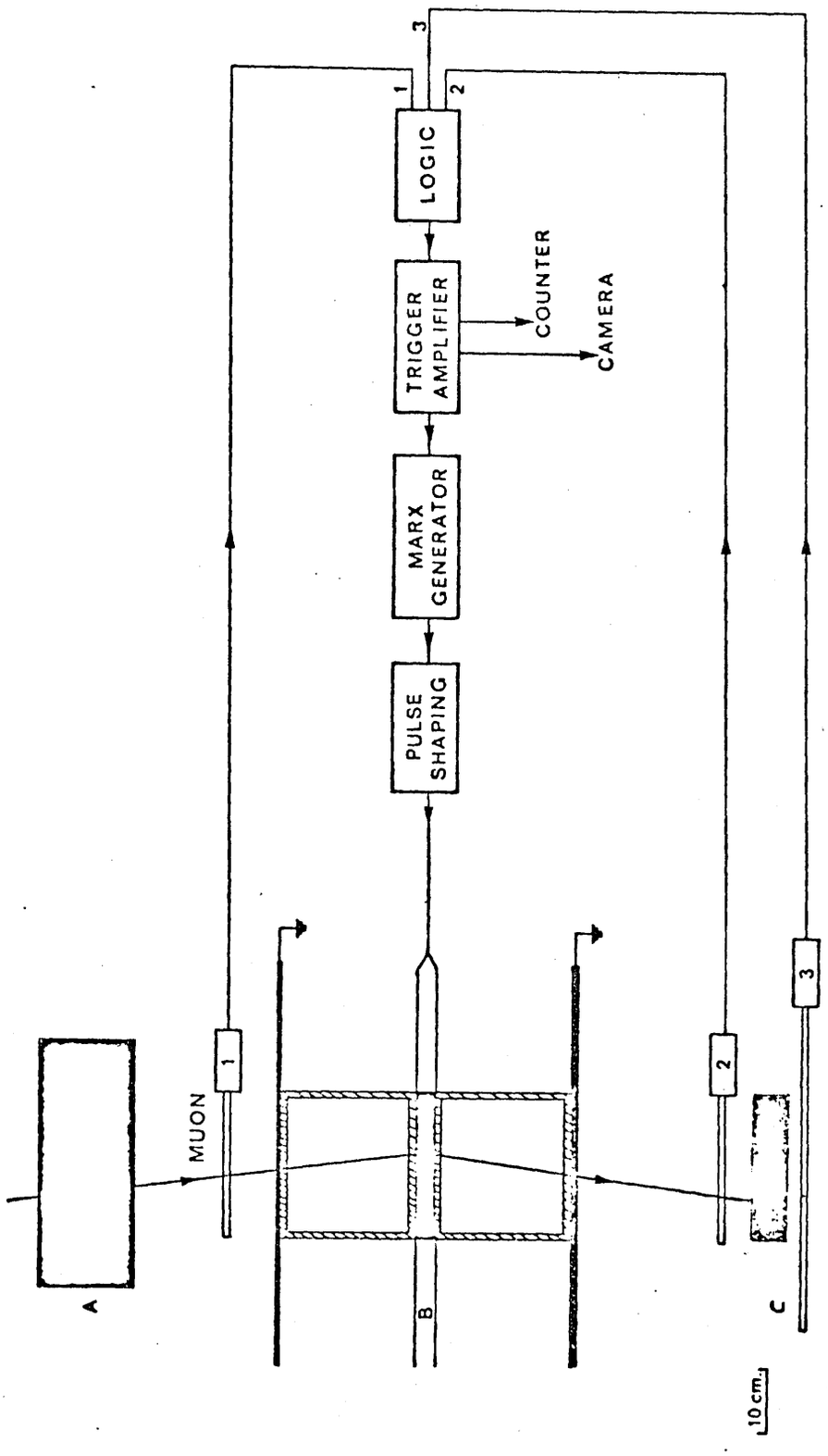

Fig. 6.4.1.1 The experimental set up

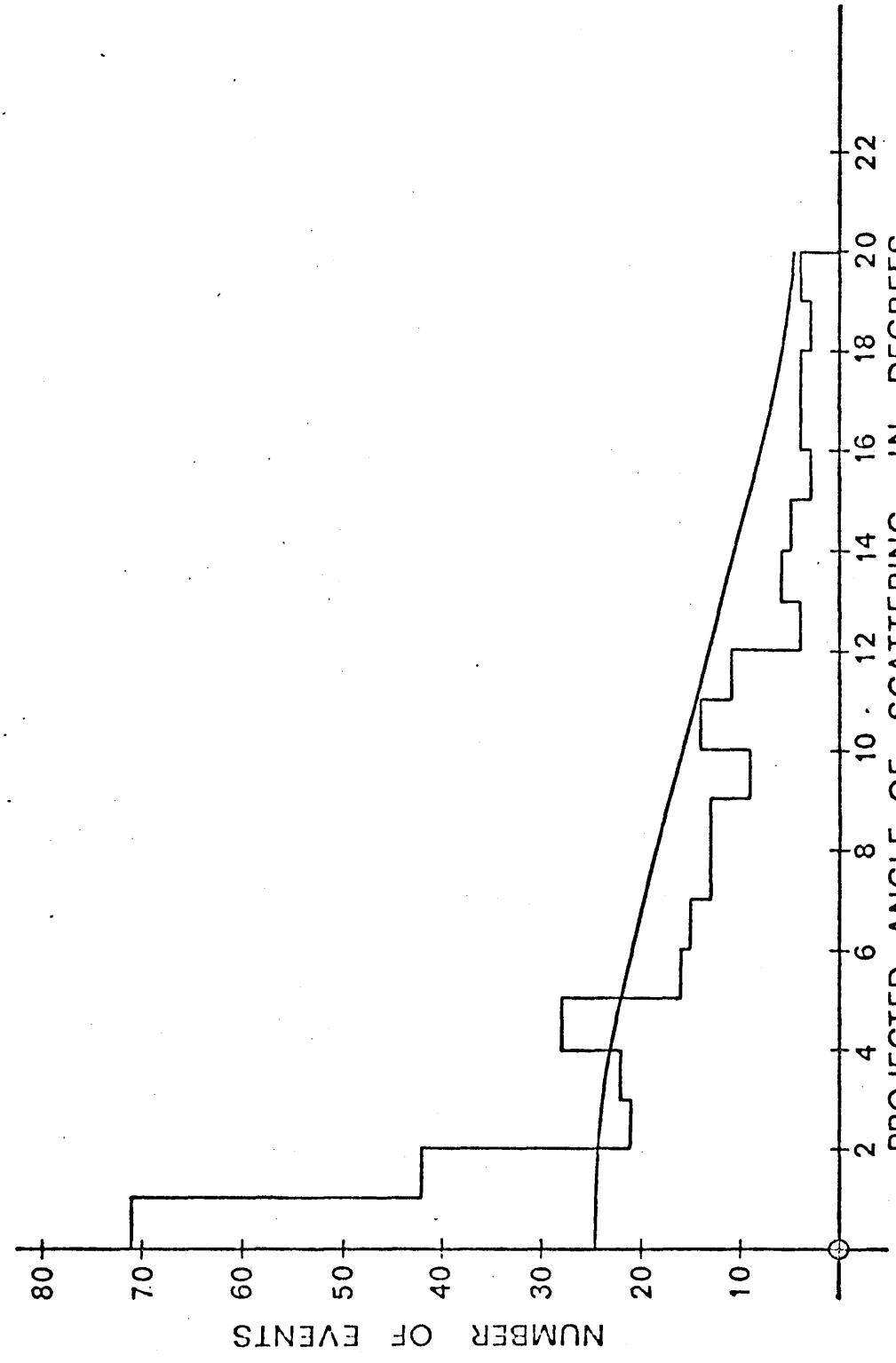

Fig. 6.4.1.2 The observed distribution of multiple scattering angle for 100 MeV particles depicted as an histogram. The curve represents the theoretical model normalised to the same area.

expected multiple scattering distribution normalized to the experimental results. From the distributions one can notice the large deviations of the experimental results from the theoretical predictions.

A second set of results was obtained with the 5 cm of lead placed above the coincidence counter (2), and 1.5 cm of lead used as an absorber placed between the anticoincidence counter (3) and the coincidence counter (2). Figure 6.1.1 shows the experimental arrangement. The 5 cm lead absorber was replaced by the 1.5 cm lead plate to narrow the momentum interval. This lead plate was chosen to be bigger than the coincidence counter (2) to insure that all particles detected simultaneously by counters (1) and (2) had to pass through it. Its dimensions were 31 x 31 x 1.5 cm^3. The projected angle of scattering was measured using D-Mac table, and results were displayed in a histogram, Fig. 6.4.1.3. The observed muons in this arrangement have a maximum energy of 148 MeV which corresponds to 9 cm of lead and a minimum energy of 127 MeV related to a range of 7.5 cm of lead. The mean muon energy was 137.5 MeV. The expected multiple scattering distribution was calculated and normalized to the experimental results Fig. 6.4.1.3. Again the difference between the two distributions is very clear. From the histogram the mean of the scattering angle was found to be 4.37°, and the root mean square value is 6.4°. The electronics used in obtaining both sets of results were described in 3.4.

6.4.2 Experiment B; Using cosmic ray absorption technique

To account for any inefficiency in the anticoincidence detection system,

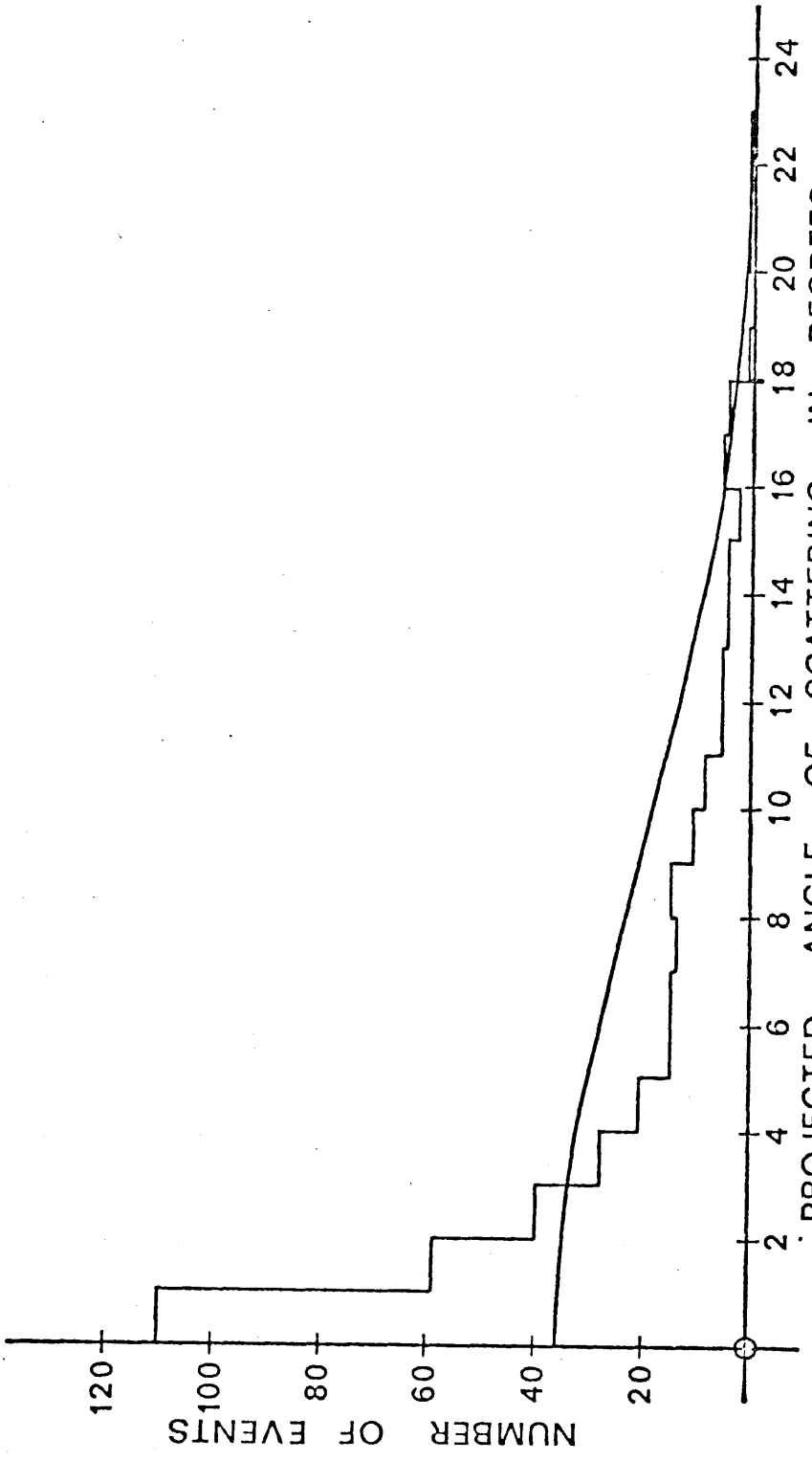

Fig. 6.4.1.3 The observed distribution of multiple scattering angle for 135 MeV particle depicted as an histogram. The curve represents the theoretical model normalised to the same area

i.e. to correct for any high momentum contamination which would contribute mainly to the small angle region of the experimental distribution, the angular distribution of the particles observed with the lead absorber removed was obtained. This distribution was subtracted from the distribution obtained (in the same length of time) with the lead absorber in place.

The scattering in 2.5 cm of lead was observed alternately with the lead absorber in its place for 1 hour, and then with the lead absorber removed for the same time. This sequence was repeated throughout the experiment. Figure 6.1.1 shows the experimental set up.

The experimental results obtained with and without the lead absorber, are displayed in a histogram shown in Figure 6.4.2.1. Figure 6.4.2.2 shows the corrected experimental distribution, i.e. the distribution that should correspond to particles that stop in the lead. In the theoretical assessment of the experimental results which will be discussed later, section 6.5, the corrected experimental distribution will be used. The observed muons in this experiment have a maximum energy of 148 MeV, and a minimum energy of 127 MeV and the mean muon energy was 137.5 MeV. A D-Mac table was used in measuring the angle of scattering. The electronics used in obtaining these results are the same as the one used in experiment A. (see 6.4.1). From the results the mean scattering angle was 5.63° and the root mean square was 7.57°.

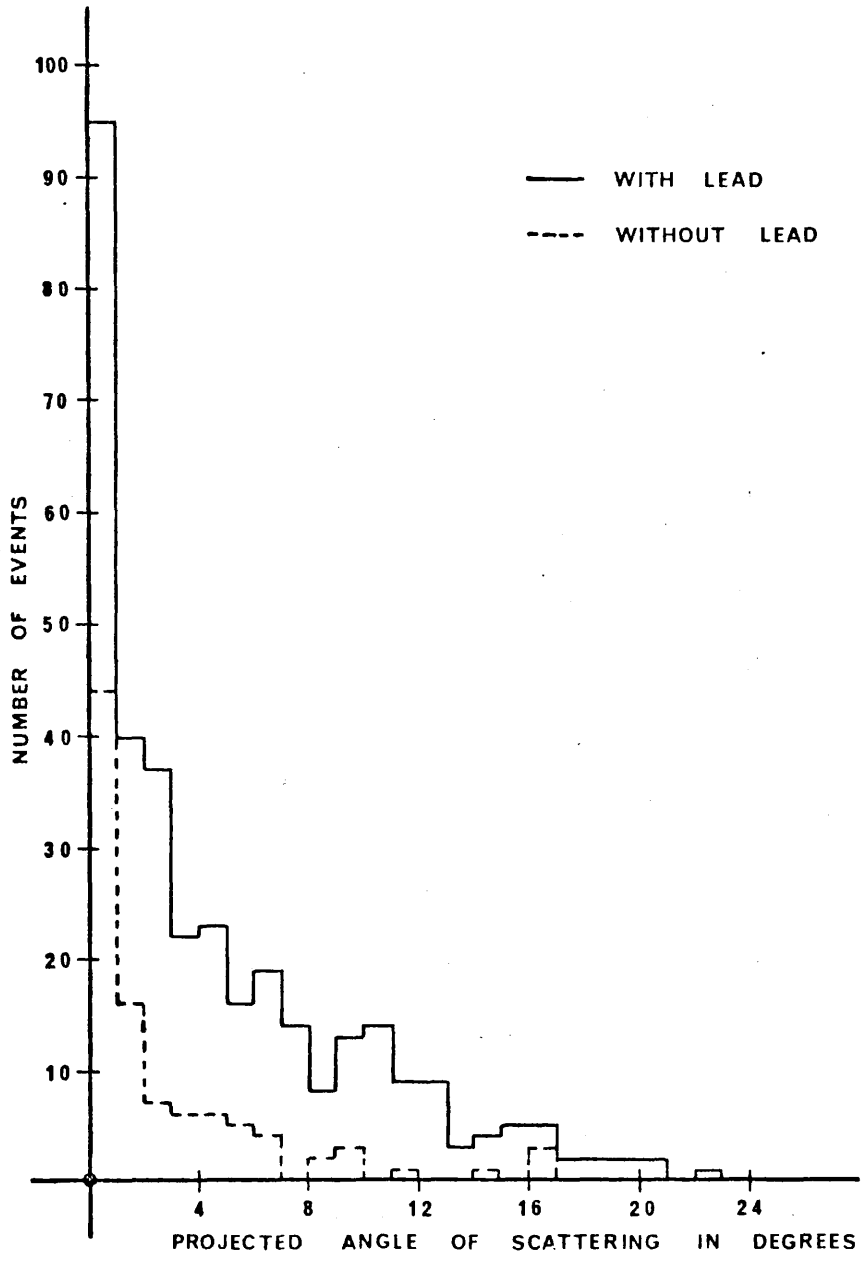

Fig. 6.4.2.1 The observed distribution of multiple scattering in lead with the lead absorber in its place and with the lead absorber removed. The results are displayed in the form of a histogram.

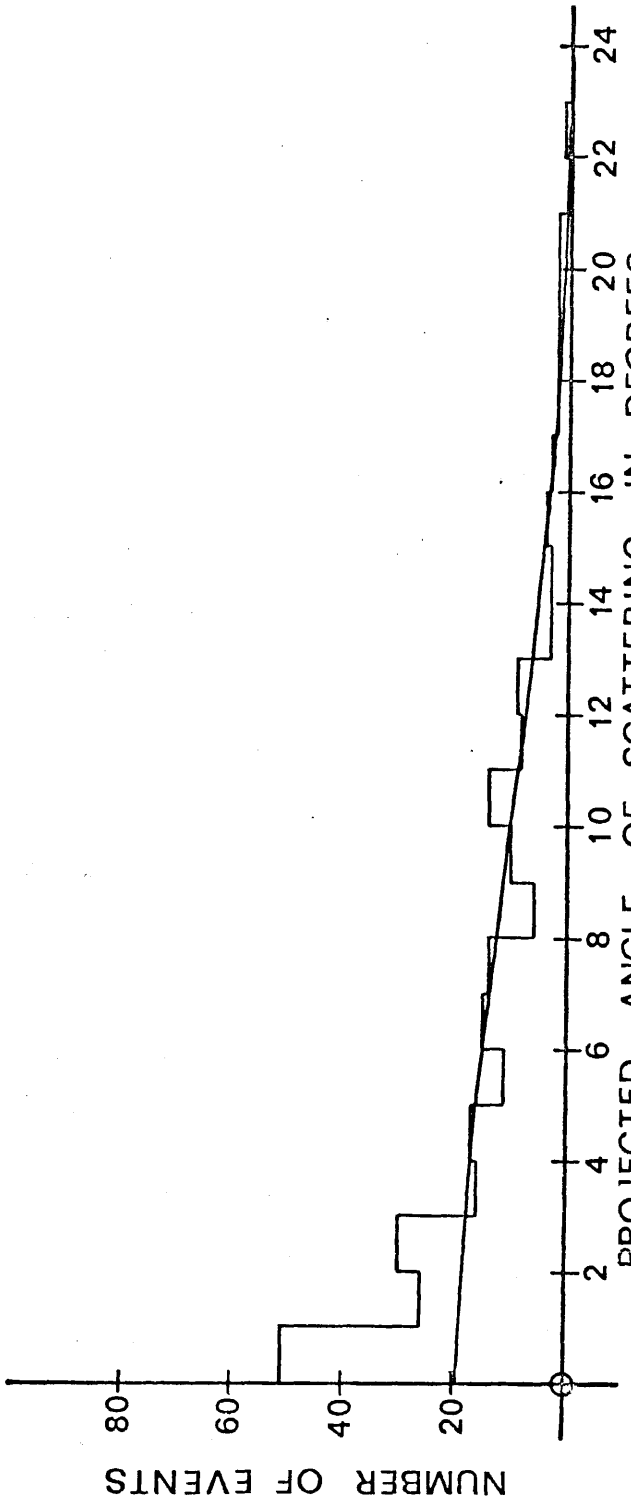

Fig. 6.4.2.2 The early subtracted experimental distribution of the multiple scattering in lead
The curve represents the theoretical model normalised to the same area

6.4.3 Experiment C; Integrated circuit electronics plus absorption technique

This experiment is similar in many ways to the experiment described in 6.4.2. The same experimental arrangement was used, and again the subtracted distribution of muons was obtained. The only difference between the experiments described in 6.4.2 and here is that in the first the valve electronics (3.4) were used while in the second the logic control employing integrated circuits (3.6) was used. The output of the logic circuit used to trigger the trigger amplifier was taken from (out 1) of the logic (3.6.2.)

The muons observed in this experiment have the same mean energy, 138 MeV, as those of experiment B. Figure 6.4.3.1 shows the experimental distribution obtained with the lead absorber in its usual place, and also the distribution with the absorber removed. Figure 6.4.3.2 shows the subtracted distribution. From this histogram the mean angle of scattering was found to be 5.88°, and the root mean square angle was 7.7°.

6.5 Analysis of Results

Various range-energy relation graphs by Wick (1943), Bethe (1953), Rossi (1941) and others exist; but the difference between them is very small. In determining the energy of muons studied in this experiment, the range-energy relation graph by Rossi was used. If we take experiment C as an example we get the minimum energy for muons to trigger our system which corresponds to a range of 7.5 cm of lead was found to be 127 MeV, a maximum range of 9 cm of lead sets an upper limit to the energy of muons that triggers the system, this upper limit was found to be 148 MeV. The mean kinetic energy

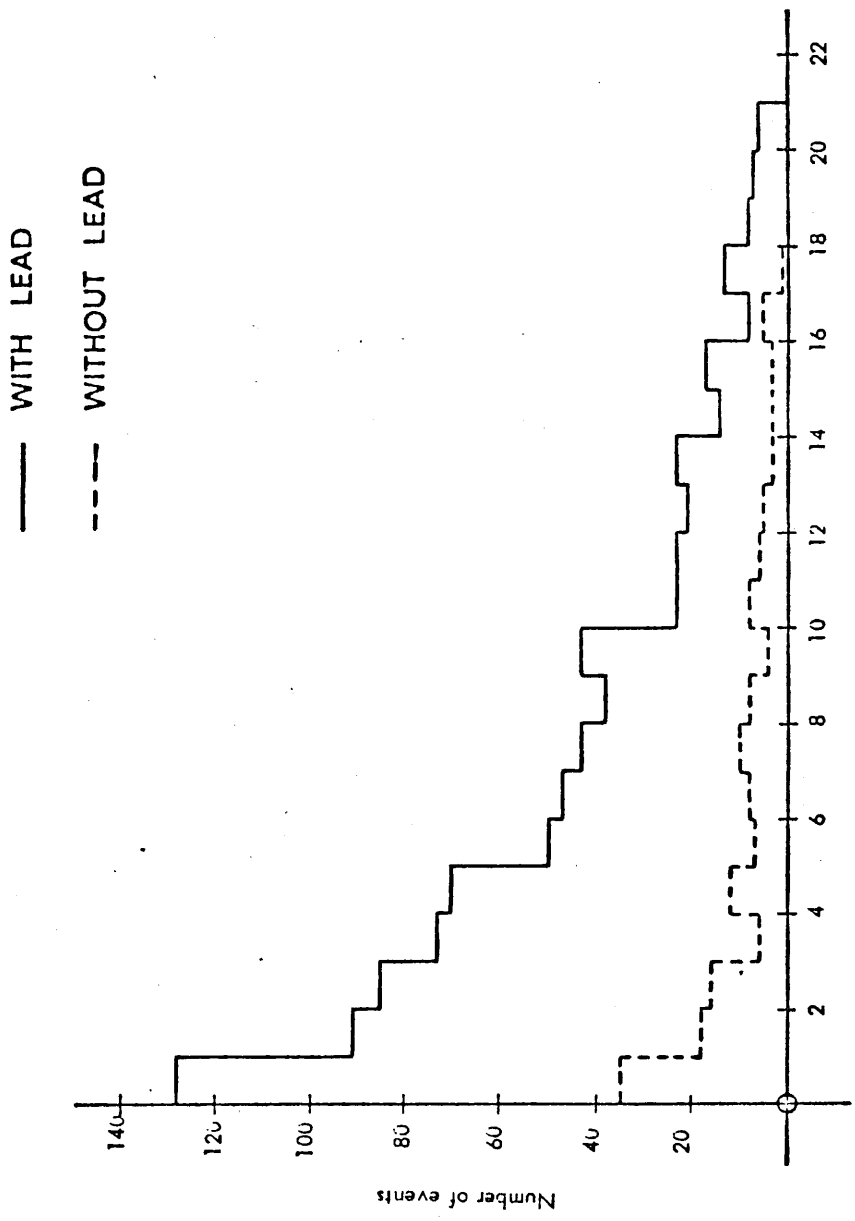

Fig. 6.4.3.1 The experimental distribution of the multiple scattering angle in lead obtained with and without the lead absorber

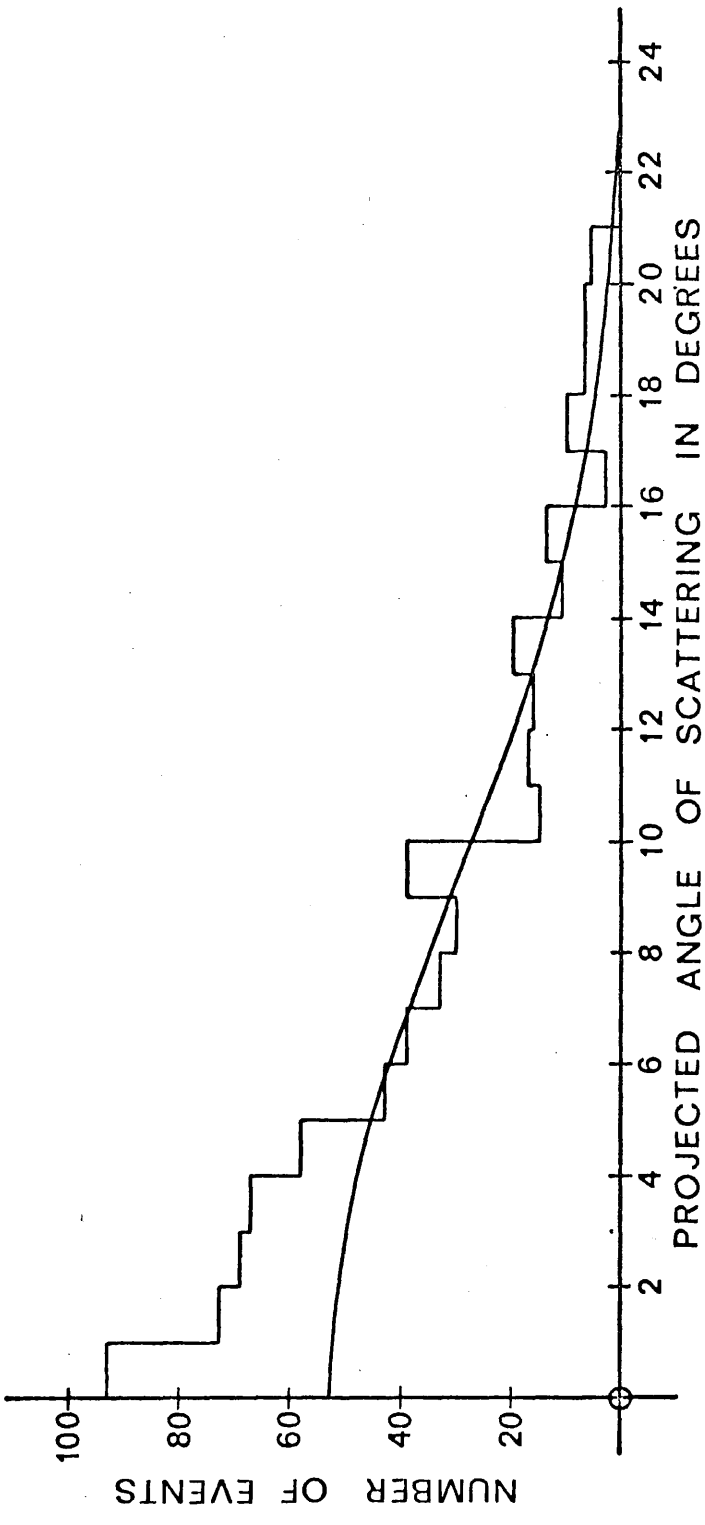

Fig. 6.4.3.2 The later corrected experimental distribution of the multiple scattering angle in lead. The curve represents the theoretical model normalised to the same area.

of these muons is 138 MeV and the mean momentum is 219 MeV/c. These values were compared with the values obtained by the use of the range-energy relation calculated by Sternheimer (1959, 1960) which includes the density effect, and where it was assumed that the ionization potential for lead is I = 1070 eV. It was found that the calculated muon energies agrees well with the values obtained by the Rossi graphs. Therefore using the Rossi graph the muon energies were obtained for each experiment. The total energy of muons observed in experiment C was 243 MeV, thus from the equation:

$$E = m_o c^2/(1 - \beta^2)^{\frac{1}{2}} \qquad 6.4.1$$

where E is the total energy and $m_o c^2$ is the muon rest mass, we get

$$\beta^2 = 0.81 \quad \text{and hence} \quad \beta = 0.9$$

The muon momentum was calculated from

$$E^2 = P^2 c^2 + m_o^2 c^4$$

and was found to be $p = 219$ MeV/c.

Using these values, the parameters G and Q were obtained from equations (2.1.36) and (2.1.28) respectively:

$$G = 7.32$$

$$Q = 3.694 \times 10^{-3}$$

Substituting the values of G and Q in equation (2.1.46) one gets the theoretical multiple scattering distribution expected for muons of this particular energy scattered through 2.5 cm of lead according to Cooper and Rainwater theory of multiple scattering. A computer program was used in solving equation 2.1.46 for particular G and Q and the theoretical distribution was obtained.

The Cooper and Rainwater theory of multiple scattering was adopted in the analysis of these experimental results because many experimentalists have found that the distribution predicted by this theory was in better agreement with their experimental results than the other theories (chapter 2.2), and that Cooper and Rainwater have taken into account the nuclear size effect as well as the shielding effect. The values of E, P, G and Q were calculated for each experiment. These values are listed in table 6.4.1 and the predicted angular distributions were computed for each of these experiments. The predicted angular distributions were normalized with regard to area and fitted to the experimental results of experiment A; and to corrected experimental distributions of experiments B and C. Figures 6.4.1.2, 6.4.1.3, 6.4.2.2 and 6.4.3.2 show the theoretical distribution fitted to the experimental results.

Table 6.4.1

Experiment	E mean MeV	P mean MeV/c	β	G	Q $\times 10^{-3}$
A_1	95	170.78	0.85	7.29	5.91
A_2	138	219	0.9	7.32	3.699
B	138	219	0.9	7.32	3.699
C	138	219	0.9	7.32	3.699

6.6 Multiple scattering in mercury

From the results obtained in the experiments described in section 6.4 it was noticed that the experimental distribution deviates from the calculated theoretical one. It was thought that this might be due to the nature of the scattering material, e.g. due to the crystal structure of the scattering material (lead). Consequently a different scatterer, mercury, which has no crystal structure has been used.

The mercury scatterer was enclosed in a perspex box; the thickness of the walls was 0.6 cm. The mercury scatterer was placed between the two high voltage plates, in the same experimental arrangement as the one used in experiment Cdescribed in section 6.4.3.

Figure 6.6.1 shows the results and the subtracted histogram is shown in Fig. 6.6.2 with the fitted theoretical distribution. A chi squared test applied to these results shows that the experimental distribution is not in agreement with that predicted.

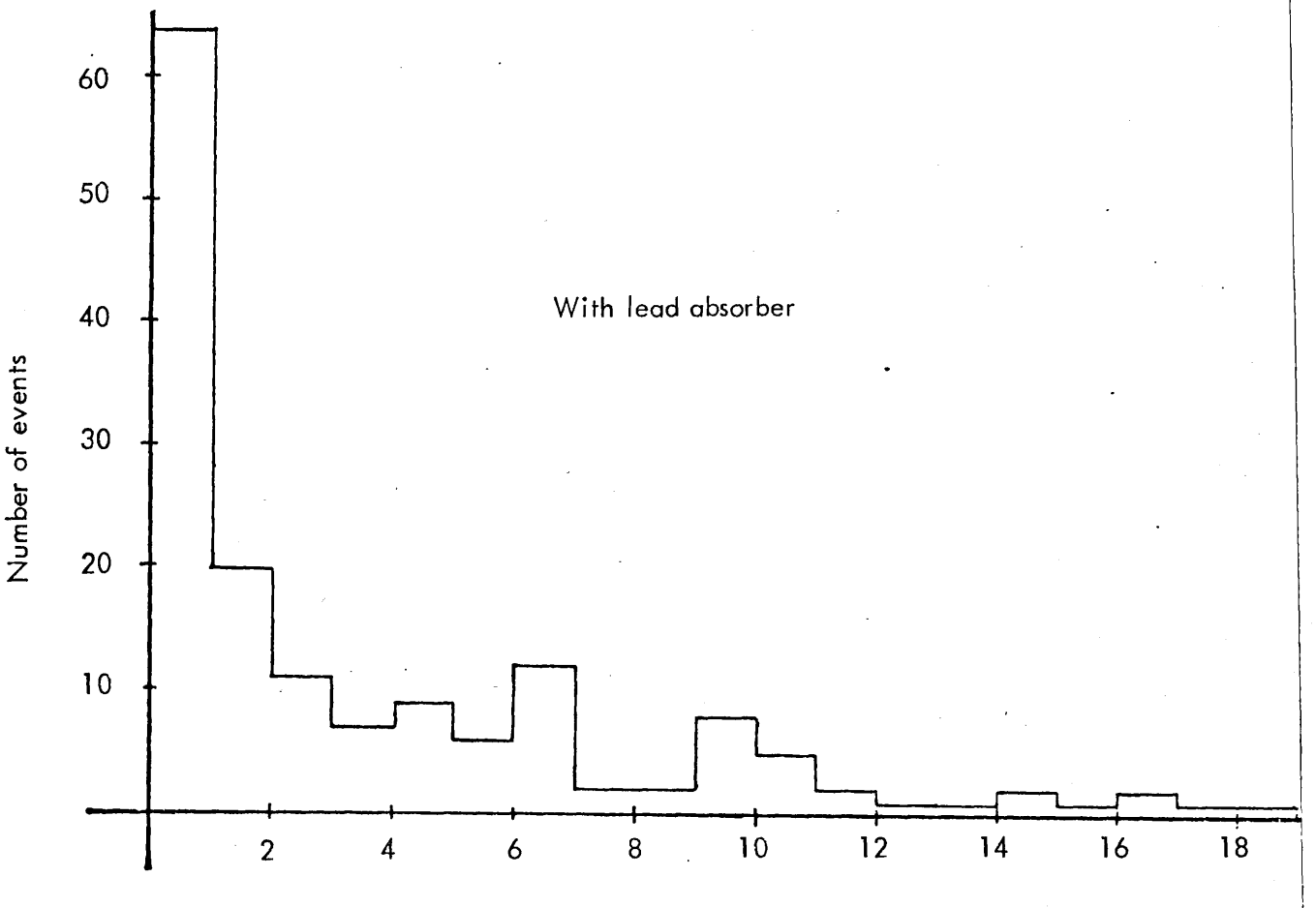

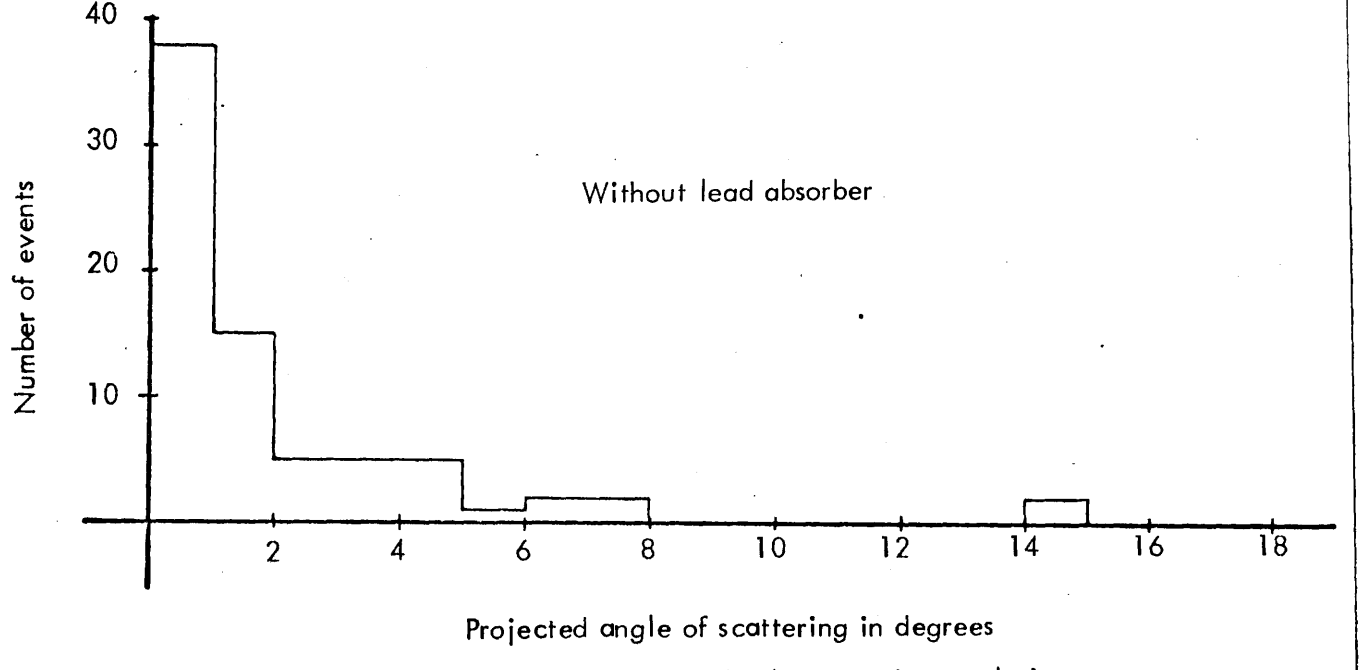

Fig. 6.6.1 The observed distributions of multiple scattering angle in mercury obtained with and without the lead absorber

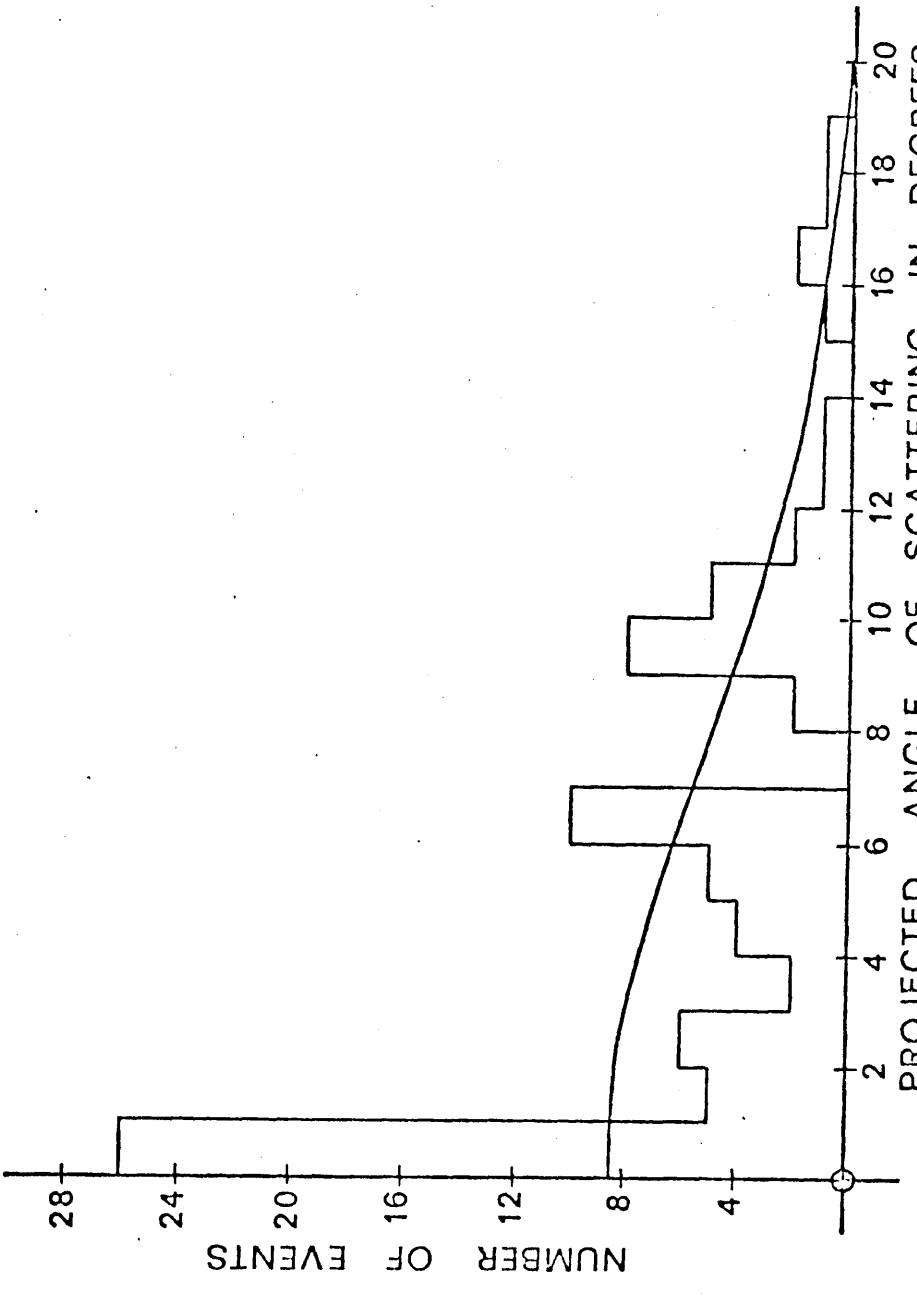

Fig. 6.6.2 The corrected experimental distribution of the multiple scattering angle in mercury depicted as a histogram. The curve represents the theoretical model normalised to the same area.

CHAPTER 7

Multiple Scattering of Identified Muons

7.1 Introduction

In this chapter the multiple scattering in lead and mercury, of cosmic ray muons identified by their decay electron, is described. Fig. 7.1.1 shows the experimental arrangement; an 8 cm carbon block was used as an absorber placed between the anticoincidence counter (3) and the coincidence counter (2). The two counters (2) and (1) are in coincidence; the logic electronics used were described in section 3.6. The output to the trigger unit, section 3.6, was taken from output 2. Therefore only muons that stop in the carbon absorber and after a certain time decay to an electron, which will be detected by the counter (3), will give a rise to an output pulse from output 2 to trigger the trigger amplifier and consequently trigger the Marx generator. The decay of a muon leads to the appearance of an electron and a neutrino and antineutrino.

$$\mu^{\pm} \rightarrow e^{\pm} + \upsilon + \bar{\upsilon}$$

This decay scheme for the muon was first confirmed by measurements on the decay-electron spectrum in a Wilson cloud chamber and by an absorption method; Leighton et al. (1949) used a cloud chamber exposed to cosmic rays to obtain the spectrum of decay electrons.

The energy distribution of the decay electron is a continuous spectrum and extends up to 50 MeV, the average energy of the decay electrons was found to be about 35 MeV.

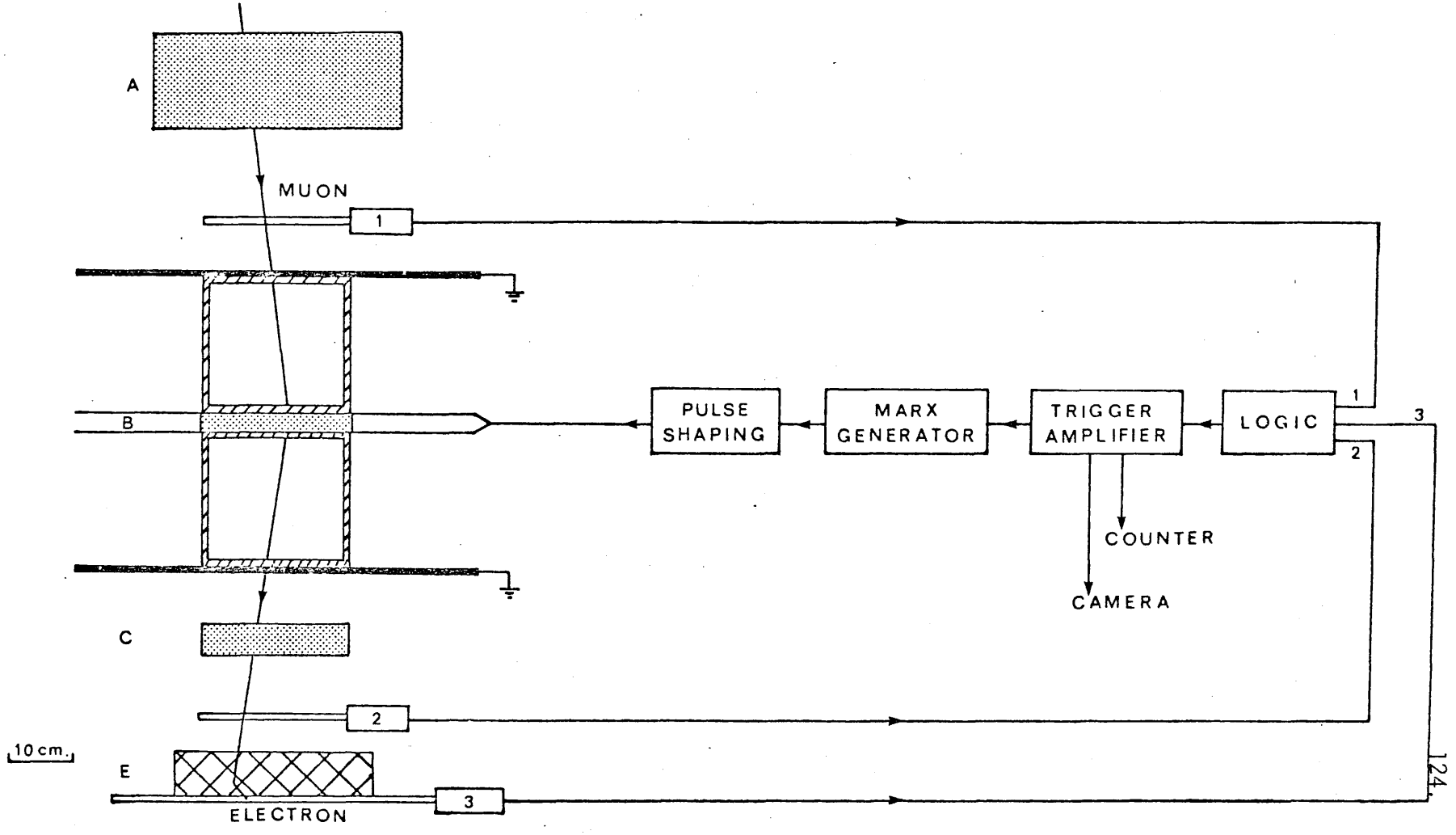

Fig. 7.1.1 The experimental arrangement with a carbon absorber

Free negative muons have the same decay constant as positive muons, negative muons stopped in matter may decay freely, but they may also interact with nuclei of the stopping substance and disappear by capture. The probability of a negative muon decaying increases as the atomic number Z of the stopping substance decreases (Conversi, Pancini and Piccioni, 1947). They measured the life time of both positive and negative muons stopping in various absorbers and they found that decay electrons were detected when negative muons were stopped in a graphite absorber. Their number was comparable with the number of decay electrons from positive muons stopping in graphite. Lifetime measurements of the muon by the delayed coincidence method were carried out by Rassati (1941). This method, which shows that muons decay exponentially was improved by Rossi and Nereson (1942). The most accurate measurements of the mean life time of cosmic-ray muons appear to be those by Bell and Hincks (1951). Their result was:

$$\tau\mu = (2.2 \pm 0.02)\ 10^{-6}\ \text{sec.}$$

Other accurate measurements of the life time of the muon have recently been carried out by a number of groups using accelerators; their results are very close to those of Bell and Hincks.

In this experiment graphite was chosen as an absorber because of its small atomic number, so that negative as well as positive muons will give a decay electron.

Since the average energy of the decay electrons was found to be 35 MeV the absorber thickness was chosen so electrons with this energy will be observed in counter (3).

The Feather relation is:

$$R = 0.543\,E - 0.160 \qquad 7.1.1$$

where R is the range in gm/cm^2, and E is in MeV.

The carbon absorber was 8 cm thick therefore using this relation, we find that $E \approx 34$ MeV.

Decay electrons which are generated at the top of the absorber will be detected by (3) if their energy is greater than 34 MeV. In the experiments that will be described later the electronic logic was set so whenever there is a coincidence signal between (1) and (2) and nothing simultaneously coming from (3), and if after an interval of (say) 1-3 μs there was a pulse from (3) (and nothing from (1) and (2)), an output pulse was obtained from output 2.

The time after which the gate is opened and the length of time for which the gate stays open, is adjusted by two 10 Kohm helipots.

The efficiency of the detection system, and of the anti-coincidence counter which is the decay electron detector, were checked by placing the counter (2)

directly underneath (3) and counting for a certain length of time. No counts were observed from output 2 for 48 hours with the counter (2) below (3) and when the counter (2) placed in its usual place above (3) the counting rate was as expected. This counting rate was low because some of the decay electrons will escape detection by (3) because they will be moving away from it and some will stop in the graphite absorber. Also a few muons will decay into electrons in a time longer than that for which the gate will be open after detecting the passage of the particle.

7.2 Scattering of Muons in Mercury

In the present experiment the scattering of cosmic ray muons in a one inch thickness of mercury has been studied. The double gap chamber in the continuous streamer mode was used with the mercury scatterer placed between the high voltage electrodes which were two 1/16 inch, 24 inches square aluminium plates. The mercury scatterer was enclosed in a perspex box, the thickness of the perspex is 0.6 cm, the volume of the mercury is ($20 \times 20 \times 2.5$ cm^3).

The muons in this experiment have to go through 2.5 cm of mercury and 5 cm of lead before being stopped in 8 cm of carbon.

This gives them a minimum energy of:

$$E_{min} = 138 \text{ MeV}$$

and a maximum energy, $E_{max} = 180$ MeV

so the mean energy $E_{mean} = 159$ MeV.

These values were obtained from Nomograph given by (Hayakawa 1969 p.107).

Using these values it was found that the mean momentum is $p_{mean} = 242$ MeV/c.

Since $E_{total} = m_0c^2/(1-\beta^2)^{\frac{1}{2}}$, 7.2.1

the value of β was calculated, and found to be:

$$\beta^2 = 0.84 \quad \text{and} \quad \beta = 0.916$$

Using the values of β and the mean momentum p_{mean} the values of G and Q, given by equation 2.1.36 and 2.1.28 respectively, were obtained. Theoretical distributions were obtained from equation 2.1.46 with the aid of a computer.

The experiment was performed at sea level; 15 cm thickness of lead blocks was placed above the chamber and above the coincidence counter (1) to absorb the soft component of cosmic rays, to eliminate the electrons, to reduce the nuclear interacting particles, e.g. protons. Scattering events were photographed using the automatic camera; the film used was 35 mm Ilford Mark V.

All tracks selected for analysis were scanned by a D-Mac table, and the results were obtained on 8 hole paper tape. A computer was used to construct straight lines by the least square method for the tracks above and below the scatterer, and the scattering angle was obtained from the difference of the slopes. The accuracy with which the scattering angle was measured was 1.5 mrad (0.09 degree).

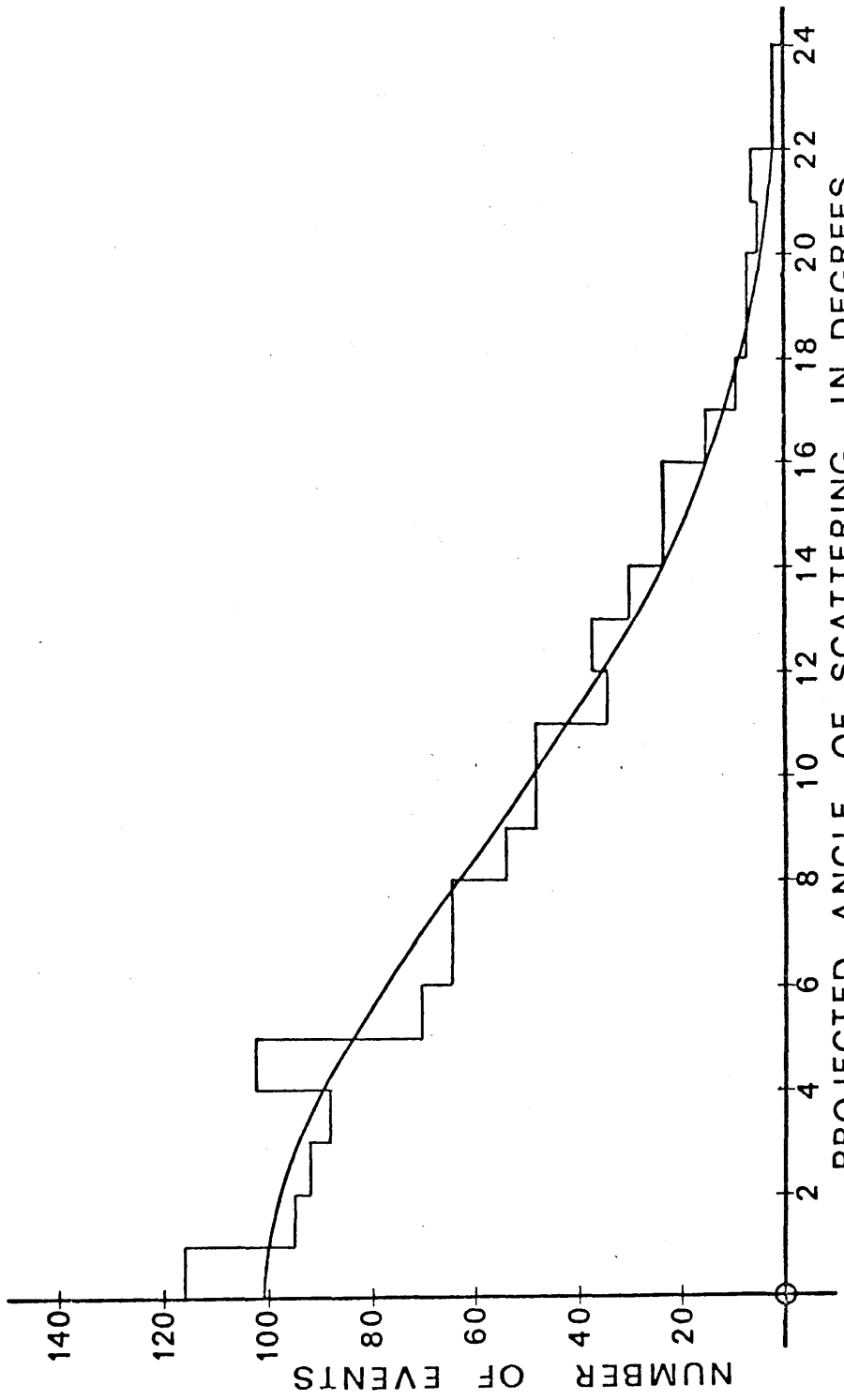

Fig. 7.2.1 The observed distribution of multiple scattering angle in mercury displayed in the form of a histogram. The curve represents the theoretical model normalised to the same area.

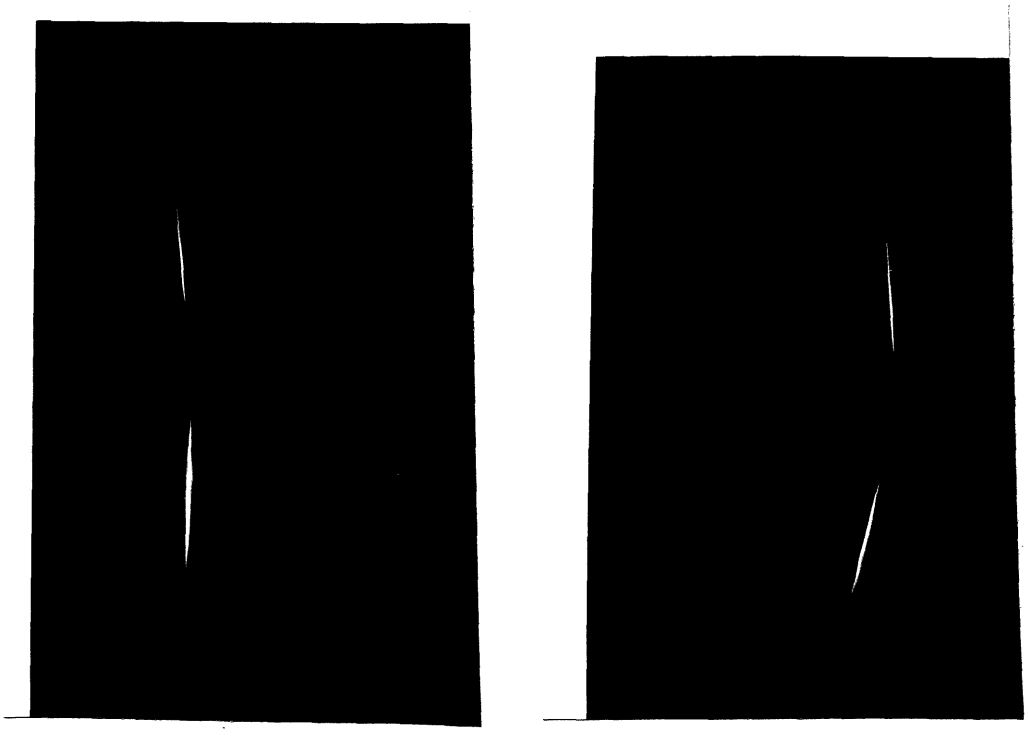

Fig. 7.2.2 The photographs of the analysed events

The particles were grouped in the angular range 0° - 1°, 1° - 2°, 2° - 3°, ... 12° - 13° and so on, their numbers were displayed in the form of a histogram Fig. 7.2.1. The theoretical distribution obtained from Equ. 2.1.46 after substituting the values of G and Q was normalized to the experimental results, this is also shown in Fig. 7.2.1. From the experimental histogram the mean scattering angle was found to be 6.37° and the root mean square value was 8.25°. Fig. 7.2.2 shows a typical track selected for analysis.

7.3 Muon scattering in lead

In this experiment a lead block (20 x 20 x 2.5 cm^3) was used as a scatterer. It was placed between the two high voltage plates (Fig. 7.1.1). The same electronic logic as was used in (7.2) was used for this experiment. Before starting this experiment the detection system was checked for efficiency and it was found to be satisfactory.

From the range - energy relation it was found that these muons have a minimum energy of:

E_{min} = 127 MeV which corresponds to a range of 7.5 cm of lead, i.e. 85.2 gm/cm^2.

The maximum energy corresponds to 7.5 cm of lead plus the 8 cm of carbon absorber, hence:

$$E_{max} = 170 \text{ MeV}.$$

Therefore the mean energy of the muons studied was

$$E_{mean} = 148.5 \text{ MeV.}$$

Since $E^2 = P^2c^2 + m_o c^2$, where E is the total energy of the incident particle the mean momentum was:

$$P_{mean} = 232 \text{ MeV/c.}$$

From Eq. 7.2.1 the value of β was calculated and found to be:

$$\beta = 0.909.$$

Using these values the parameters G and Q given by eq. 2.1.36 and eq. 2.1.28 respectively were found.

Putting these values in the computer program (appendix B) the theoretical distribution (eq. 2.1.46) was computed. The experimental results were analysed in the same way as the results of 7.2. The theoretical distribution was normalized by equalising the total areas, to the experimental histogram Fig. 7.3.1. From the experimental histogram the mean angle of scattering is found to be 6.5° and the root mean square is found to be 8.23. Application of the correction factors described in 6.3 to both these results and the results from 7.2 proved to be negligible; the first correction factor alters the mean angle and the root mean square by only 1% and the second factor was found to have a maximum correction of 3.3%.

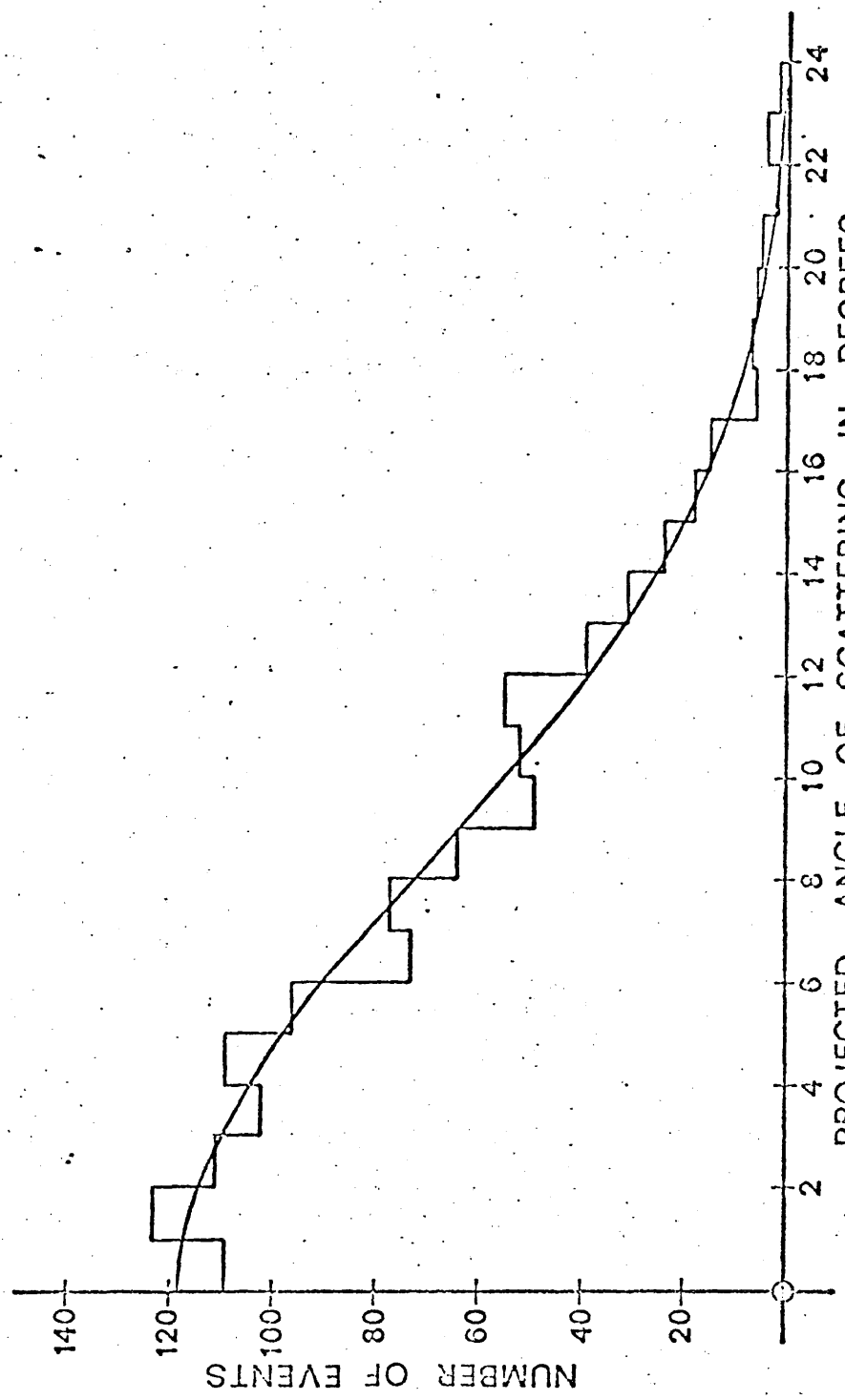

Fig. 7.3.1 The observed distribution of multiple scattering angle in lead presented in the form of a histogram. The curve represents the theoretical model normalised to the same area.

CHAPTER 8

Discussion of the results of multiple scattering of cosmic rays

8.1 Discussion of Experimental Scatter Spectrum

The multiple scattering of cosmic rays in a thick (2.5 cm) lead scatterer was observed in chapter 6; the experimental results were displayed in Figures 6.4.1.2, 6.4.1.3, 6.4.2.2 and 6.4.3.2. The expected distribution calculated on the basis of the Cooper and Rainwater model normalized to the experimental results is shown in the same figures. It was noticed that the experimental results deviate from the predicted distributions of muons especially in the small angle region. Using the Chi squared test on the three sets of results it was concluded that the assumed distribution very probably did not correspond to the observed one ($P_{\chi^2} = 0.001$).

Since both experiments B and C, described in 6.4.2 and 6.4.3, were carried out under the same conditions i.e. for particles of the same energy, Fig. 8.1.1 shows their combined results which will be referred to in the following discussion. The number of events analysed in experiments B and C with the lead absorber in its position was 1186 events. These events were collected over 140 hours, therefore the rate of events observed was 8.47 event/hour. From Hayakawa the sea level muon flux for the momentum studied was 3×10^{-3} part/cm^2/sec/sr/(GeV/c)^2. From the geometry of the experimental set up and the experimental conditions, the expected number of triggers due to muons in our experiment was 10.5 per hour. This number is larger than the observed rate (8.47 hour). The difference is due to two reasons: (a) not all events were analysed (b) in the calculation, the counter sizes were larger than the sensitive areas of the chambers used.

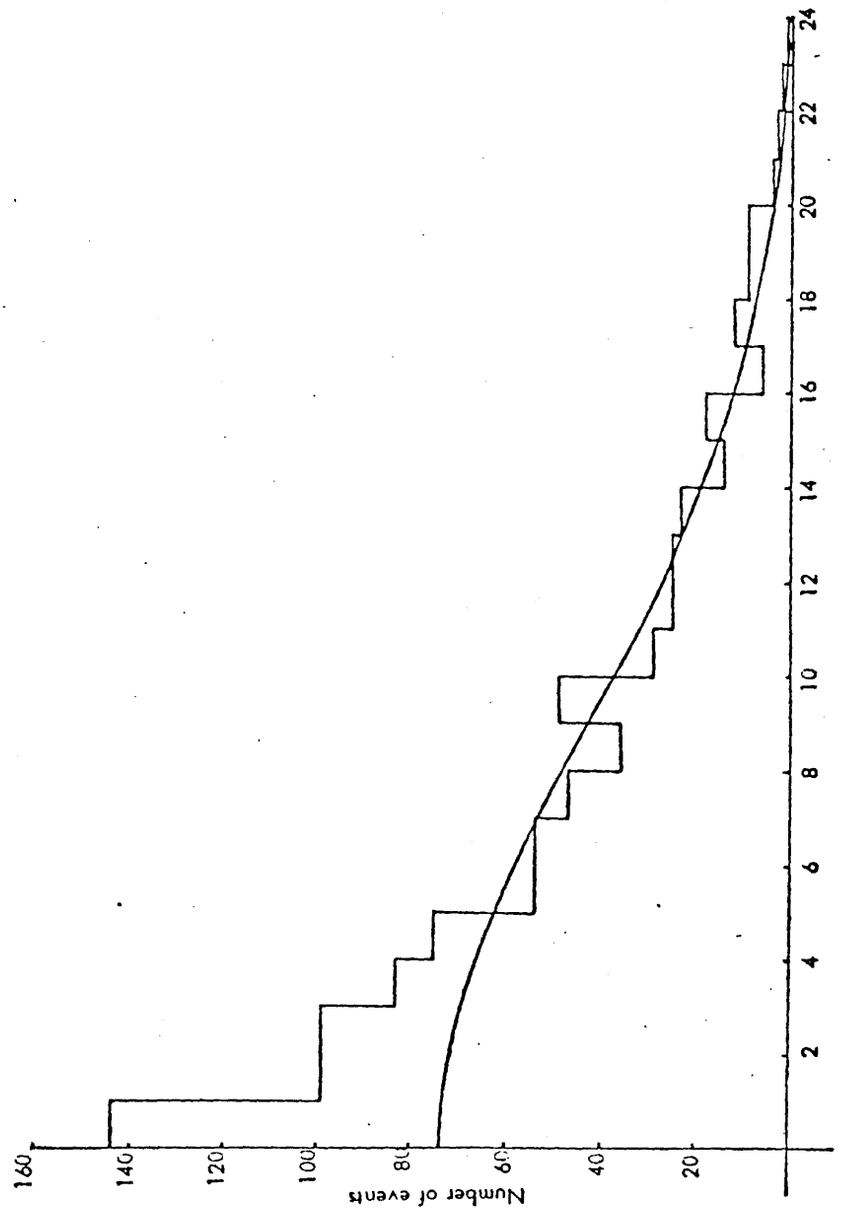

Fig. 8.1.1 The combined results of the distributions obtained in section 6.4.2 and 6.4.3

The percentage of protons in cosmic rays at sea level for our energy range was estimated to be less than 4% (Allkofer, 1970). Taking into consideration the 15 cm of lead block above the chamber, the percentage capable of triggering the system was calculated (see later) and found to be 2.3%. The effect of proton scattering on the observed distribution may be obtained as follows. If $P_{\mu}(\emptyset)$ and $P_{p}(\emptyset)$ represent the normalised theoretical scattering distributions for muons and protons respectively, and if x is the fraction of protons present in the beam, then the scattering function for this contaminated beam is:

$$P(\emptyset) = (1 - x)\ P_{\mu}(\emptyset) + x\ P_{p}(\emptyset) \qquad 8.1.1$$

Fig. 8.1.2 shows the theoretical distribution obtained from equations 8.1.1 when x = 5% fitted to the experimental distribution.

A close examination of the experimental distribution (Fig. 8.1.1) shows that it could be divided into two separate Gaussian distributions (Fig. 8.1.3). Assuming that all the events which scattered with an angle greater than 8^{o} were muons, then the broader distribution, if extrapolated to cover the range 0^{o} to 8^{o} (Fig. 8.1.3), gives a mean angle of 6.77^{o}, and when corrected for the geometrical factors, it becomes 7.06^{o} and the root mean square angle 8.86^{o}. These values compare reasonably well with the theoretical values; they are about 94% of the predicted one. The narrow component is contained in an angular range of 0^{o} to 5^{o} (Fig. 8.1.3b) and appears to be Gaussian in form with a mean angle of 1.6^{o}. This narrow component cannot be reconciled with any of the theories on multiple scattering when the established cosmic ray fluxes are used.

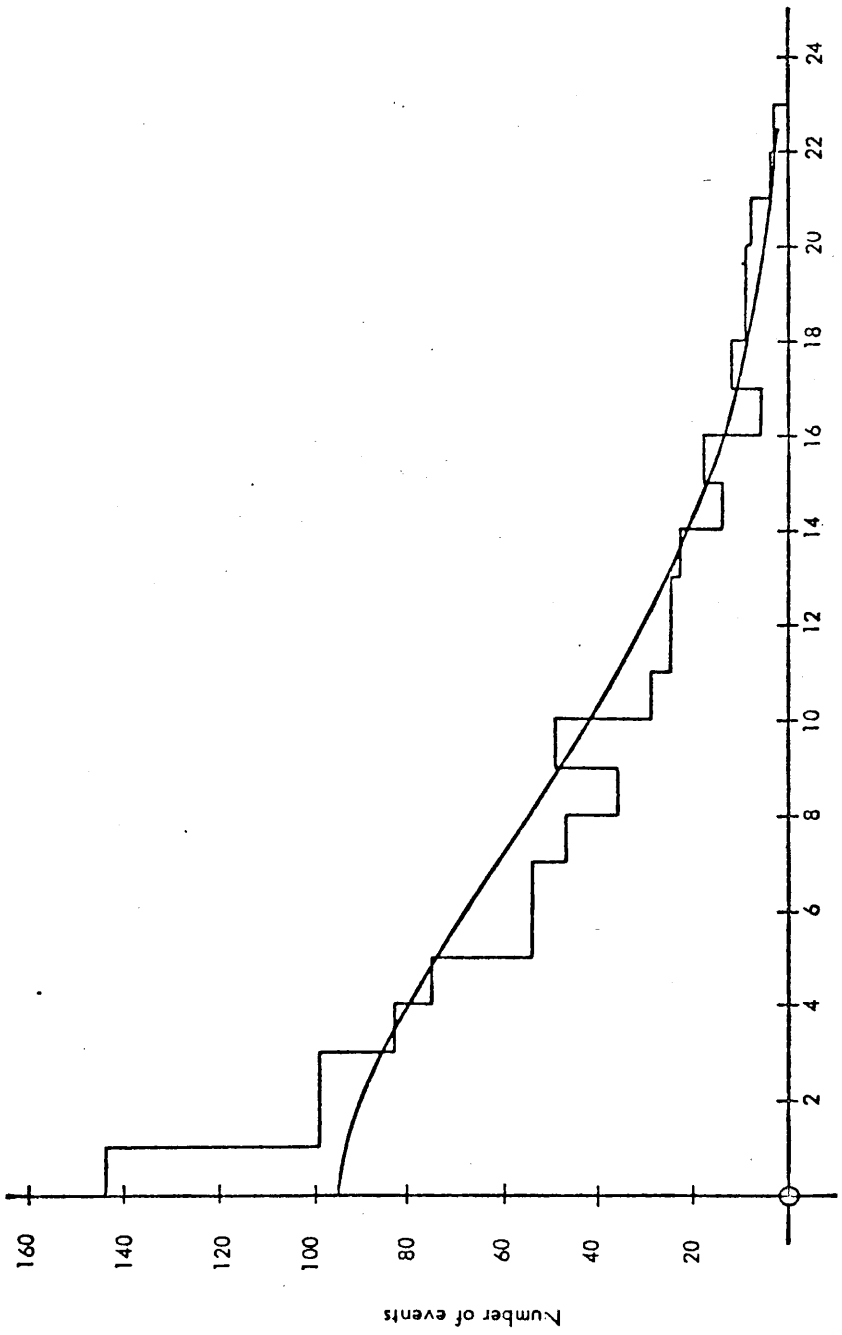

Fig. 8.1.2 The observed distribution represented in the form of a histogram. The curve represents the theoretical model for muons with 5% proton contamination

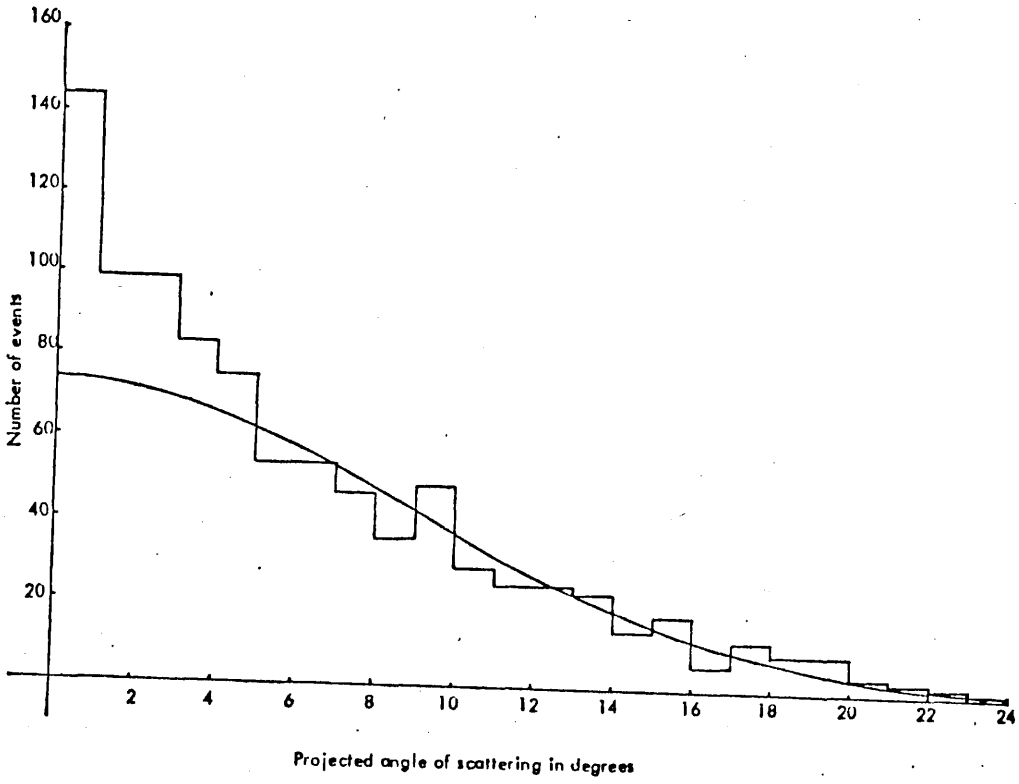

Fig. 8.1.3 (a) Histogram of the total distribution. The curve indicates the theoretical model for muons

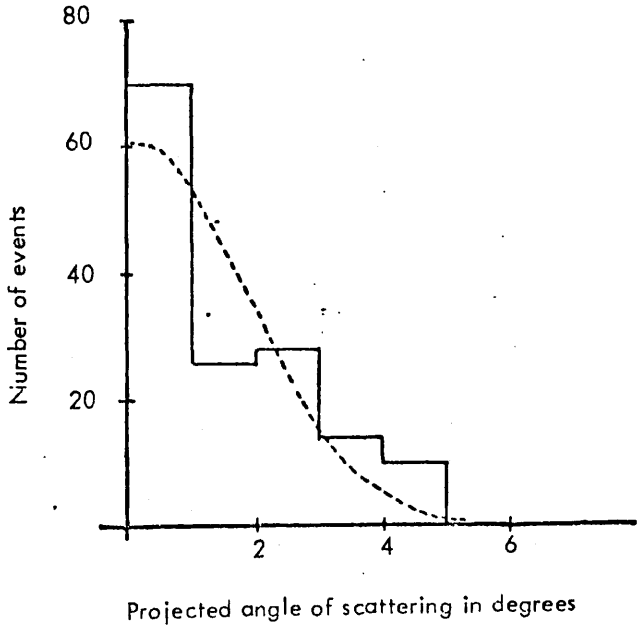

Fig. 8.1.3 (b) A histogram of the subtracted narrow component. The curve represents a Gaussian

To help analyse the problem a decision tree was constructed (Fig. 8.1.4). Three possible explanations were considered to account for the narrow component (2): apparatus defects (5), imperfect analysis (6) or that the effect is real (7). (N.B. the numbers in brackets refer to branches in the decision tree).

8.2 On the possibility of a defect in the apparatus

Apparatus defects could consist of:

(a) inefficient counters (8). If the coincidence system were not 100% efficient, the effect would be unimportant, because the undetected events would not contribute to the measured distribution. However, if the anti-coincidence counter were not 100% efficient, this would contribute to the measured distribution, and particles of higher energies than those calculated will be observed. Such particles would contribute heavily to the small angle region and would give rise to a distribution which decreases faster with increasing angle than would have been the case in the ideal experiment when the anticoincidence counter is 100% efficient.

But the graph of the number of counts against the anticoincidence counter voltage (Fig. 6.2.2) suggests that the anticoincidence counter is efficient. In any case this would be unimportant for our experiments involving the cosmic ray absorption technique, i.e. with the experiment performed with the lead absorber in position and then for the same period of time with the lead absorber removed, and then subtracting the two experimental distributions. This will cancel the effect of any inefficiency of the anticoincidence counter on the corrected experimental distribution.

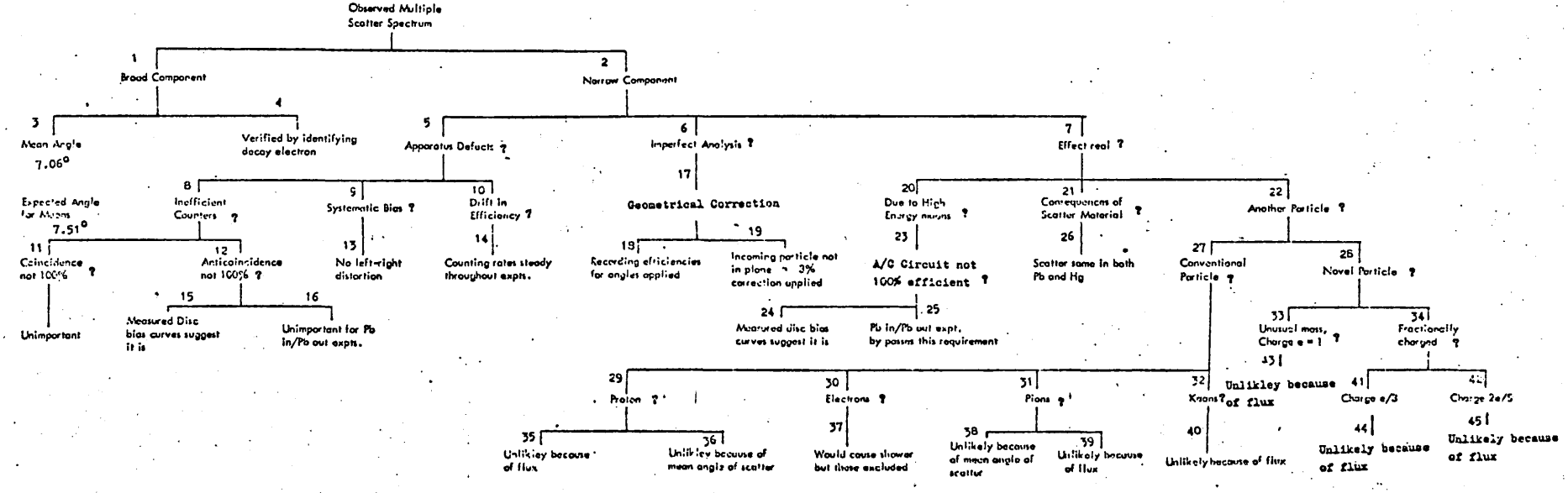

Fig.8.1.4 The decision tree

One might comment that if this distribution were due to some high energy contamination, i.e failure of the anticoincidence counter, then the experimental distribution would have the shape of an exponential distribution rather than a Gaussian distribution. The experimental events were grouped in smaller angular intervals of 0.2°, and were displayed in a histogram (Fig. 8.2.1). It can be see that it has approximately a Gaussian form with a flat top.

(b) Systematic bias (9). If there were any systematic angular bias it would be observed in the distribution of all the accepted particles and in that of the scattered particles. Figure 8.2.2 shows that there is no left-right distortion for the accepted or scattered events.

(c) Drift in efficiency (10); one of the apparatus defects which might affect the experimental results is the drift in the efficiency of the detection system. However the counting rate was monitored daily throughout the experiment and it was found to be steady.

8.3 On the possibility of imperfect analysis

The second explanation of this narrow component is that it could be due to some imperfect analysis (6). Two geometrical corrections were applied to the experimental results, one to account for the recording efficiencies for particles scattered at different angles, and the other to account for the cases when the incoming particles are not in the same plane as the photography plane. These corrections were discussed in section 6.3.

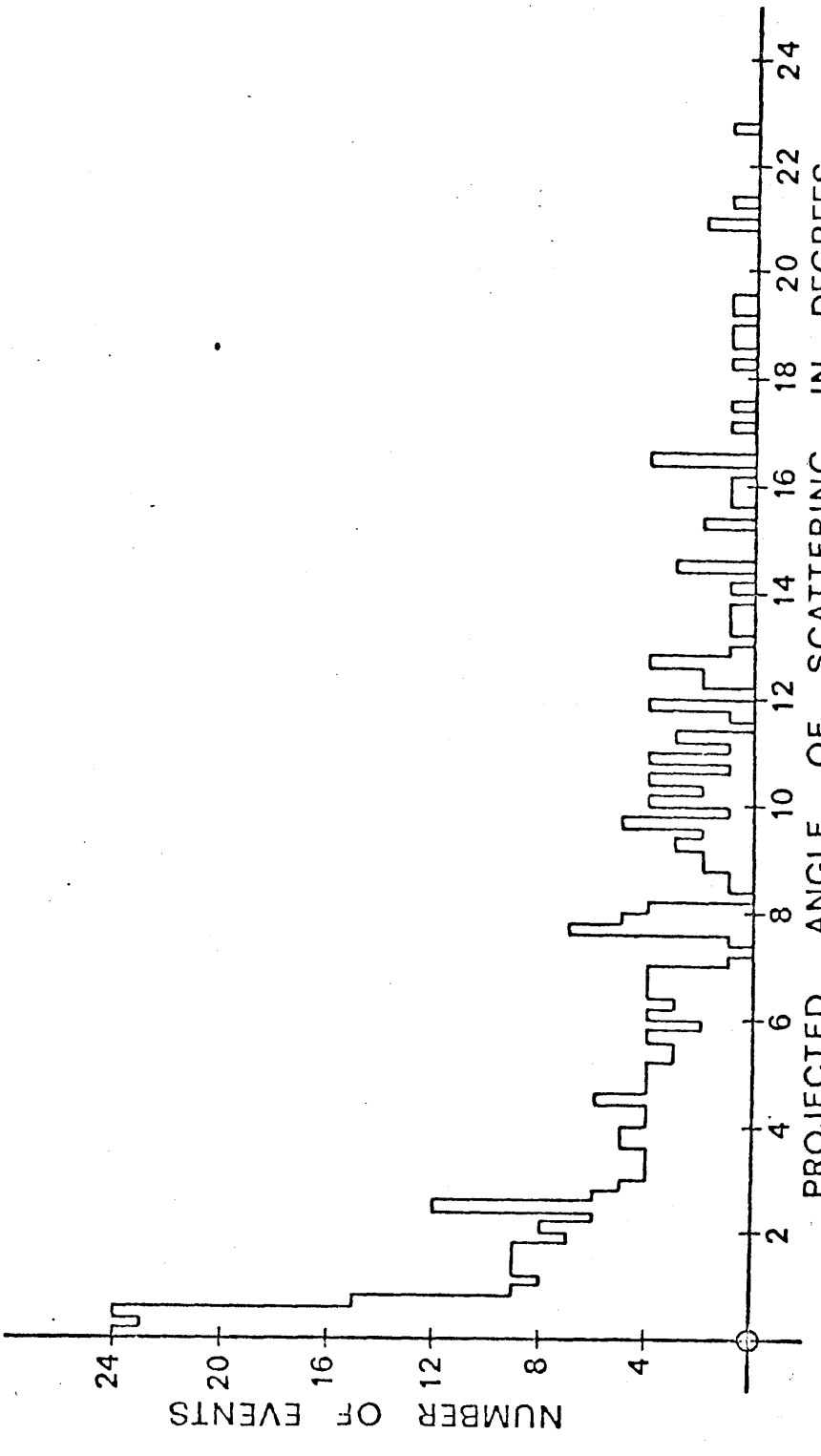

Fig. 8.2.1 The observed distribution represented in a histogram form of angular interval of 0.2 degrees

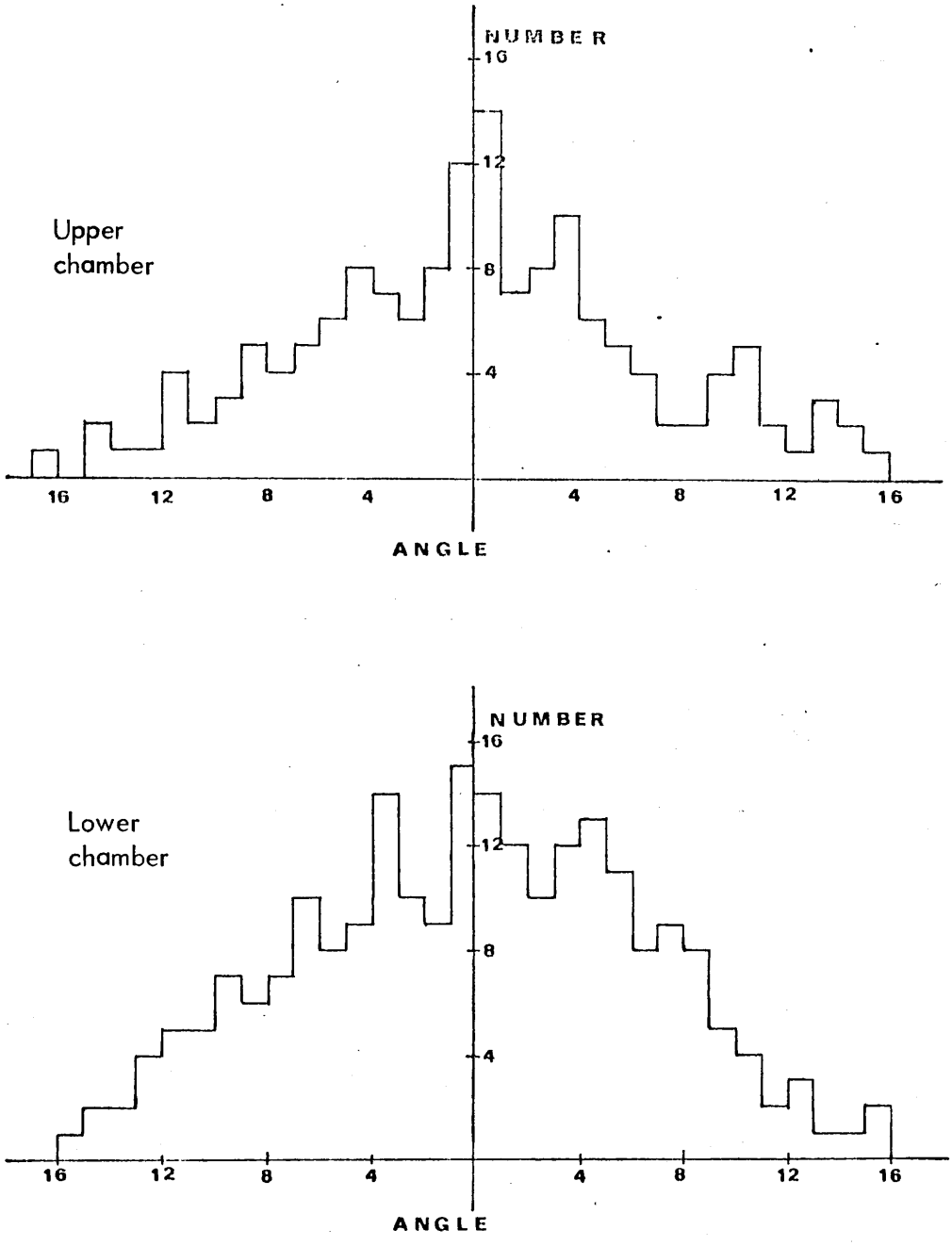

Fig. 8.2.2 Test for possible left/right bias in the performance of the system

Imperfect analysis was omitted as the explanation for the narrow component of the experimental distribution, because the same method of analysis was applied to the results obtained for the experiment in which muons were identified by their decay electron (chapter 7) and it was found that the experimental distribution was in very good agreement with the predicted distribution (see chapter 9).

8.4 On the possibility of the narrow component being significant

The only other interpretation of the experimental distribution, i.e. the narrow component, is that the effect is real. Three causes might explain this narrow component if the effect is real.

(1) It is due to high energy muons included in the experimental data due to inefficiency of the anticoincidence counter, but this is most unlikely because of (a) in 8.2.

(2) The second suggestion to explain the experimental results is that they are a consequence of the nature or crystalline structure of the scattering material, e.g. due to channelling although channelling has only been observed at low energies (a few MeV).

This suggestion was ignored because the same results i.e. the narrow component was observed in the two cases, when the scatterer used was lead and mercury, and that the results of the identified muons was in good agreement with the theoretical prediction in both cases.

(3) The other explanation is that the narrow component in the experimental distribution is due to some other particles included in the results. It could be either a conventional particle or novel particle. The possibility that a conventional particle is the explanation for the experimental distribution is investigated in what follows, taking into account that the hard component of cosmic rays at sea level consists mainly of muons, protons and electrons. Electrons could be excluded because they would cause showers in travelling through 17 cm of lead, which could be noticed and excluded from the analysis. The other particles considered were pions which were unlikely because, for pions to satisfy the experimental conditions, they must have an energy of 148 MeV and this would give a mean scattering angle of 6.5^{o} which is about 4 times larger than the observed mean scattering angle (1.6^{o}). And the pion flux at sea level is very small (about 1% of the proton flux), i.e. much smaller than the expected flux calculated from the experimental distribution.

Assuming that the narrow distribution is a scatter distribution of protons, then these protons must have a mean energy of 291 MeV. to satisfy the experimental conditions i.e. to go through 7.5 cm of lead and to stop in the 1.5 cm of lead absorber placed between the anticoincidence counter and one of the coincidence counters. The mean scattering angle of protons of such energy was calculated to be 2.74^{o} (equivalent to a rms value of 3.69^{o}) while the observed mean scattering angle obtained from the narrow component of the experimental results was 1.6^{o} (rms 2.04^{o}).

From the number, and the time in which these events were obtained, the flux of the particles responsible for this narrow distribution was calculated. The number of events observed was 148 obtained in 140 hours.

The flux of particles was calculated from the observed event rate by using the Greisen (1942) relation:

$$\frac{N}{I} = \frac{b^2}{4}\left[3\frac{a}{l}\tan^{-1}\left(\frac{a}{l}\right) + \frac{a^2}{l^2 + a^2}\right] \qquad 8.2$$

where l is the separation of the counter, a and b are the length and the width of the coincidence counters, N is the event rate and I is the absolute flux. For the present experiment the ratio

$$\frac{N}{I} = 44.6$$

Therefore, in our case with N = 0.000294 per second the absolute flux for the particles in the narrow component was found to be

$$1 = 6.58 \times 10^{-6} \text{ part/cm}^2\text{/sec/sr.}$$

Although the momentum of the protons at the scatterer was in the range 794 $\pm$ 16 MeV/c, because of the 15 cm of lead above the streamer chamber, the actual sea level momentum of any protons triggering the chamber would be 1161 $\pm$ 18 MeV/c. From the established momentum spectrum of protons at sea level (see Hayakawa, 1970), the calculated flux of these protons is 6×10^{-5} part/cm^2/sec/sr/(GeV/c), and hence the flux of protons triggering the chamber is expected to be:

$$2.1 \times 10^{-6} \text{ part/cm}^2\text{/sec/sr}$$

which is smaller than the experimental flux. For these reasons it was considered that protons were an unlikely explanation for the narrow component.

Faced with the dilemma of there apparently being no conventional particles that could account for the narrow distribution, we have considered whether cosmic rays might include some so-far undetermined particles. One obvious possibility is the particle with the electron charge but unknown mass. Using the 2.04 width of the distribution, a plausible mass was calculated as follows: From Cooper and Rainwater theory:

$$(GQ)^{\frac{1}{2}} = (\varphi)$$

where φ is the root mean square calculated from the experimental results. Since G is almost independent of β, for G = 7.32,

$$\left(\frac{E_s}{vp}\right)^2 = \text{const} = K.$$

where E_s is the characteristic energy of scattering and is given by:

$$E_s = 21 \; Z_i^2 \text{ MeV}$$

where Z_i is the charge of the scattered particle.

Then the mass of the scattered particle is:

$$\frac{M_o\beta^2}{\sqrt{1-\beta^2}} = 21\ Z_i^2/\sqrt{k} \quad \text{MeV}/c^2 \qquad 8.4.1$$

From equation 8.4.1 a value for Mo was assumed and a value for β was obtained. From Sternheimer (1959) we have the relation

$$R_o = \frac{1}{Z_i^2} \frac{M_o}{Mp} Rp \left(\frac{Mp}{M_o} T_o \right) \qquad 8.4.2$$

where R_o, T_o, Z_i and M_o are the range, energy, charge and mass of the particle, M_p is the proton mass and R_p is the proton range for the appropriate energy $\frac{M_p}{M_o} T_o$

The range of the particle R_o is set by the experimental arrangement to be between 7.5 and 9 cm. By substituting various values of M_o in equation 8.4.1 one obtains corresponding values of β; one then calculates T_o and from the relation 8.4.2 one calculates R_o. M_o can be varied until the correct range is obtained. In addition to $Z_i = 1$ the calculation was also performed for Z_i = e/3 and 2e/3. The calculated masses for the different charges are given in table 8.4.1.

Table 8.4.1

charge	Mass MeV/c^2	β	$\frac{-dE}{dx}$ MeV $(gm/cm^2)^{-1}$	Range in cm of lead
1	3800	0.47	+5.21	8.42
$2e/_3$	1600	0.47	+2.32	8.18
$e/_3$	400	0.47	+0.58	8.50

Table 8.4.1 indicates combinations of mass and charge that are compatible with the width of the narrow component in the multiple scattering distribution. The possibility of the peak being due to heavy particles of mass 3800 MeV/e^2, or due toquarks is discussed later.

Values of ionisation loss would give a clue to the nature of any novel particles. The streamer chamber is not normally a sensitive indicator of ionisation loss, but nevertheless it is sensible to estimate the losses for these particles.

The energy loss by ionization is given by the Bethe-Bloch relation:

$$\frac{-dE}{dx} = \frac{2Cm_e c^2 Zi^2}{\beta^2} \left[\ln\left(\frac{4m_e^2 c^4 \beta^4}{(1-\beta^2) I^2(z)} \right) - 2\beta^2 \right]$$

where me is the electron mass, Zi the charge of the ionizing particle, C is a constant given by:

$$C = \pi N z A^{-1} r_e^2$$

$$= 0.15 \frac{Z}{A} \quad (gm^{-1}cm^2)$$

and I (Z) is a matter constant depending on the ionization potential of the traversed matter (i.e. is the average ionization potential):

$$I(z) = 9.1 (1 + 1.9 Z^{-2/3}) Z. \qquad (eV)$$

The energy loss by ionization was calculated for neon for the different particles and the values are included in table 8.4.1.

The calculated values of $\frac{-dE}{dx}$ for muons and protons accepted by the experimental arrangement are 1.82 MeV$(gm/cm^2)^{-1}$ and 3.03 MeV$(gm/cm^2)^{-1}$.

From the previous discussion it was concluded that a possible explanation for the experimental results might be:

(a) Due to a novel particle, either fractionally charged or of charge e = 1 but of unusual mass. The flux of such particle was calculated to be 6.58×10^{-6} part/cm^2/sec/sr which is much higher than the upper limit for quark fluxes established by cosmic ray ionisation experiments (Jones, 1973).

McCusker et al. (1969) claimed to have found five quarks based on the finding of five cloud chamber tracks so thin that they seemed to correspond to particles with only a fraction of the electron charge.

A quark of 2e/3 charge would be expected to make a track having a specific ionization of only 4/9 that of ordinary high energy particles; just the reduction in ionization McCusker observed. The main argument against McCusker's interpretation is that experiments similar to his have so far failed to provide evidence of quarks. Adair and Kasha (1969) placed limits on the flux of the quark in the secondary cosmic rays of about

$$10^{-10} \quad \text{par/cm}^2\text{/sec/sr.}$$

They concluded that the claim of McCusker et al. was in contradiction with the results of their search.

(b) The experimental distribution could be explained if the percentage of protons stopped by the lead absorber is about 10 times the calculated one, i.e. the proton flux at sea level has to be much higher than the well established proton flux at sea level. Although the ratio of protons to muons at sea level for the energy concerned has been given by Allkofer (1970) as about 4%, we have also calculated the ratio for the particles accepted by the present experimental system by using the established fluxes. The minimum range in lead was 22.5 cm, and the maximum range 24 cm, and using the Rossi graph, the mean energy for accepted muons was estimated to be 328.6 MeV, and the energy interval was 21.2 MeV (Δ E). The mean muon monentum was P (mean) = 421.5 MeV/c and Δ P = 21.8 MeV/c.

And for protons the corresponding values were P mean = 1161 MeV/c and ΔP = 36 MeV/c.

From the graphs of the flux intensities of muons and protons given in Hayakawa's book (1970), the flux intensity of muons observed in the experiment was:

$$I_{\mu} = 3 \times 10^{-3} \quad \text{part cm}^{-2} \text{ sec}^{-1} \text{ sr}^{-1} \text{ (GeV/c)}^{-1}$$

and for protons

$$I_{p} = 6 \times 10^{-5} \quad \text{part cm}^{-2} \text{ sec}^{-1} \text{ sr}^{-1} \text{ (GeV/c)}^{-1}$$

Hence the proportion of protons in the present experiment is estimated to be 3.2%. In this calculation the roof and ceiling above were ignored. Including them, a rough estimate suggested a proton contamination of 2.1%. Using these ratios the total number of protons expected to be observed in the experiment was 23 particles when the ceiling was included, and 40 particles when the ceiling was ignored. So the total number of protons expected should not exceed 40 particles. The number of events in the narrow component was 148 particles, scattered between 0^{o} and 5^{o}. The number of protons that will scatter in the region 0^{o} to 5^{o} was calculated to be less than 33 which is about 5 times smaller than the observed number.

An attempt was made to find the proton to muon ratio that will satisfy the experimental distribution (Fig. 8.1.1). By using equation 8.1.1 and changing the proportion of protons present (x), it was found that in order to satisfy the experimental results the proton contamination at sea level under the experimental conditions would have to be 25% which is about 10 times the calculated value.

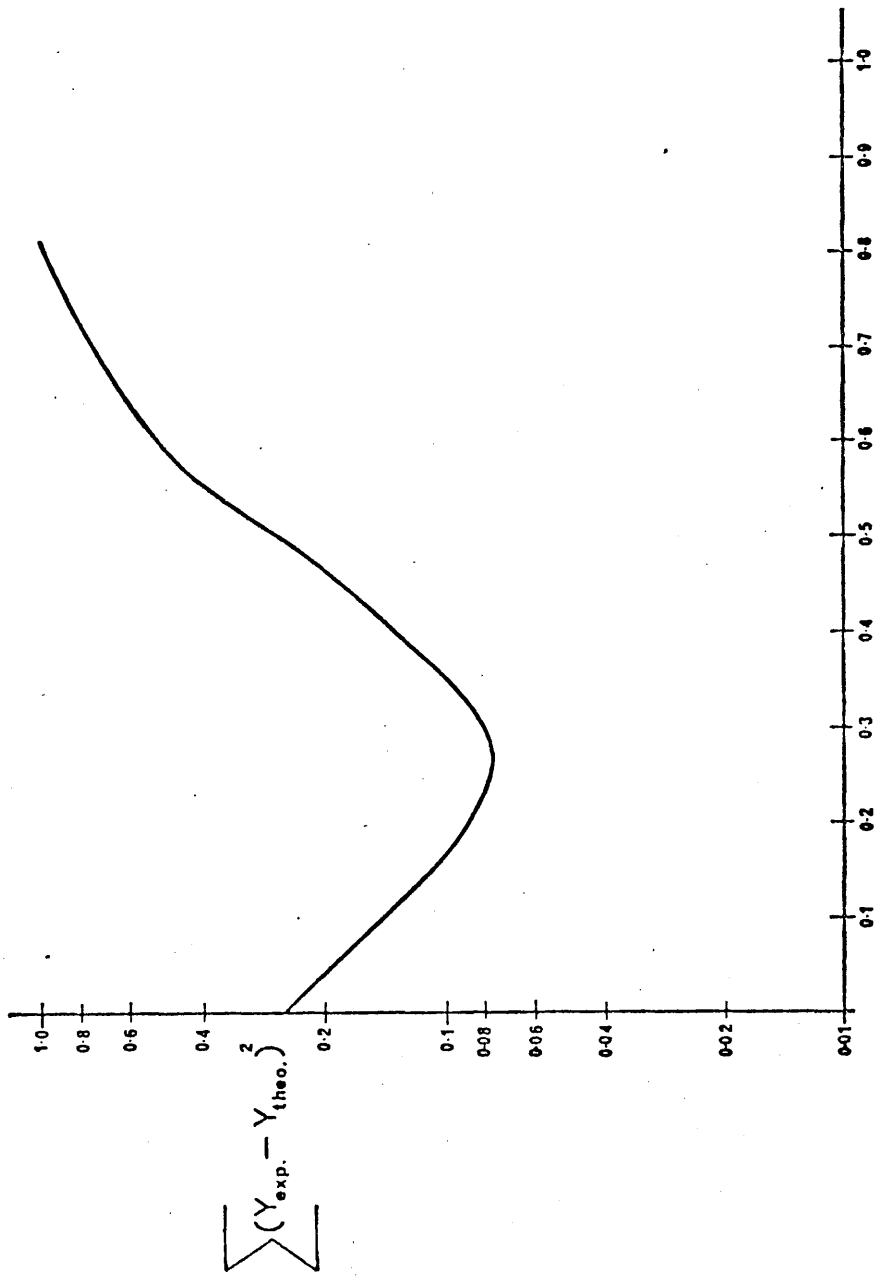

Fig. 8.4.1 Statistical test of the success of fitting

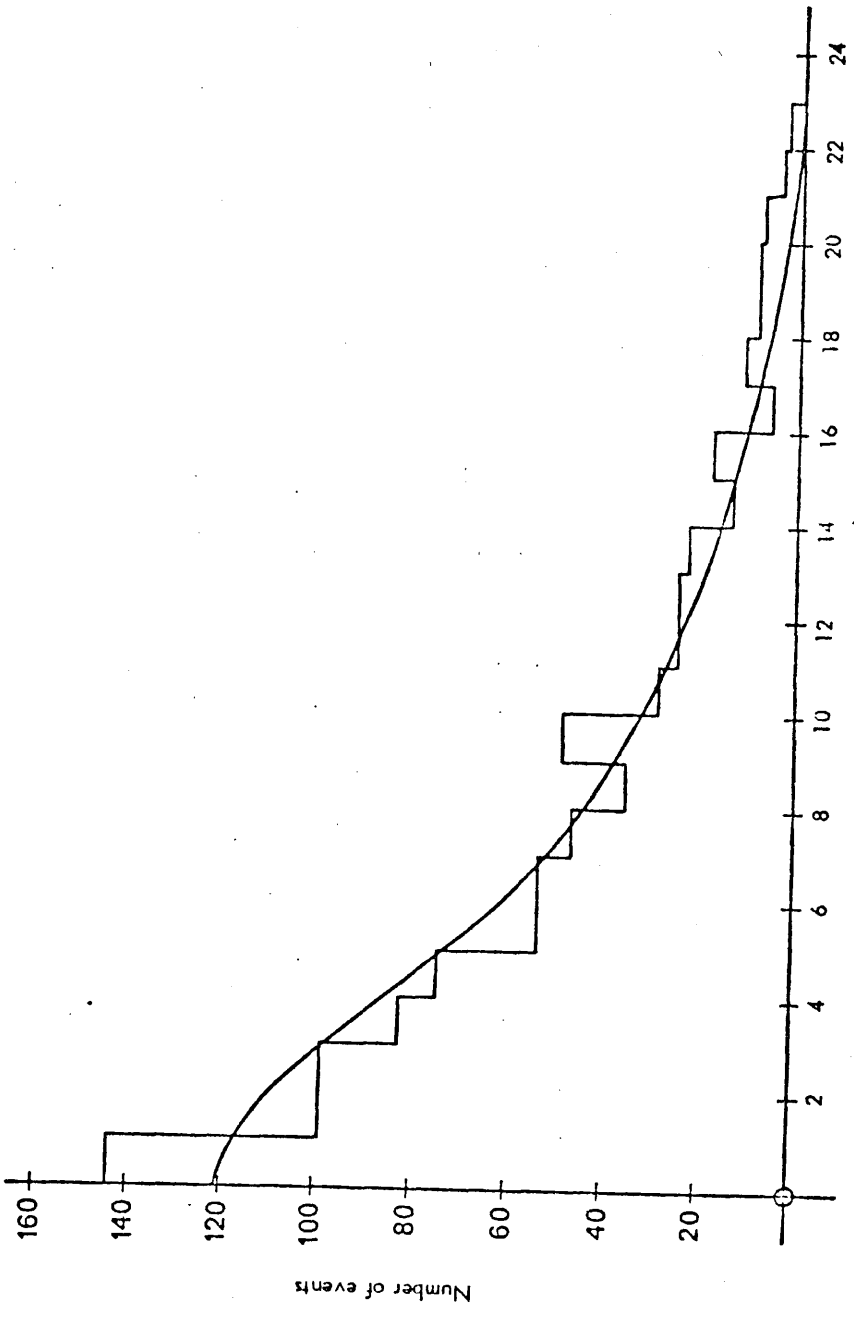

Fig. 8.4.2 The observed distribution represented in a histogram form. The curve represents the theoretical model for muon with a 25% proton contamination

Figure 8.4.1 shows the value of the agreement with the experimental results plotted against x. This graph was obtained using a computer to help solve equation 8.1.1 and finding the sum of the difference between the experimental points and the calculated ones from equation 8.1.1. Figure 8.4.2 shows the calculated distribution with the proton contamination 25% fitted to the experimental results.

In conclusion, we note that the results are compatible with existance of heavy particles, or fractionally charged particles, or very high proton fluxes at sea level. All these explanations appear to contradict established beliefs, and further study would appear advisable.

CHAPTER 9

Conclusion on the multiple scattering of the identified cosmic ray muons

The multiple scattering distributions of cosmic ray muons identified by an electron resulting from decay in the carbon absorber has been measured for two scatterers, mercury and lead, of 2.5 cm thickness. This has been described in chapter 7. In the analysis of these results the Cooper and Rainwater, and the Moliere models were used to calculate the expected distribution. A statistical test was carried out on both theories to find out which theoretical prediction is in better agreement with the experimental results.

The expected distribution obtained on the basis of the Cooper and Rainwater expression (2.1.46) was evaluated in the way described in 6.5, the appropriate values of G and Q were calculated from (2.1.36) and (2.1.28). In the Cooper and Rainwater expression (2.1.46) the effect of single scattering was given by:

$$\frac{1}{\sqrt{\pi}} \qquad \frac{1}{4G} \qquad \int_{t}^{\infty} \lambda^{-3} \quad F_N\,(\lambda/\chi o)\; T\,(\lambda,\, xo)\; d\lambda$$

The effect of this term was found to be negligible for the angular range observed in this work. For a particle scattering through a 20^{o} angle the correction term due to the effect of single scattering was found to be about 0.0003 which is about 1% of the other two terms in the Cooper and Rainwater expression. The nuclear form factor F_N was taken to be $1/Z$.

The evaluation of Moliere theory of multiple scattering was performed as follows since the distribution function is given as an expression in a power series in B^{-1}.

$$f(\theta)\,\theta\,d\theta = y\,dy\,[f^{o}(y) + B^{-1} f'(y) \ldots\ldots] \qquad 9.2.3$$

where B is defined as

$$B - \ln B = b \qquad 9.2.4$$

and

$$e^{b} = \frac{6680}{\beta^{2}}\, t \quad \frac{(Z+1)\, Z^{\frac{1}{3}}\, z}{A\,(1+3.3\alpha^{2})} \qquad 9.2.5$$

where α is the usual parameter $\alpha = zZe^{2}/h\beta c$

and $$y = \theta/(Q\,B^{\frac{1}{2}}) \qquad 9.2.6$$

$$Q^{2} = 4\pi\, te^{4}\, Z(Z=1)\, z^{2} / (Pv)^{2} \qquad 9.2.7$$

the first two functions in 9.2.3.

$$f^{(o)} = 2\,e^{-\chi}$$

$$f' = 2\,e^{-\chi}(\chi-1)\,[\bar{E}_{i}(\chi) - \ln(\chi)] - 2(1-2e^{-\chi})$$

where $\chi = y^{2}$ and $\bar{E}_{i}(\chi)$ is defined in Jahnke E. E mde F. (1943).

For small angles, i.e., y less than about 2, the Gaussian $f^{(o)}$, is the dominant term, in this region $f^{(1)}$ is in general less than $f^{(o)}$, so that the correction to the Gaussian is of order 1/B i .e . of the order of 10%. For larger angles y> 2 the function $f^{(1)}$ becomes larger than $f^{(o)}$. So $f^{(o)} + B^{-1} f^{(1)}$ is a good approximate representation of the distribution at any angle (Bethe, H.A. 1953).

The two expected distributions, the one calculated on the basis of the Cooper and Rainwater expression and the other calculated on the basis of the Moliere distribution were normalized to the same area under the experimental histogram. Figs. 9.1 and 9.2 show these distributions fitted to the experimental results of 7.2 and 7.3 where the scatterer was mercury and lead respectively.

A chi squared test on both results shows that for Mercury

P_{X^2}	Cooper and Rainwater	=	70%
P_{X^2}	Moliere	=	50%

and for lead

P_{X}	Cooper and Rainwater	=	75%
P_{X^2}	Moliere	=	30%

The probability P_{X^2} that a repetition of the observations would show a greater deviation from the predicted distribution was calculated as explained in Appendix C.

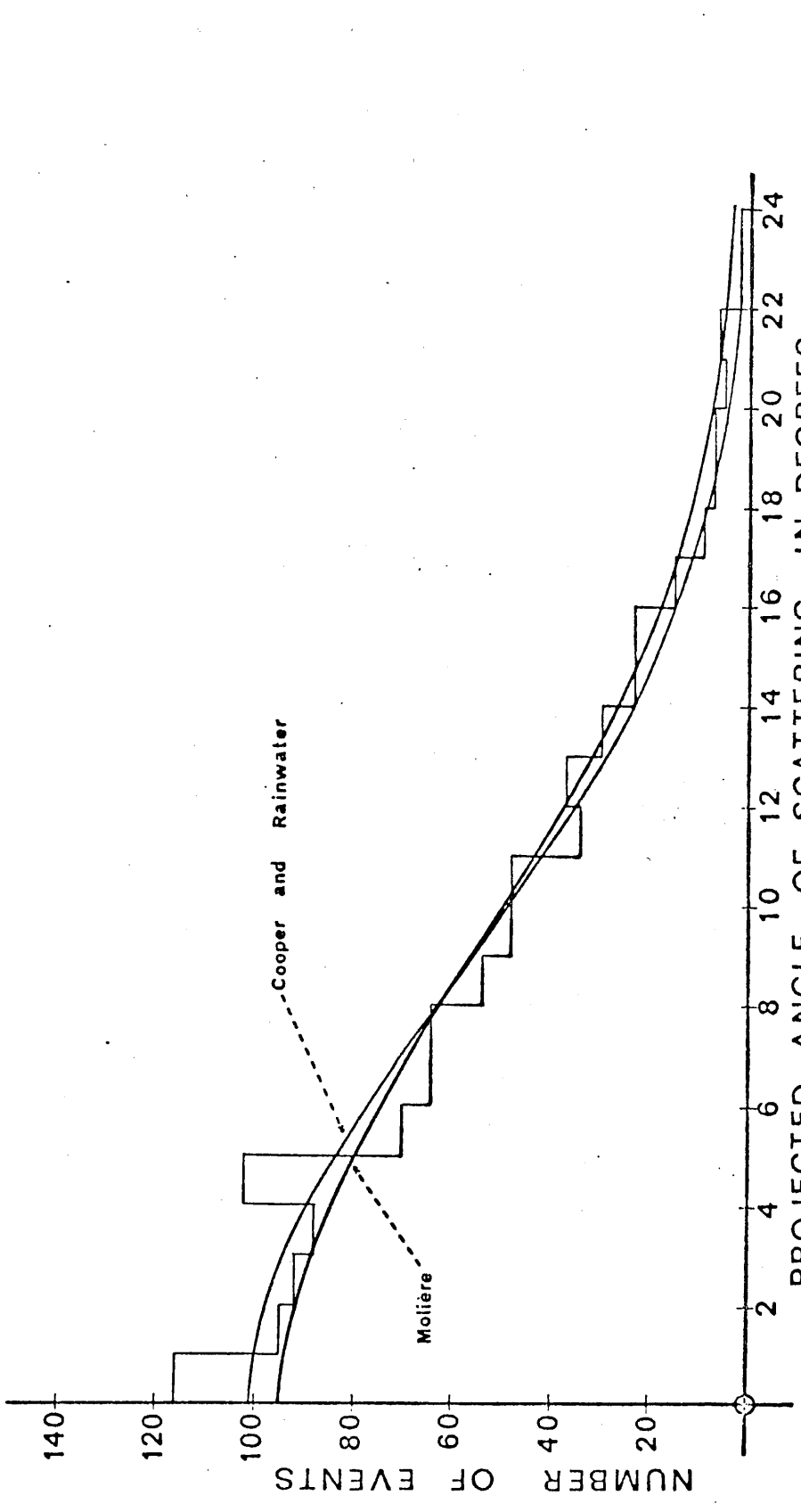

Fig. 9.1 The observed distribution of the multiple scattering angle in mercury displayed in a histogram form. The curves represent the two theoretical models normalised to the same area.

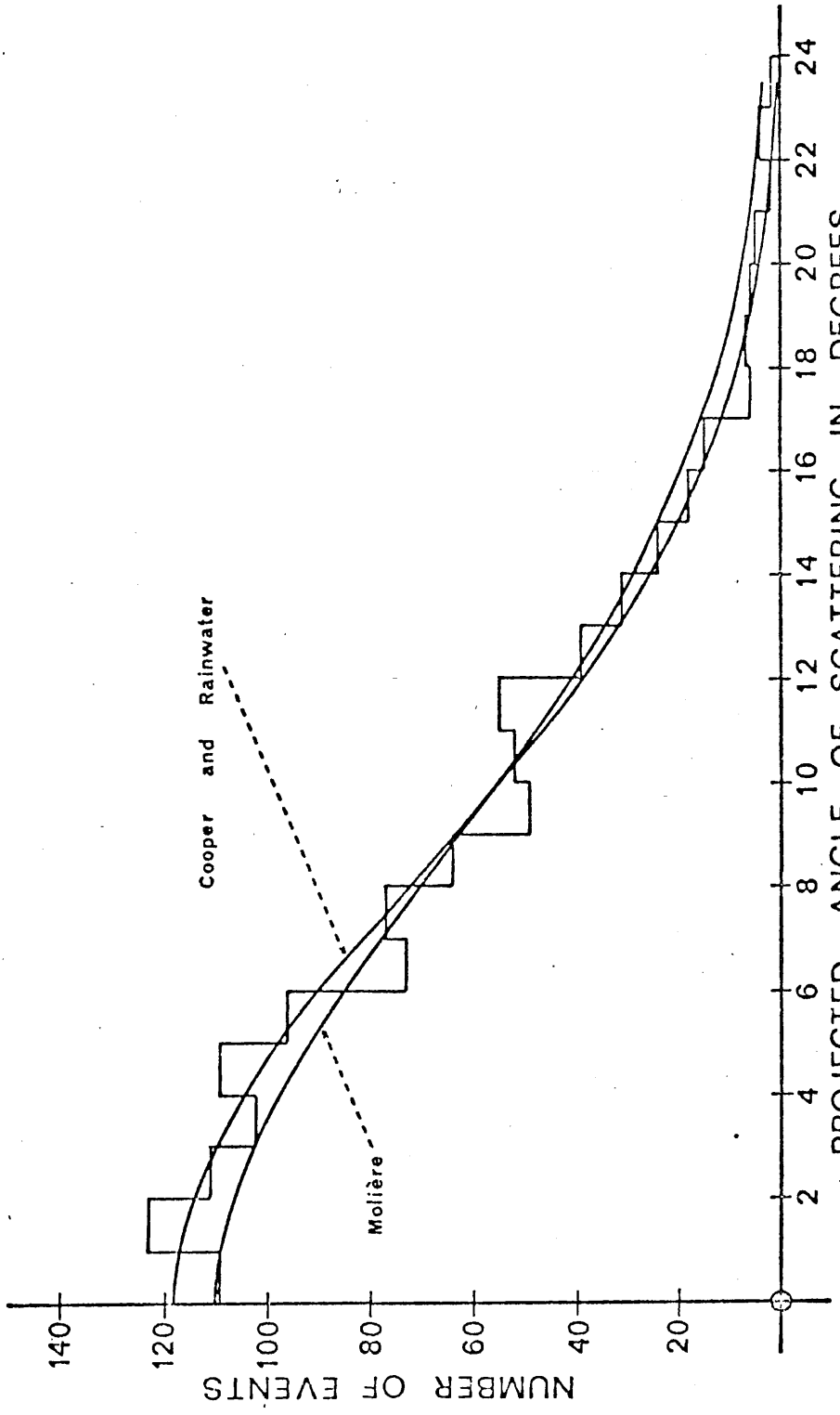

Fig. 9.2 The observed distribution of multiple scattering angles in lead depicted as an histogram. The curve represent the theoretical model normalised to the same area

The X^2 test results showed that the experimental results are in better agreement with Cooper and Rainwater theory than with Moliere theory. It was concluded that the measurements favour Cooper and Rainwater theory, in the momentum region 230 MeV/c, this is in agreement with the finding of Meyer et al., (1962) and Bizard et al., (1966). Other low momentum measurements (Chidley et al., 1959) and Kirillov-Vgrgumov et al., (1958) were in agreement with Moliere theory. (No comparison with the Cooper and Rainwater was made). The value of $P_{X}2$ obtained by Kirillov-Vgrgumov was 40% for the Moliere theory. From values of $P_{X}2$ obtained for the experimental results of chapter 7, one can see that the difference in both theories is small.

From this work it was concluded the multiple scattering model based on the extended nucleus is the best.

Appendix A: Program to calculate the scattering angle from the track co-ordinates

```
                PROGRAM SCATER (INPUT,OUTPUT,TAPE4=IHY130,TAPE1=IHY130,PUNCH)
000002          DIMENSION IX(10),IY(10),X(10),Y(10)
000002          INTEGER IH(22)
000002          DO 6 I=1,22
000007    6     IH(I)=0
000011          READ (1,100) II,IJ
000020    5     IS=0
000021    1     SUMX=SUMY=SUMXX=SUMXY=0.0
000025          DO 2 I=1,10
000027          READ (1,100) IX(I),IY(I)
000036          IF (EOF(1)) GO TO 99
000043          X(I)=IX(I)
000044          Y(I)=IY(I)
000045          SUMX=SUMX+X(I)
000047          SUMY=SUMY+Y(I)
000051          SUMXX=SUMXX+X(I)*X(I)
000053          SUMXY=SUMXY+Y(I)*Y(I)
000055    2     CONTINUE
000057          IF (IS.EQ.0) 3,4
000062    3     A=(10*SUMXY-SUMX*SUMY)/(10*SUMXX-SUMX*SUMX)
000071          IS=IS+1
000073          PRINT 101,IX
000101          PRINT 101,IY
000107          PUNCH 101,IX
000115          PUNCH 101,IY
000123          GO TO 1
000124    4     B=(10*SUMXY-SUMX*SUMY)/(10*SUMXX-SUMX*SUMX)
000133          ETA=ATAN((A-B)/(1+A*B))
000142          ANGLE=ETA*180./3.1415927
000144          PRINT 101,IX
000152          PRINT 101,IY
000160          PUNCH 101,IX
000166          PUNCH 101,IY
000174          PRINT 102,ANGLE
000202          K=INT(ABS(ANGLE))+1
000206          IF(K.GT.21) PRINT 103,ANGLE
000216    103   FORMAT(/' ERROR IN HISTOGRAM PLOTTING, ANGLE OF'F10.2' TOO LARGE'
                )/)
000216          IF(K.GT.21) GOTO 8
000222          IH(K)=IH(K)+1
000223    8     CONTINUE
000223          GO TO 5
000224    100   FORMAT (I4,2X,I4,2X)
000224    101   FORMAT (10I8)
000224    102   FORMAT (5X,'ANGLE IS'F10.4,//)
000224    99    CONTINUE
000224          DO 9 I=1,21
000226          IF(IH(I).GT.75) PRINT 104,I,IH(I)
000240          PRINT 105,I,IH(I)
000250    104   FORMAT(/' TOO MANY SCORES FOR HISTOGRAM, ANGLE ='I4' SCORES='I6/)
000250    105   FORMAT (2I5)
000250          IF(IH(I).GT.75) IH(I)=75
000255    9     CONTINUE
000257          STOP
000261          END

UNUSED COMPILER SPACE
005300
```

Appendix B: Program to calculate the scattering probability from the Cooper and Rainwater model

```
FUNCTION COSH        74/74   OPT=1                          FTN 4.0+P357

      FUNCTION COSH(A)
      COSH=(EXP(A)+EXP(-A))/2.
      RETURN
      END
```

```
FUNCTION SINH        74/74   OPT=1                          FTN 4.0+P357

      FUNCTION SINH (A)
      SINH=(EXP(A)-EXP(-A))/2.
      RETURN
      END
```

```
 PROGRAM SCATT       74/74   OPT=1                          FTN 4.0+P357

      PROGRAM SCATT (INPUT,OUTPUT)
      ANGLE=0
    5 RAD=ANGLE*3.1415927/180.
      G=7.424
  5   B=3.4609E-3
      ETA=1./SQRT(2.*G*G)*RAD
      X=EXP(-ETA*ETA)
      Y=1.*X/SQRT(3.1415927)
      Z=2.*1.25*ETA
 10   W=2.*(2.*ETA*ETA-1.)*(ALOG(0.25/1.26)+Z**2./4.+Z**4./(4.*24.)
     1+Z**6./(6.*720.))
      U=6.*ETA*ETA-1/(0.25*3.25)*(COSH(2.*0.25*ETA)-1)-2.*ETA/0.25
     1*SINH(2.*3.25*ETA)
      S=U+W
 15   SCAT=Y*(1.+B/(4.*G))
      PRINT 100,ETA,B,SCAT
      ANGLE=ANGLE+0.5
      IF (ANGLE.LE.25.) GO TO 5
  100 FORMAT(1X,'ETA',F8.4,'B',E14.5,'SCATTERING PROBABILITY IS',E14.5)
 21   STOP
      END
```

Appendix C: Chi square evaluation

The chi square test may be stated as follows:

$$\chi^2 = \sum^{i} \frac{[(\text{observed value}) i - (\text{expected value}) i]^2}{(\text{expected value}) i}$$

where the summation is over the total number of independent classifications (i) in which the data have been grouped (angle intervals in the present case). Secondly one determines the number of degrees of freedom F, which is the number of independent classifications in which the observed data may differ from the predicted one. From χ^2 and F the value of P could be obtained from the tables given by (Bevington, P.R., 1969). In interpreting the value of P, we may say that if P lies between 0.1 and 0.9, the assumed distribution very probably corresponds to the observed one, while if P is less than 0.02 or more than 0.98 the assumed distribution is extremely unlikely.

The experimental results have been grouped in 24 angular intervals; hence there are originally 24 ways in which observations may be different from the calculation. However, there are not 24 degrees of freedom because two restrictions are placed, i.e. we have used two degrees of freedom by specifying the total number of intervals and the total number of events.

Appendix D: Rossi's Range-Energy relation graph

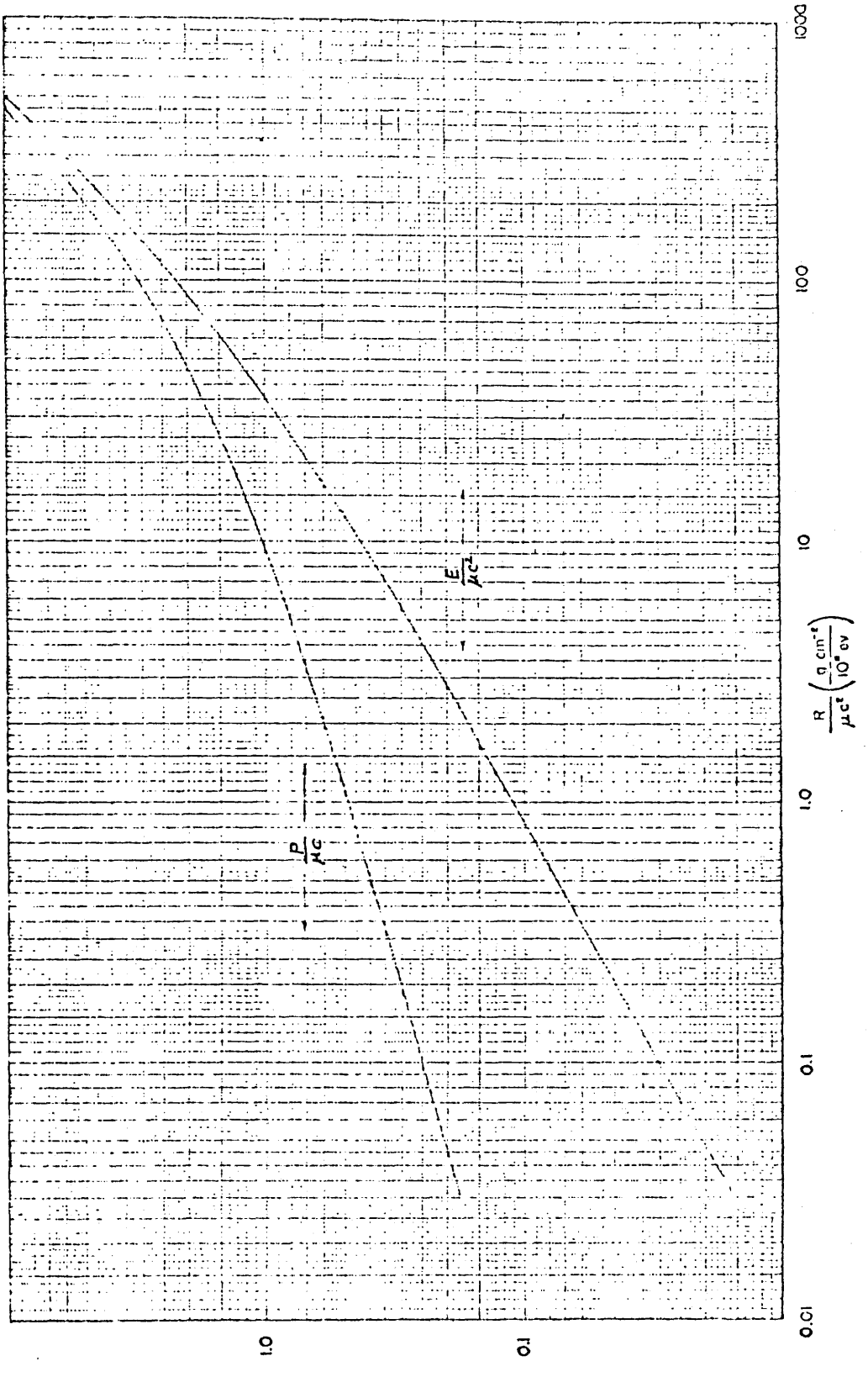

ACKNOWLEDGEMENTS

I wish to express my sincere appreciation to my supervisor Dr. Peter Rice-Evans for the guidance and help extended by him during the course of this research.

I wish to thank Professor H.O.W. Richardson and Professor E.R. Dobbs for their support, Dr. P. Pal for his help in computation and Mr. R.N. Thomas for his interest and I wish to thank Dr. Peter Trent of Birkbeck College for the use of a digitising table.

I would also like to thank Messrs. W.A.G. Baldock, F.A. Grimes, A.K. Betts, A. Lemottle, J.D. Sales, B. Pashley and A. King for their technical assistance.

I am grateful to the University of Tripoli for providing me with a Scholarship to enable me to proceed with this work.

Adair, R.K., and Kasha, H., Phys. Rev. Lett. 23, 1355 (1969).

Alikhanian, A.I., Shostakovich, N.V., Dadaian, A.T., Fedorov, V.N., and Deriagin, B.N. Soviet Phys. J.E.T.P. 4, 817 (1957).

Alikhanian, A.I., and Arutyunian, F.R., Nucl. Phys. 10, 244 (1959).

Alikhanian, A.I., Asatiani, T.L., Matervosiah, A.M., and Sarkhatunian, R.O., Physics Lett. 4, 295 (1963).

Allkofer, O.C., Bagge, E., Henning, P.G., and Schmieder, L., Atom Kernenergie 2, 88 (1957).

Allkofer, O.C., with Dall, W.D., and Grupen, C., "Spark Chambers" (Verlag Karl Thiemig K.G., Munchen 1969).

Allkofer, O.C., and Knoblich, P., Lett. Nuovo Cim., 3, 6 (1970).

Allen, K.R., and Phillips, K., Proc. Roy. Soc. (London) 278A, 188 (1964).

Annis, M., Bridge, H.S., and Albert, S., Phys. Rev. 89, 1216 (1953).

Bell, W.A., and Hincks, E.P., Phys. Rev. 84, 1243 (1951).

Bella, F., Franzinetti, C., and Lee, D.W., Nuovo Cim. 10, 1338 (1953).

Bethe, H.A., and Ashkin, J., "Experimental Nuclear Physics" Vol. 1. ed. by Segre, E., Wiley, New York (1953).

Bethe, H.A., Phys. Rev. 89, 1256 (1953).

Bevington, P.R., "Data reduction and error analysis for Physical Sciences" (McGraw Hill, 1969).

Bizard, G., Duchon, J., Milliard, J., Patry, J.P., Scherer, M., and Seguinot, J., Nucl. Phys. 56, 385 (1964).

Bizard, G., Duchon, J., Landaud, G., Lemeilleur, F., Patry, J.P., Scherer, M., and Yonnet, J., Nucl. Phys. 87, 495 (1966).

Bulos, F., Odian, A., Villa, F., and Yount, D., SLAC Report 74 (1967).

Chidley, B., Goldstein, P., Hinman, G., Summers, B., and Adler, R., Phys. Rev. 116, 1015 (1959).

Chikovani, G.E., Mikhailov, V.A., and Roinishvili, V.N., Phys. Letters 6, 254 (1963).

Chikovani, G.E., Roinishvili, V.N., and Mikhailov, V.A., Nucl. Inst. Meth. 29, 261 (1964).

Chikovani, G.E., Roinishvili, V.N., Mikhailov, V.A., and Javrishvili, A.K., Nuc. Inst. Meth. 35, 197 (1965).

Code, F.L., Phys. Rev. 59, 229 (1941).

Conversi, M., Poncini, E., and Piccioni, O., Phys. Rev. 71, 204 (1947).

Cooper, L.N., and Rainwater, J., Phys. Rev. 97, 492 (1955).

Cranshaw, T.E., and de Beer, J.F., Nuovo Cim. 5, 1107 (1957).

Crewe, A.V., Proc. Phys. Soc. (London) 64A, 660 (1951).

Crewe, A.V., and Litherland, A.E., Jou. Sci. Inst. 28, 182 (1951).

Dalitz, R.H., Proc. Phys. Soc. A206, 509 (1951).

Davidenko, V.A., Dolgoshein, B.A., and Somov, S.V. Societ Physics J.E.T.P. 28, 227 (1969).

Davidenko, V., Dolgoshein, B., and Somov, S., Nucl. Phys. 75, 277 (1969).

Davidenko, V., Dolgoshein, B., Semenov, S., and Somov, S., Soviet Physics J.E.T.P. 28, 223 (1969).

Dolgoshein, B.A., Rodinov, B.V., and Luchkov, B.I., Nucl. Inst. Meth. 29, 270 (1964).

Evans, D., "The Atomic Nucleus" (McGraw Hill, 1955).

Fowler, G.N., and Wolfendale, A.W. "Progress in Elementary Particle and Cosmic Ray Physics" (North Holland, 1958).

Fredholm, O., and Lovstrand, K.G., J. Phys. E., 5, 1058 (1972).

Fukui, S., and Miyamoto, S., Nuovo Cim., 11, 113 (1959).

George, F.P., Redding, J.L., and Trent, P.T., Proc. Phys. Soc. A66, 553 (1953).

Goudsmith, S.A., and Sanderson, J.L., Phys. Rev. 57, 24 (1940).

Greisen, E., Phys. Rev. 61, 212 (1942).

Grieder, P.F.K., Nucl. Inst. Meth. 55, 295 (1967).

Gygi, E., and Schneider, F., CERN Report CERN 64-46 (1964).

Gygi, E., and Schneider, F., CERN Report CERN 66-14 (1966).

Hayakawa, S., "Cosmic Ray Physics" (Wiley Interscience 1969).

Jones, L.W., Phys. Today 5, 31 (1973).

Keuffel, J.W., Rev. Sci. Inst. 20, 202 (1949).

Kirillov-Ugryumov, V.G., Dolgoshein, B.A., Moskvichov, A.M., and Morozova, L.P., Nucl. Phys. 11, 357 (1959).

Lavoi, L., Parker, S., Rey, C., and Schwartz, D.M. Rev. Sci. Inst. 35, 1567 (1964).

Leontic, B., and Wolfendale, A.W., Phil. Mag 44, 1101 (1953).

Lewis, H.W., Phys. Rev. 78, 526 (1950).

Leighton, R.B., Anderson, C.D., and Seriff, A.J., Phys. Rev. 75, 1432 (1942).

Lewis, I.A.D., and Wells, F.H., "Millimicrosecond Pulse Technique" (Pergamon Press, Oxford, 1954).

Lloyed, J.L., and Wolfendale, A.W., Proc. Phys. Soc. A68, 1045 (1955).

Lozanskii, E.D., and Firsov, O.B., Soviet Phys. J.E.T.P. 29, 367 (1969).

McCusker, C.B.A., and Cairns, I., Phys. Rev. Lett. 23, 658 (1969).

Meek, J.M., and Craggs, J.D., "Electrical Breakdown in Gases" (Oxford University Press, 1953).

Merrill, F.H., and von Hippel, A., Jour. Appl. Phys. 10, 837 (1939).

Meyer, M.A., De Villiers, J.A.M., Wolmarans, N.S., and Koen, J.W., Nucl. Phys. 30, 353 (1962).

Meyer, M.A., De Villiers, J.A.M., Wolmarans, N.S., and Koen, J.W., Nucl. Phys. 32, 71 (1962).

Mishra, S.R., Ph.D. Thesis, University of London (1969).

Moliere, G., Z. f. Naturfarsch 3a, 781 (1948).

Nash, W.F., and Pointon, A.J., Nuovo Cim. 9, 412(1958).

Nasser, E., and Loeb, L.B., Jou. Appl. Phys. 34, 3340 (1963).

Nigam, B.P., Phys. Rev. 131, 238 (1963).

Nigam, B.P., and Mathur, V.S., Phys. Rev. 121, 1577 (1961).

O'Brien, K., J. Phys. A. 8, 1530 (1975).

Olbert, S., Phys. Rev. 87, 319 (1952).

Raether, H., "Electron Avalanches and Breakdown in Gases" (Butterworths, London, 1964).

Rasetti, F., Phys. Rev. 60, 198 (1941).

Rice-Evans, P., Jour. Phys. E. 2, 221 (1969).

Rice-Evans, P., and Mishra, S.R., Nucl. Inst. Meth. 67, 337 (1969).

Rice-Evans, P., and Mishra, S.R., Jour. Phys. E. 4, 638 (1971).

Rice-Evans, P., and Hassairi, I.A., Phys. Lett. 38A, 196 (1972).

Rice-Evans, P., and Hassairi, I.A., Nucl. Inst. Meth. 106, 345 (1973).

Rice-Evans, P., "Spark Streamer, Proportional and Drift Chambers" (The Richelieu Press, London, 1974).

Rice-Evans, P., Hassairi, I.A., and Betts, A.K., Nucl. Inst. Meth. 130, 571 (1975).

Roberts, A., Rev. Sci. Inst. 32, 482 (1961).

Roche, G., Fargeix, J., Girard, G., and Farmos, F., Nucl. Inst. Meth. 86, 61 (1970).

Rossi, B., and Greisen, K., Rev. Mod. Phys. 13, 240 (1941).

Rossi, B., and Nereson, N., Phys. Rev. 62, 417 (1942).

Rossi, B., Rev. Mod. Phys. 20, 537 (1948).

Rudenko, N.S., and Smetanin, V.I., Societ Phys. J.E.T.P. 34, 76 (1972).

Sandstorm, A., "Cosmic Rays" (North Holland, 1965).

Scott, W.T., Phys. Rev. 85, 245 (1952).

Sen Gupta, S.N., and Sinha, M.S., Nuovo Cim. 26, 1279 (1962).

Shutt, R.P., Phys. Rev. 61, 6 (1942).

Sinha, M.S., Phys. Rev. 68, 153 (1945).

Snyder, H.S., and Scott, W.T., Phys. Rev. 76, 220 (1949).

Sternheimer, R.M., Phys. Rev. 115, 137 (1959).

Sternheimer, R.M., Phys. Rev. 117, 485 (1960).

Sternheimer, R.M., Phys. Rev. 118, 1045 (1960).

Wagner, K.H., Z. Physik. 186, 466 (1966).

Weissenberg, A.W., "Muons" (North Holland, 1967).

Whittemore, W.L., and Shutt, R.P., Phys. Rev. 88, 1312 (1952).

Wick, G.C., Nuovo Cim. 1, 302 (1943).

Williams, E.J., Proc. Roy. Soc. A169, 531 (1939).

Williams, E.J., Proc. Roy. Soc. 58, 292 (1940).

Wilson, J.G., Proc. Roy. Soc. A174, 74 (1940).

Wolfendale, A.W., (ed). "Cosmic Rays at Ground Level" (The Institute of Physics, London, 1973).